A New Double Laser Pulse Pumping Scheme For Transient Collisionally Excited Plasma Soft X-Ray Lasers

Cotutelle de Thèse - Ko-betreute Dissertation

pour l'Obtention du Titre "Docteur en Sciences" (Dr.) -

zur Erlangung des Grades
"Doktor der Naturwissenschaften" (Dr. rer. nat.)

à l'École Doctorale Ondes et Matière
de l'Université Paris Sud 11 à Orsay

et - und

am Fachbereich Physik, Mathematik und Informatik
der Johannes Gutenberg-Universität in Mainz

présenté par - vorgelegt von

Daniel Frederik Zimmer

né à Mayence - geb. in Mainz

Date de la Soutenance - Datum der mündlichen Prüfung : 6.7.2010

Abstract

Within this thesis a new double laser pulse pumping scheme for plasma-based, transient collisionally excited soft x-ray lasers (SXRL) was developed, characterized and utilized for applications. SXRL operations from $\sim$ 50 up to $\sim$ 200 electron volt were demonstrated applying this concept. As a central technical tool, a special Mach-Zehnder interferometer in the chirped pulse amplification (CPA) laser front-end was developed for the generation of fully controllable double-pulses to optimally pump SXRLs.

This Mach-Zehnder device is fully controllable and enables the creation of two CPA pulses of different pulse duration and variable energy balance with an adjustable time delay. Besides the SXRL pumping, the double-pulse configuration was applied to determine the B-integral in the CPA laser system by amplifying short pulse replica in the system, followed by an analysis in the time domain. The measurement of B-integral values in the 0.1 to 1.5 radian range, only limited by the reachable laser parameters, proved to be a promising tool to characterize nonlinear effects in the CPA laser systems.

Contributing to the issue of SXRL pumping, the double-pulse was configured to optimally produce the gain medium of the SXRL amplification. The focusing geometry of the two collinear pulses under the same grazing incidence angle on the target, significantly improved the generation of the active plasma medium. On one hand the effect was induced by the intrinsically guaranteed exact overlap of the two pulses on the target, and on the other hand by the grazing incidence pre-pulse plasma generation, which allows for a SXRL operation at higher electron densities, enabling higher gain in longer wavelength SXRLs and higher efficiency at shorter wavelength SXRLs. The observation of gain enhancement was confirmed by plasma hydrodynamic simulations.

The first introduction of double short-pulse single-beam grazing incidence pumping for SXRL pumping below 20 nanometer at the laser facility PHELIX in Darmstadt (Germany), resulted in a reliable operation of a nickel-like palladium SXRL at 14.7 nanometer with a pump energy threshold strongly reduced to less than 500 millijoule. With the adaptation of the concept, namely double-pulse single-beam

grazing incidence pumping (DGRIP) and the transfer of this technology to the laser facility LASERIX in Palaiseau (France), improved efficiency and stability of table-top high-repetition soft x-ray lasers in the wavelength region below 20 nanometer was demonstrated. With a total pump laser energy below 1 joule the target, 2 mircojoule of nickel-like molybdenum soft x-ray laser emission at 18.9 nanometer was obtained at 10 hertz repetition rate, proving the attractiveness for high average power operation. An easy and rapid alignment procedure fulfilled the requirements for a sophisticated installation, and the highly stable output satisfied the need for a reliable strong SXRL source. The qualities of the DGRIP scheme were confirmed in an irradiation operation on user samples with over 50.000 shots corresponding to a deposited energy of $\sim$ 50 millijoule.

The generation of double-pulses with high energies up to $\sim$ 120 joule enabled the transfer to shorter wavelength SXRL operation at the laser facility PHELIX. The application of DGRIP proved to be a simple and efficient method for the generation of soft x-ray lasers below 10 nanometer. Nickel-like samarium soft x-ray lasing at 7.3 nanometer was achieved at a low total pump energy threshold of 36 joule, which confirmed the suitability of the applied pumping scheme. A reliable and stable SXRL operation was demonstrated, due to the single-beam pumping geometry despite the large optical apertures. The soft x-ray lasing of nickel-like samarium was an important milestone for the feasibility of applying the pumping scheme also for higher pumping pulse energies, which are necessary to obtain soft x-ray laser wavelengths in the water window. The reduction of the total pump energy below 40 joule for 7.3 nanometer short wavelength lasing now fulfilled the requirement for the installation at the high-repetition rate operation laser facility LASERIX.

Résumé

Cette thèse présente le développement, la caractérisation et l'utilisation d'un laser à rayons X à plasma pompé en régime transitoire collisionnel dans un nouveau schéma en double impulsion. Dans ces conditions, des photons de ~ 50 à ~ 200 électronvolt ont été produits grâce à l'implantation d'un interféromètre de type Mach Zehnder dans la chaine laser infrarouge de type CPA ("chirped pulse amplification") qui sert à générer le laser X. Ce montage permet de contrôler totalement et donc de faire varier la durée, la balance d'énergie et le délai des deux impulsions nécessaires d'une part à la création d'un plasma d'ions multichargés et d'autre part au chauffage des électrons qui viennent pomper par collision l'inversion de population. Nous avons donc pu expérimentalement optimiser ces deux paramètres pour la génération d'un laser X. Ce montage de doubles impulsions réglables a également permis de mesurer l'intégrale B d'un système laser CPA entre 0,1 et 1,5 radians, ce qui est une technique prometteuse pour caractériser l'amplitude des effets non linéaires sur les chaines de puissance.

L'intérêt de la configuration en double impulsion permise par l'implantation du Mach Zehnder est tout d'abord un montage expérimental très simplifié car il se réduit à un seul système de focalisation au lieu de deux initialement dans la configuration GRIP (grazing incidence pumping) classique. Les fluctuations de l'efficacité du laser X dues à une instabilité du pointé du faisceau sont considérablement diminuées et la superposition des deux lignes focales laser est intrinsèquement parfaite. De plus, les données expérimentales et des simulations hydrodynamiques du plasma indiquent un fonctionnement du laser X à des densités électroniques plus élevées, ce qui augmente le gain obtenu à longueur d'onde fixe et permet également d'atteindre potentiellement des longueurs d'onde plus courtes.

Un fonctionnement du laser X à 14,7 nanomètre dans le schéma DGRIP (double-pulse single-beam grazing incidence pumping) a été démontré sur l'installation laser PHELIX à Darmstadt en Allemagne avec un seuil d'énergie de pompe fortement réduit à moins de 500 millijoule. Le même schéma a été implanté sur la chaine LASERIX de l'Université Paris Sud et a permis la démonstration d'un fonctionnement extrêmement stable du laser X à 18,9 nanomètre dans le Molybdène à un taux de répétition de 10 hertz avec une énergie de pompe de moins d'un joule et avec une

énergie de sortie de l'ordre de 2 microjoules. Ce type de fonctionnement est idéal pour l'utilisation d'une telle source pour des applications, comme l'a prouvé une expérience d'irradiation d'échantillons d'utilisateur sur plus de 50000 tirs pendant quelques heures avec une énergie totale déposée de l'ordre de 50 millijoules.

Ce même type de pompage de laser X a été transposé sur l'installation PHELIX avec un angle d'irradiation plus proche de la normale et l'introduction d'une onde progressive pour générer des longueurs d'onde laser X plus courtes qui se rapprochent de la fenêtre de l'eau entre 2 et 4 nanomètre. Un fonctionnement fiable et stable a été obtenu pour le samarium nickelloïde à 7,3 nanomètre avec une énergie de pompe divisée par deux par rapport à des travaux plus anciens. Cela permet d'envisager la démonstration de lasers X courtes longueurs d'onde à taux de répétition élevé sur la station LASERIX.

Zusammenfassung

In dieser Arbeit wurde ein neues Laser Doppelpuls Pumpschema für plasmabasierte, transient Elektronenstoß-angeregte weiche Röntgenlaser entwickelt, charakterisiert und für Anwendungen eingesetzt. Mit diesem Konzept wurde ein effizienter Röntgenlaserbetrieb im Bereich von $\sim$ 50 bis $\sim$ 200 Elektronenvolt demonstriert. Mit der Implementierung eines speziell entwickelten Mach-Zehnder Interferometers im Front-End des "chirped pulse amplification" (CPA) (Verstärkung Wellenlängen-kodiert gestreckter Pulse) Lasers, konnte ein voll konfigurierbarer Doppelpuls erzeugt werden, der zum optimalen Pumpen eines Röntgenlasers eingesetzt wurde.

Die Mach-Zehnder Einheit ermöglichte die Erzeugung von zwei Pulsen verschiedener Pulsdauer und variablem Energieverhältnis bei einer justierbaren Zeitverzögerung. Die Doppelpuls-Konfiguration wurde neben dem Pumpen von Röntgenlasern auch zur Messung des B-Integrals in zwei verschiedenen CPA Lasersystemen durch Verstärkung von kurzen Pulsreplika, gefolgt von einer zeitlichen Analyse, benutzt. Die Messung von B-Integralwerten von 0,1 bis 1,5 Radians, begrenzt nur durch die zur Verfügung stehenden Laserparameter, zeigt das Potenzial zur Charakterisierung von nicht-linearen Effekten in CPA Lasersystemen.

Zum Pumpen der Röntgenlaser wurde der Doppelpuls derart konfiguriert, dass eine optimale Erzeugung des Lasermediums für die Röntgenverstärkung erreicht wurde. Die Fokussierungsgeometrie der zwei ko-linearen Laserpulse unter demselben streifend auf das Target auftreffenden Einfallswinkel verbesserte signifikant die Erzeugung des aktiven Plasmamediums. Auf der einen Seite wurde der Effekt durch den instrinsisch garantierten exakten Überlapp der zwei Pulse auf dem Target bewirkt, auf der anderen Seite wurde, durch die Erzeugung des Vorplasmas unter streifendem Einfallswinkel, der aktive Bereich des Röntgenlasers zu höherer Elektronendichte verschoben, was eine höhere Verstärkung in länger-welligen Röntgenlasern und eine höhere Effizienz in kürzer-welligen Röntgenlasern zur Folge hatte. Die Erhöhung der Verstärkung konnte durch Plasma-Hydrodynamik-Simulationen bestätigt werden.

Die erste Anwendung des Doppel-Kurzpuls-Einzelstrahl-Pumpens unter streifendem Einfallswinkel für Röntgenlaser unterhalb von 20 Nanometern in der Laseranlage PHELIX in Darmstadt (Deutschland) resultierte in einem verlässlichen Betrieb eines Nickel-ähnlichem Palladium-Röntgenlasers bei 14.7 Nanometern mit einer stark reduzierten Pumpschwellenenergie von weniger als 500 Millijoule. Mit der Anpassung des Konzepts zum Doppelpuls-Einzelstrahl-Pumpen unter streifendem Einfall (Abkürzung: DGRIP) und dem Transfer dieser Technologie zur Laseranlage LASERIX in Palaiseau (Frankreich), konnte die Effizienz und Stabilität des hoch-repetierenden "table-top" Röntgenlasers im Wellenlängenbereich unter 20 Nanometern gesteigert werden. 2 Microjoule Röntgenlaserenergie basierend auf Nickel-ähnlichem Molybdän bei 18.9 Nanometern wurde mit einer Gesamtpumpenergie von weniger als 1 Joule auf dem Target bei 10 Hertz Repetitionsrate erzeugt, was die Attraktivität für einen Betrieb bei hoher mittlerer Leistung zeigte. Die einfache und schnelle Justageprozedur erfüllt die Voraussetzungen für eine technisch ausgereifte Installation, und die hoch-stabile Ausgangsenergie den Wunsch nach einer verlässlichen, starken Röntgenlaserquelle. Die Qualitäten des DGRIP-Schemas wurden schließlich durch den Bestrahlungsbetrieb von Nutzerproben mit über 50.000 Schüssen bestätigt, was einer akkumulierten Dosis von $\sim$ 50 Millijoule entsprach.

Die Erzeugung von Doppelpulsen mit hohen Energien von bis zu 120 Joule ermöglichte den Röntgenlaserbetrieb bei noch kürzeren Wellenlängen in der Laseranlage PHELIX. Diese Anwendung des DGRIP Schemas bewährte sich als einfache und effiziente Methode zur Erzeugung von Röntgenlasern unterhalb von 10 Nanometern. Beim Nickel-ähnlichen Samarium-Röntgenlaser bei 7.3 Nanometern konnte eine Pumpschwellenenergie von nur 36 Joule erreicht werden, was die Tauglichkeit des angewandten Pumpschemas zeigte. Durch die Einzelstrahl-Pumpgeometrie wurde ein verlässlicher und stabiler Röntgenlaserbetrieb trotz großer Optik-Aperturen erreicht. Das Beispiel des Nickel-ähnlichen Samarium-Röntgenlasers war ein wichtiger Meilenstein für die Eignung dieses Pumpschemas auch bei hohen Pumplaserenergien, die notwendig sind, um Röntgenlaserwellenlängen im Wasserfenster zu erreichen. Die Reduzierung der Gesamtpumpenergie unter 40 Joule für den 7.3 Nanometer kurzen Röntgenlaser erfüllt nun die Voraussetzungen für eine Installation im hoch-repetierenden Betrieb der Laseranlage LASERIX.

Contents

List of Figures

List of Tables

Chapter 1

Introduction and Principle of Transient Collisionally Excited Plasma Soft X-Ray Lasers

1.1 Introduction

The demonstration of the first LASER (Light Amplification by Stimulated Emission of Radiation) 50 years ago, operating at 694.3 nm in ruby was a huge breakthrough (Mai60). Immediately, many new laser schemes followed and a dramatic development was launched. Since the invention of the laser, the expansion of the spectral range especially to the shorter wavelength was difficult. The shortest wavelength of commercially available laser systems today is still at 157 nm. Further wavelength reduction is achieved mainly by huge, accelerator-based free-electron lasers, reaching down to 0.1 nm. However, in the last few years remarkable progress was made towards new concepts for laboratory-scale, so called table-top extreme ultraviolet or soft x-ray lasers with promising high average brilliances. Applications of such compact short-wavelength lasers are coming up rapidly for micro- and nanotechnologies of the present century. In this thesis the newest developments of this kind of short wavelength laser scheme are presented.

One of the most exciting research areas in this field are sources of coherent short-wavelength radiation with wavelengths between 2 and 60 nanometers. As this spectral region touches the soft x-ray range, these sources have been termed as Soft X-Ray Lasers (SXRL), even if the research is dominantly performed in the EXtreme

UltraViolet (XUV or EUV). With the first soft x-ray laser demonstration 25 years ago, pumped by a large-scale infra-red laser (MHR+85), numerous successful soft x-ray lasers were developed with remarkable results. Bright coherent short wavelength sources which are available now can be separated in three categories of fundamental processes for the generation of coherent soft x-rays: free electron lasers (FEL), high-order harmonics (HOH), and plasma-based soft x-ray lasers (Plasma SXRL). Rapid progress was enabled by developments in electron beam technology as well as progress in high-power lasers.

1.1.1 Free electron lasers

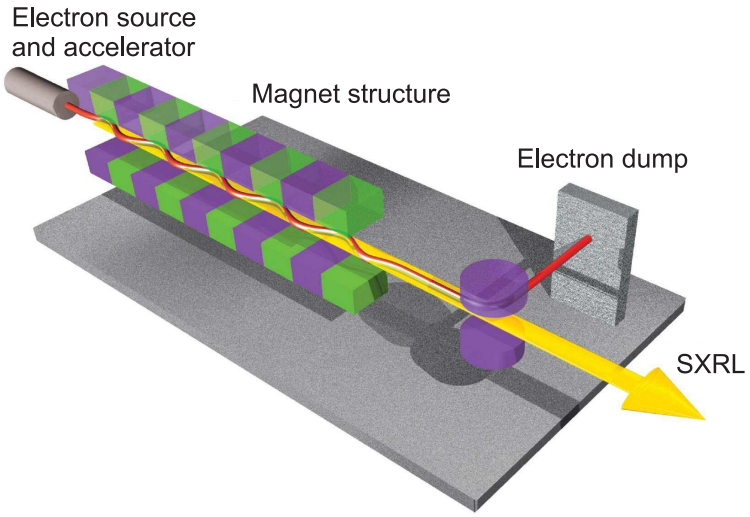

Figure 1.1: Schematic description of a free electron laser which induces the generation of soft x-rays by the propagation of an electron beam through an undulator (MAHM+07).

Free electron lasers (FEL) are based on beams of electrons, accelerated to almost speed of light, and guided through an undulator. This arrangement of periodic, transverse magnetic fields, generated by alternating magnetic poles, leads to the acceleration of the electrons in a sinusoidal path resulting in the generation of coherent soft x-ray radiation. Due to their huge size only two facilities operating in the x-ray regime on the SASE FEL principle are present today, the Free electron LASer in Hamburg (FLASH) and the Linac Coherent Light Source (LCLS) at the SLAC National Accelerator Laboratory. Typical soft x-ray pulses of FLASH with a tun-

able wavelength of 7-50 nm reach energies of 10-100 μJ in 10-100 fs (AAA$^+$07), while the x-ray pulses of LCLS reach down to 0.1 nm with similar pulse characteristics (Emm09).

1.1.2 High-order harmonics

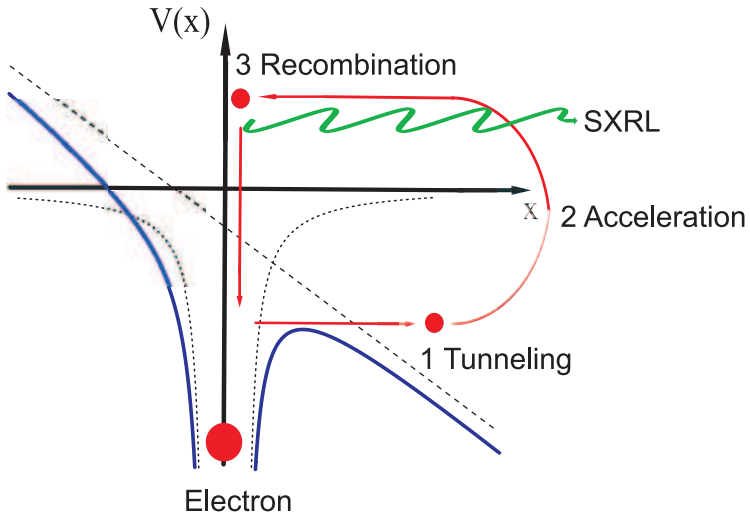

Figure 1.2: Schematic description of high-order harmonic generation in a semi-classical three-step model (Eck09).

High-order harmonic (HOH) sources are generated by nonlinear effects occurring in the interaction of linearly polarized short laser pulses with gases or solids. Odd multiples of the laser frequency, called harmonics, are obtained in this way. High-order harmonics provide a tunable table-top soft x-ray source with a high beam quality and a spatial coherence making HOHs ideal seed laser sources, which can be injected into high-gain plasma-based soft x-ray laser amplifiers. High-order harmoics were achieved with wavelengths down to 1 nm (SSV$^+$05), and pulse durations of $\sim$ 100 as (SME$^+$06), but in both cases with very limited photon numbers. The highest high-order harmonic pulse energy below 25 nm was achieved by (KLP$^+$08) with $\sim 0.6\,\mu J$.

1.1.3 Plasma soft x-ray lasers

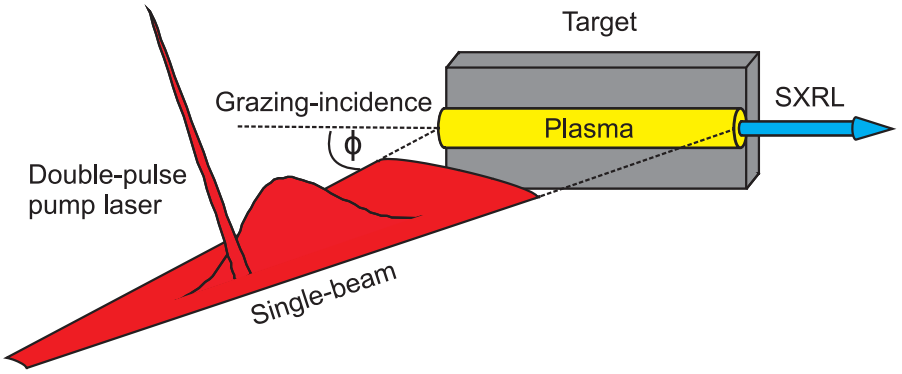

Figure 1.3: Schematic description of a plasma soft x-ray laser which is pumped by laser double-pulses.

The plasma-based soft x-ray lasers were one of the first ideas proposed to generate coherent soft x-ray radiation via population inversion in a plasma gain medium. Many population inversion mechanisms have been considered to produce the lasing effect in the soft x-ray range. Among these, the two which were investigated most profoundly, were the recombination scheme (SSM$^+$85) and the collisional excitation scheme (MHR$^+$85), both involving highly charged ions in a dense plasma filament. But only the last one succeeded to produce large gain coefficients in laser-produced plasmas, leading to saturated SXRL emission (ZML$^+$97). Its investigations were based on line-shaped focalization of infra-red lasers on solid targets. Indeed, to obtain strongly amplified soft x-ray emission, it is necessary to achieve plasma conditions producing at the same time a large fraction of the lasing ions and a large population of high-energy electrons, leading to a strong monopole collisional-excitation rate from the ground state. Several scenarios using either pump laser pulses of duration between 1 ns and 30 fs or even electric discharges in plasmas may be employed to produce SXRL emission. Thus, different SXRLs can be realized with different properties in terms of photon number or output energy, duration, and optical quality (spatial and temporal coherence). Basically, the use of discharge plasmas resulted in fast capillary discharge SXRLs (BMBR97), while the use of long laser pulses lead to so-called Quasi-Steady State (QSS) SXRLs (MHR$^+$85), and ultra-short, circularly polarized pulses were able to drive SXRLs in plasmas produced by optical field ionization (OFI) (SHB$^+$01). Between these two extreme situations, picosecond pulses

gave rise to the class of soft x-ray lasers, based on the Transient Collision Excitation (TCE) scheme (NSK$^+$97).

Capillary discharge SXRL

The excitation of plasma with an electric discharge is a compact and efficient method to create quasi-steady state soft x-ray lasers. A cylindrical plasma is created in this case by an electrical discharge, which reaches the required temperature and density by compression on the cylindrical axis, followed by a stagnation process. In this way a high pumping efficiency in a high density plasma is obtained together with a high axial uniformity. The capillary discharge lasers with a length of several tens of centimeters are e.g. argon filled at ~ 1 bar and driven by currents up to $\sim$ 100 kA. Saturated output in Ne-like Ar at 46.9 nm with a pulse duration of 0.8 ns and repetition rate of 4 Hz has been demonstrated. The set-up of (MBR99) delivers highly spatially coherent pulses with an average power of ~ 3.5 mW, one of the highest average output powers available in the soft x-ray regime. However, this scheme has so far not been extended to wavelengths shorter than 46.9 nm, which limits its application.

Optical-field ionization SXRL

The optical-field ionization (OFI) occurs when a high-intensity, ultra-short laser pulse irradiates a gas target and ionizes atoms in the tunnel regime. The oscillatory electric field of the laser pulse has to be comparable or higher than the electron attractive Coulomb forces of the nucleus, to reduce the potential barrier and enable the ionization process by tunneling or Barrier Suppression. Generally, optical-field ionization soft x-ray lasers have the advantage of strongly reduced pump laser energy requirements, because the mechanism is favored by the high laser pulse intensity. The low pump energy requirements allow for very high repetition rate operation. In the recombination OFI scheme reasonable lasing was obtained at 13.5 nm on the Lyman-α transition of Li^{2+} by (NMK$^+$93),(KBSR97), while in the collisional OFI scheme Ni-like Kr at 32.8 nm was demonstrated with a high gain of 78 cm^{-1} by (SMR$^+$02). Currently OFI SXRLs are limited in pulse energy to $\sim$ 100 nJ, which complicates their application.

Quasi-steady state SXRL

The Quasi-steady state (QSS) soft x-ray lasers are produced by irradiation of slab targets with energetic (100 to several 1000 J) and long (0.3-1 ns) laser pulses. The first soft x-ray laser was demonstrated in this way by (MHR$^+$85). Later the idea came up to separate the production of the high abundance of Ne- or Ni-like ions, and the creation of the population inversion within the ion abundance, by applying several pumping pulses (MEP$^+$93) and (NM95). Up to three low energetic pre-pulses with the same pulse duration were preceding the main pulse to pre-heat the target. This created small density gradients, the required ionization state and optimum conditions for the main heating pulse to generate lasing in a more efficient way. The application of this method resulted in the first saturated soft x-ray laser at 7.3 nm (ZML$^+$97) and in the shortest saturated SXRL at 5.8 nm (STZ$^+$99). The highest output energy of ~ 4 mJ was achieved at 21.2 nm by (RMP$^+$02), while the shortest wavelengths were reaching down to 3.6 nm (MMDS$^+$90). With the high efficiency of $\sim 10^{-5}$ QSS SXRLs are very suitable for applications, but the repetition rate is limited to about one shot per 30 min restricting the applications to single shot operation.

Transient collisional excitation SXRL

Even though the pump laser energies in the QSS scheme have been reduced to a level around 100 J, this is still too much for the table-top operation in smaller laboratories. With the transient excitation the first low pump energy soft x-ray laser was obtained by (NSK$^+$97) with only 15 J. In the transient collisional excitation (TCE) scheme, two laser pulses with different pulse parameters are applied. The first typically nanosecond long pulse, called pre-pulse, produces the plasma with an abundance of the required ionization stage (Ne- or Ni-like), similar to the QSS scheme. After an optimized delay necessary for the plasma expansion, a second pulse, called main pulse, with a short picosecond duration generates a transient population inversion by electron collisional excitation. The rapid heating process does not influence the ionization balance, because of the negligible kinetic relaxation and hydrodynamic expansion. With this technique high gain is produced in a very short time scale of several picoseconds. Due to the high gain of up to $100\,cm^{-1}$, saturated output could be obtained with plasma lengths below 10 mm and less than

10 J total pump energy, allowing for the operation of table-top soft x-ray lasers. The first table-top saturated TCE SXRL was reported in Ni-like Pd at 14.7 nm by (DOS$^+$98). The shortest wavelength realized in the TCE regime was achieved in Ni-Sm at 7.3 nm pumped with a still rather high pump laser energy of $\sim$ 70 J by (KPM$^+$01).

Grazing incidence pumping SXRL

A huge step for the reduction of the total pump energy requirement for TCE SXRLs was the introduction of the GRazing Incidence Pumping (GRIP). It enabled lasing in Ni-like Mo with energies as low as 150 mJ (KDP$^+$05), and with energies about 1 J the operation in the saturated regime (LWL$^+$05). With such small total pump energies, laser systems could provide soft x-ray lasing at repetition rates of 10 Hz (KDP$^+$05) and energies up to 2 μJ (CKR$^+$07). Saturated soft x-ray lasing in several Ni-like ions were achieved with Mo at 18.9 nm, Pd at 14.7 nm, Ag at 13.9 nm Cd at 13.2 nm and down to Te at 10.9 nm with small pump energies below 5 J (AMW$^+$10). With average powers up to $\sim$ 20 μW at 18.9 nm (10 Hz) (CKR$^+$07) and 13.9 nm (2.5 Hz) (MAL$^+$10) the attractiveness for applications of table-top GRIP SXRLs was considerably increased.

1.1.4 Specificity of plasma soft x-ray lasers

Comparing different soft x-ray lasers sources requires a good knowledge of their radiative properties like pulse energy, duration, bandwidth, source size, beam divergence as well as spatial and temporal coherences. The brilliance B is often used to benchmark soft x-ray sources giving the number of photons per ($s\,mm^2\,mrad^2$) in 0.01% bandwidth. High values of peak brilliance are required for many applications and an overview of the peak brilliances of existing complementary soft x-ray sources together with collisionally excited plasma SXRLs is shown in Fig. 1.4. Since the peak brilliance of plasma-based SXRLs is currently not yet competitive with free electron lasers, one has to consider as well the average peak brilliance. Here, the plasma-based soft x-ray lasers can nearly reach the values of FELs, since the necessary high repetition-rate pump laser systems are available soon. Picosecond pump laser systems exceeding 100 Hz at the joule energy level will be realized by the diode-pumped solid-state laser technology showing promising improvements (TJS$^+$09).

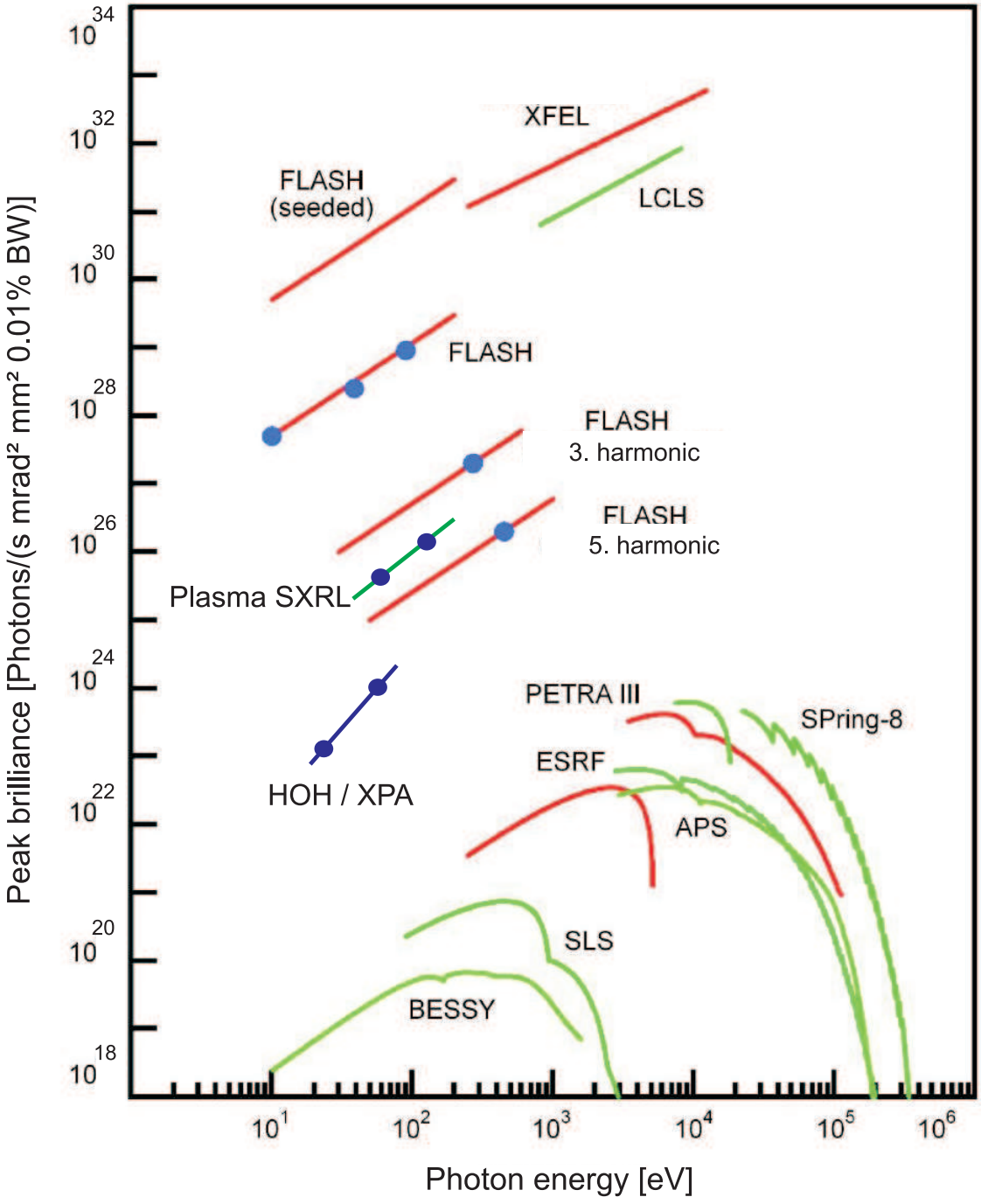

Figure 1.4: The peak brilliances of different soft x-ray sources, synchrotrons, free-electron lasers, high-order harmonics and plasma soft x-ray lasers, are presented, showing the potential of plasma SXRLs as laboratory-scale bright coherent sources (MAHM+07),(WGP+08).

The two main complementary soft x-ray sources namely free-electron lasers and high-order harmonics give outstanding resolution in the time domain, but cannot offer high spectral resolution with high peak brilliance in the intermediate regime at wavelengths below 20 nm. Here the plasma soft x-ray laser is filling this gap with relative spectral bandwidth better than 10^{-4} and peak brilliance of $\sim 10^{26}$ photons$/(s\,mm^2\,mrad^2)$ in 0.01% bandwidth.

Owing to the high peak brightness, laser produced plasma soft x-ray lasers are versatile diagnostics tools for interferometry, microscopy and reflectometry (ZAJ+98), (RMMK99). Large plasmas of up to 3 mm size with high electron densities of $n_e > 4 \times 10^{21}\,cm^{-3}$ can be probed by SXRLs, while optical lasers cannot propagate through these kinds of plasma, due to the lower critical density at the longer wavelength. For the diagnostics of Warm Dense Matter, plasmas at approximately solid state density and temperatures in the range between 1 eV and 100 eV, Thomson scattering with a *narrow bandwidth* and *short wavelength* laser source can yield information on the plasma temperature and density (RDM+07). Short wavelength is required to penetrate through high density plasma, whereas the narrow bandwidth of the plasma SXRL is a prerequisite for the spectral analysis.

Imaging of biological samples requires SXRLs operating in the water window between 2.3 and 4.4 nm. In this wavelength region the contrast between water- and carbon-containing samples (DNA, proteins, etc.) is very high and in-situ microscopy of wet samples is possible (DSTB+92). For maximization of the scattering in the soft x-ray holography in carbon structures, reducing the necessary dose per cell, a wavelength slightly longer than the carbon edge is interesting. In context of the upcoming EUV lithography at a wavelength around 13.5 nm, Ni-like Cd SXRLs at 13.2 nm represent an attractive diagnostic source for lithography facilities (BWB+09). High repetition rate SXRL systems are also very promising for material science such as photo-electron spectroscopy.

The precise knowledge of the wavelength and its narrow bandwidth of $\Delta\lambda/\lambda \sim 10^{-5}$ together with reasonable photon numbers of 10^{12} allows for spectroscopy even of highly charged ions (KUB+07b). Another type of experiments like nonlinear optics in the soft x-ray regime requires a sufficiently high SXRL intensity, which can be delivered at the short wavelength by suited focusing optics (JCJ+99).

To summarize, the table-top soft x-ray laser sources presented here, operating around 10 nm at 10 Hz repetition rate with pulse energies of about 1 μJ, present a highly

desirable tool for applications in spectral regions where wavelength matches the geometrical dimensions of the micro- and nano-objects in the technologies of the current century.

1.2 Principles of transient collisionally excited plasma soft x-ray lasers

1.2.1 Pump energy absorption in the active medium

The active medium of a soft x-ray laser is a plasma consisting of highly charged ions and free electrons with an electron density of $\sim 10^{19}-10^{21}\,cm^{-3}$ and an electron temperature of $\sim 100-1000\,eV$. The transitions between the energy levels of the ions are responsible for the operation at such short wavelengths. The plasma is created by laser interaction with solids with intensities varying between $\sim 10^{11}-10^{17}\,W/cm^2$. The pump laser energy is converted with a certain efficiency into thermal energy, ionization energy and kinetic energy of the plasma expansion. The ablated material is vaporized and dominantly heated by the "Inverse Bremsstrahlung" mechanism and ionized by collisional impact or multi-photon ionization.

A laser pulse with wavelength λ can only penetrate through the under-dense plasma up to the critical electron density n_c:

$$n_c[cm^{-3}] = (\epsilon_0 m_e/e^2)\omega_p^2 = 1.1 \times 10^{21}/\lambda^2[\mu m] \tag{1.1}$$

with the dielectric constant ϵ_0, the electron mass m_e, the electric charge e and the angular frequency ω_p.

The laser energy is dominantly absorbed at the critical density, and the electrons are mostly heated in this region called coronal zone. The density profile of the plasma plume is decreasing with expansion, while the temperature profile is rising to a maximum and falls by adiabatic expansion and thermal conduction, as shown in Fig. 1.5. A shock wave is generated in the interaction process which propagates towards the target. The zone of interest for the SXRL amplification is located in the coronal zone characterized by sufficiently high electron density and temperature.

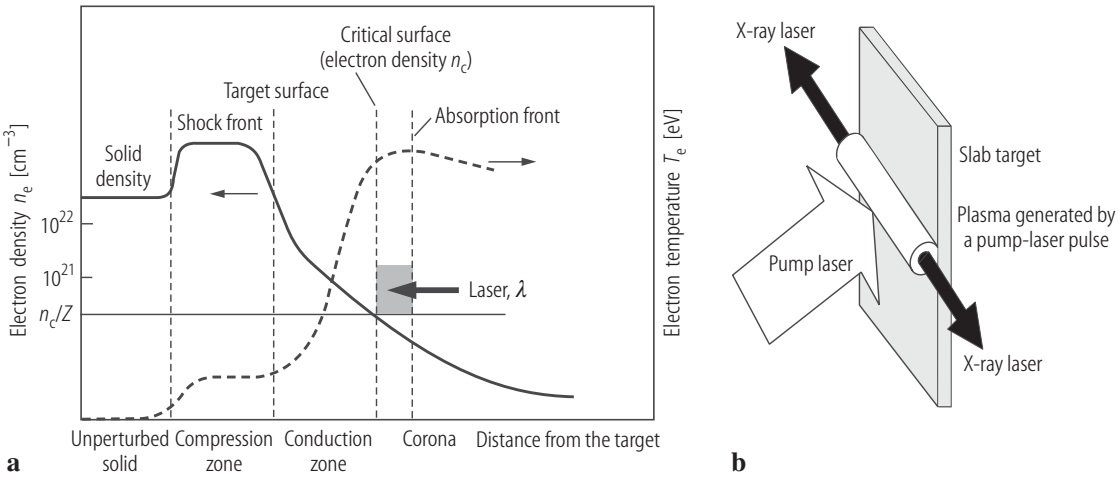

Figure 1.5: On the left-hand side the electron density and temperature for a typical laser-produced plasma are shown for the direction normal to the target. On the right hand side a typical set-up is shown with the cylindric plasma column on a slab target which is irradiated by the pump laser (NJS08).

1.2.2 Population inversion and gain

The plasma gain medium with its highly ionized atoms is not stable in time, but specific compositions of ion species have lifetimes up to several nanoseconds. The species required for the lasing transition has to have a certain abundance in the plasma. In order to create a population inversion in the specific ions the ionizaton balance has to be reasonably stable, which is given in ions with closed electronic shells or sub-shells. Therefore the active medium uses dominantly one ionization stage to produce lasing with a reasonably efficient collisional-radiative cascade after a recombination process with a long-lived level at its end, which becomes the upper laser level. Ion isotronic sequences fulfilling these requirements are He-like (n=2), Ne-like (n=10), Ni-like (n=28) and Pd-like ions (n=46).

Population inversion is typically realized in a three-level scheme embedded in the reservoir of energy levels of the e.g. Ni-like ions. The upper laser level is populated by collisions with electrons from the ground-state level, while the direct transition from the upper level into the ground state is forbidden (metastable), and the lower laser level empties rapidly by radiative or collisional processes.

The gain, given as the small-signal gain coefficient $g(\nu)$, describes the amplification in the system without considering its origin. The product of the stimulated emission

cross section σ and the density of the population inversion $\Delta N = (N_u - N_l \frac{g_u}{g_l})$ of the lasing transition with the population of the upper and lower laser level N_u and N_l, respectively, determines the gain factor to

$$g(\nu) = \sigma \times \Delta N \approx (A_{ul}\lambda^2/8\pi\Delta\nu) \times (N_u - N_l\frac{g_u}{g_l}). \tag{1.2}$$

With the Einstein coefficient for spontaneous emission $A_{ul} \propto \lambda^{-2}$ and the neutral line width $\Delta\nu \propto A_{ul}^{-1}$ follows

$$g(\nu) \propto \Delta N\lambda^2 \propto N_u\lambda^2. \tag{1.3}$$

Here, the gain increases with the plasma electron density n_e, but it is limited by electron collisions that can thermalize the laser levels and destroy the population inversion.

1.2.3 Kinetics of the active medium

The temporal changes in the populations of the ion levels in the active medium are influenced by ionization, recombination, collisional excitation, de-excitation and radiative decay and described by the rate equations for the population density N_{nZ} of an energy level with the electronic state n of ions with the charge Z:

$$\frac{dN_{nZ}}{dt} = \Sigma_i N_{iZ}\Gamma_{in} - N_{nZ}\Sigma_i\Gamma_{ni} + R_{nZ+} - R_{nZ-}. \tag{1.4}$$

The first and second term are the positive and negative contribution of electrons from other levels of the same ion with the rates Γ_{in} and Γ_{ni}, respectively. To simplify the equation only collisional ionization and recombination are accounted for, and the radiative part is neglected. By choosing the ion species of interest (e.g. Ni-like) and separating the rate equations including the creation of other ion species, one finds:

$$\frac{dN_n}{dt} = \Sigma_i N_i S_{in} - N_n\Sigma_i S_{ni}, \tag{1.5}$$

with the population N_n and total transition probability $S_{in} = S_{in}(Z, n_e, T_e)$.
The ion species concentration ϵ_Z can be written as the ratio of the given ion species density to the total ion density

$$\epsilon_Z = \frac{\Sigma_n N_{nZ}}{\Sigma_n\Sigma_Z N_{nZ}}, \tag{1.6}$$

and the dynamics of the ion creation as

$$\frac{d\epsilon_Z}{dt} = [\epsilon_{Z-1}C^I_{Z-1} + \epsilon_{Z+1}C^R_{Z+1} - \epsilon_Z(C^I_Z + C^R_Z)]n_e, \tag{1.7}$$

with the ionization rate C_Z^I and recombination rate C_Z^R. Together with the hydrodynamic equations for a given n_e and T_e distribution, the description of the ionic system is a multi-parameter problem. To solve this, different approximations can be applied which fit the characteristic times of the process (τ_{hyd} of the hydrodynamic changes in the plasma, τ_I of the ionization and τ_r of the relaxation of excited electronic levels). Here the non-stationary, transient approximation is better suited than the steady-state and the quasi steady-state cases:

$$\frac{d\epsilon_Z}{dt} \neq 0 \quad and \quad \frac{dN_n}{dt} \neq 0, \tag{1.8}$$

with the assumption of constant n_e and T_e.
The transient approximation describes the situation in which the population and the ionization stages do not have enough time to stabilize on the hydrodynamic evolution time scale. At the time $t = 0$ the electron temperature increases rapidly and after this rise time, T_e and n_e can be considered as constant, as $\tau_{hyd} < \tau_I$ and τ_r, i.e. the rise time is comparable to the inter-atomic relaxation time. Typically the highest gains are achieved in this regime with values of $g \sim 10 - 100\,cm^{-1}$.

1.2.4 Medium size, output geometry and refraction

The active medium with its high pump power densities and its small optical thickness in the transverse direction of the plasma column, can typically only be realized in small volumes. With a width d of 10-200 μm and a length L of 1-20 mm, this results in an aspect ratio of $\sim 1:1000$, which determines the maximal divergence Θ of the output beam of the transversely pumped SXRL in the range of $\sim$ 1-10 mrad. The values strongly depend on the applied pump power and often limit the effective gain length of the active medium. In general it is desirable to maximize the aspect ratio by increasing the gain length, improve the transverse spatial coherence and to operate in the saturated regime.
The sufficient propagation of the SXRL beam along the plasma line is required for a high output level and a reasonable collimation at a preferably high plasma density to increase the gain. Density inhomogeneities should be minimized, since the SXRL is deflected by the refraction index gradients ∇n of the plasma density gradients ∇n_e:

$$\nabla n = -\frac{1}{n}\frac{\nabla n_e}{2n_c}, \tag{1.9}$$

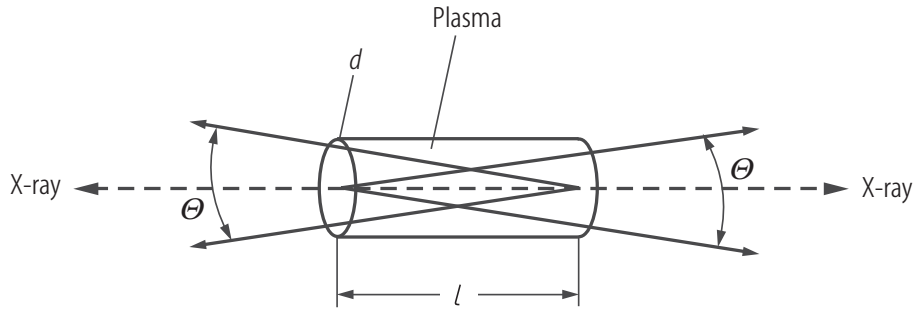

Figure 1.6: The divergence of the SXRL beam Θ is determined by the size of the medium with the aspect ratio d/l (NJS08).

with the refraction index in the plasma

$$n = \sqrt{1 - \frac{n_e}{n_c}} \tag{1.10}$$

and the plasma electron density n_e and the critical plasma density n_c.
Typical values of the refraction gradient in the region of high amplification for the SXRL wavelength are in the order of $\nabla(n_e/n_c) \sim 10^{-3} - 10^{-4}\mu m^{-1}$ normal to the target surface. Since the high-gain zone in the plasma has only a narrow spatial extent (several tens of microns), the SXRL beam suffering from refraction is easily bent out of the gain zone, limiting the total accessible gain length. The refraction length can be expressed as

$$l_{ref} = l_x(n_c/n_{oe})^{1/2} \tag{1.11}$$

with maximum electron density $n_0 e < n_c$ and the transversal extension of the gain region l_x with the refraction angle

$$\Theta_{ref} = (n_c/n_{0e})^{1/2}. \tag{1.12}$$

This results in an effective gain g_{eff} reduction for a plasma length $l_z > l_{ref}$ of

$$g_{eff} = g - \frac{1}{l_{ref}}. \tag{1.13}$$

Several techniques are applied to reduce or to compensate for the refraction in the plasma, e.g. foil targets to smooth the density profile or curved targets to retain the bent SXRL. However, the technique which is most commonly applied is using pre-pulses of low laser intensity preceding the actual pump pulses.

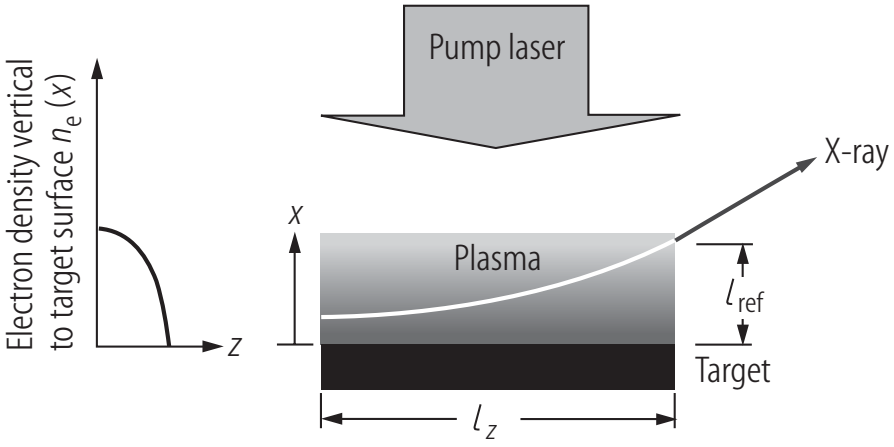

Figure 1.7: The refraction of the SXRL beam in a plasma is caused by the density gradient normal to the propagation direction (NJS08).

1.2.5 Electron collisional excitation

The collisional excitation is the most applied pumping mechanism due to its robustness. The excitation process can be expressed as

$$Z_0^{i+} + electron \rightarrow Z_u^{i+}$$

with Z^{i+} as an i-fold ionized atom with the atomic number Z in which the ground state (0) is excited to the upper state (u). Energetic free electrons collide with the ions in the plasma and transfer part of their energy to the ion by populating the upper and lower lasing levels. Since the radiative decay for the lower laser level is strong compared to the one from the uppper laser level, an inversion population is achieved. The pumping rate for this collisional excitation is proportional to the square of the electron density. Suitable conditions are fulfilled only in transitions of Ne-like and Ni-like isoelectronic sequences.
The lasing transitions in the neon-like scheme are taking place in the (n=3) $1s^2 2s^2 2p^5 3p \rightarrow 1s^2 2s^2 2p^5 3s$ transitions. The largest population inversion can be produced for three transitions:

$$3p(1/2,1/2)_{J=0} \rightarrow 3s(1/2,1/2)_{J=1},$$

$$3p(1/2,3/2)_{J=1} \rightarrow 3s(1/2,1/2)_{J=1},$$

$$3p(3/2,3/2)_{J=2} \rightarrow 3s(1/2,1/2)_{J=1},$$

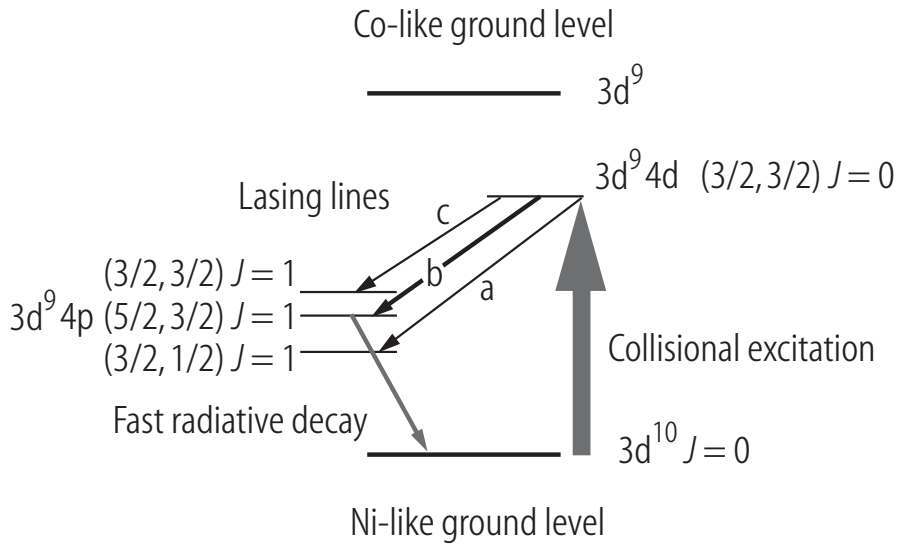

Figure 1.8: The energy level diagram of a nickel-like soft x-ray laser plasma (NJS08).

with the jj-coupling referring to the angular momenta of the core and of the excited electrons and J the total angular momentum of the level (j,j).
A more common configuration is the Nickel-like scheme, in which the lasing transitions are located on the (n=4) $3d^9 4d - 3d^9 4p$ transitions as shown in Fig. 1.8. The $4d$-levels are metastable regarding the radiative decay to the $3d^{10}$ Ni-like ground state, while the p-levels are rapidly depopulated. As a remark, the electron temperature for populating the upper laser level is twice as high as the one needed for producing the Ni-like ion abundance. The strongest gain is obtained in three $J = 0 - 1$ transitions:

$$4d(3/2,3/2)_0 \rightarrow 4p(3/2,1/2)_1,$$

$$4d(3/2,3/2)_0 \rightarrow 4p(5/2,1/2)_1,$$

$$4d(3/2,3/2)_0 \rightarrow 4p(3/2,3/2)_1.$$

The Ni-like scheme is also favorable for short wavelength operation as shown in Fig. 1.9 compared to Ne-like schemes.
The requirements for efficient collisional pumping can be summarized as:

- reasonable abundance of lasing ions (e.g. Ni-like ions)
- sufficiently high electron density to obtain large collisional pumping rates
- suitable electron temperature to efficiently populate the upper lasing level, which is in the best case slightly higher than the excitation energy of the upper laser level

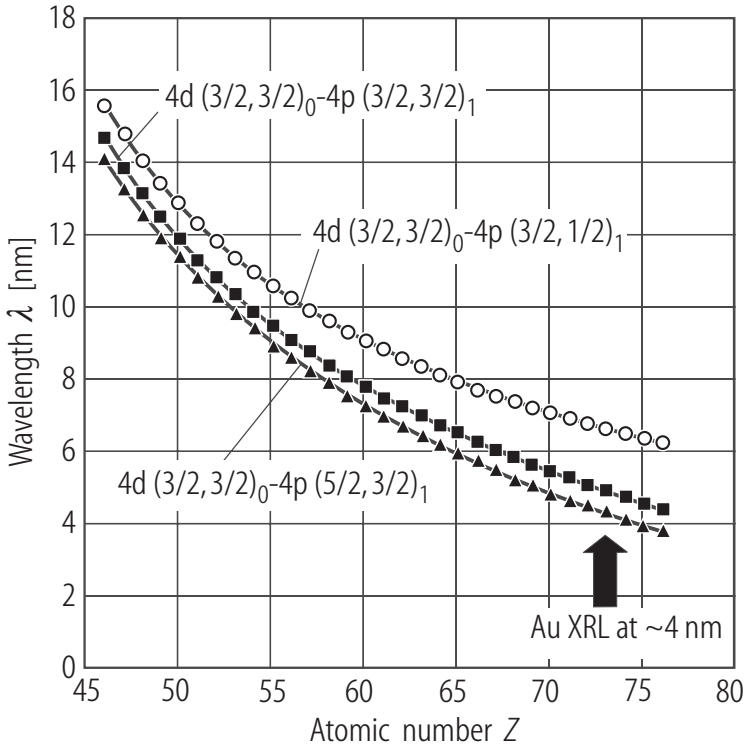

Figure 1.9: The wavelength scaling for the Ni-like isoelectric sequence of the 4d-4p transition (NJS08).

- suitable plasma conditions to provide a low opacity for depopulation radiation of the lower laser level
- not too high plasma density, which would result in strong de-population by electron collisions
- rather smooth density gradients allowing for low refraction of the SXRL beam in the gain region

1.2.6 Output intensity and efficiency

Typically the SXRL operates as super-radiator in the regime of Amplification of Spontaneous Emission (ASE) in a gain medium with the length l, due to the short inversion lifetime, and since there are no efficient mirrors for the operating wavelength. The spectrally integrated intensity of the laser signal grows exponentially with l, until saturation, expressed by the Linford formula for narrow Doppler

broadened line profiles (LPSS74), (TF00):

$$I = \frac{\epsilon_s (e^{g_0 l} - 1)^{3/2}}{g_0 (g_0 l \, e^{g_0 l})^{1/2}}, \tag{1.14}$$

with g_0 and ϵ_s as the gain coefficient at the line center and the emissivity per length, respectively. The emissivity is the spectrally integrated emitted energy per volume and time $N_u A_{ul}$.
The conversion efficiency $\nu = E_x/E_p$ of pump energy E_p into SXRL output energy E_x is in the order of 10^{-6}, resulting in SXRL energies of microjoules for pump laser energies of joules.

1.2.7 Saturation

The saturated operation is the most efficient energy extraction from a laser medium, but also gives constraints to the exponential increase of the output energy with the plasma length. The saturation intensity is defined as the intensity for which the actual gain $g(\nu)$ is reduced by a factor of two. The saturated intensity is determined by equating the non-negligible stimulated emission rate to the pump rate of the upper laser level:

$$I_s = 8\pi h \nu^3 \Delta\nu / c^2, \tag{1.15}$$

with $\Delta\nu$ as the FWHM of the line profile, ν the laser frequency, h the Planck's constant and c the speed of light. The collisionally excited SXRL usually operates at saturation intensities of $10^{10} - 10^{11}\, W/cm^2$, but one has to remark that this intensity is not an upper limit, it is only the starting point of efficient energy extraction from the gain medium. One can assume that the gain saturation is achieved when the gain-length product $gl > 15$ (LPSS74).

1.2.8 Wavelength, spectral line width and pulse duration

Collisionally pumped SXRLs were demonstrated at wavelengths between 3.56 nm (Ni-like Au) and 60.8 nm (Ne-like S), while shorter wavelengths are not yet realized, due to the very high pump energy requirement. An overview of the shortest wavelength soft x-ray lasers in the collisional excitation scheme is given in Table. 1.1. The line width of the laser transition is dominated by Doppler broadening due to the thermal motion of the ions with the kinetic energy kT_i, which results in the

Gaussian-shaped line profile half width of:

$$\Delta\lambda_d/\lambda_d = 7.7 \times 10^{-15}(kT_i/2Z)^{1/2}, \tag{1.16}$$

with kT_i in eV and Z the charge number. A factor of $\sim 1/\sqrt{gl}$, reflecting the gain narrowing effect, has to be taken into this consideration. Typical line widths are $\sim 10^{-4} - 10^{-5}$, with the smallest measured line width of Ni-like Pd of 2×10^{-5} (SDH$^+$03a).

The pulse length of an SXRL depends on the gain duration, which strongly depends on the excitation scheme and pump parameters (AATE$^+$03). Picosecond pumping of transient excited SXRLs typically results also in picosecond pulse durations, with the shortest measured pulse duration to date in Ni-like Ag of 2 ps (KGR$^+$06).

1.2.9 Coherence

The coherence is determined by the propagation process of the SXRL beam in the plasma amplifier, and one has to distinguish between spatial and temporal coherence. The degree of coherence is important for applications involving interference effects and sets limits to the brightness and focusability of the SXRL beam. In the ASE regime, and because the aspect ratio is such that the Fresnel number is high, the SXRL can be approximated as a source with low spatial coherence. The coherence transverse to the SXRL beam axis is characterized by the extent D_c of a region of coherence at a distance L_d illuminated by a source with the diameter d_s emitting at the wavelength λ_x:

$$D_c \sim L_d\lambda_x/d_s. \tag{1.17}$$

Typical values for spatial coherence can be estimated for a SXRL at 10 nm with a source size of 100 μm at a distance of 1 m to the range of 0.1 mm. This is sufficient for small focal region applications like microscopy. An improvement of the coherence can be achieved by a master oscillator power amplifier set-up, where e.g. a HHG source is injected into the SXR amplifier.

The longitudinal or temporal coherence length is characterized by

$$L_c = \lambda_x^2/\Delta\lambda_x, \tag{1.18}$$

which for a laser wavelength of 10 nm and $\Delta\lambda_x/\lambda = 10^{-4}$ gives 100 μm (t_c=0.3 ps), sufficient for imaging objects larger than 1 μm. A further increase of the temporal coherence can be achieved by a narrower line width of the laser.

Table 1.1: The table presents the most important realized collisionally excited SXRLs below 10 nm together with the main pump laser parameters and the output characteristics.

Year	SXRL Ni-like Z (nm)	Pulses [nm]	Duration [ps]	Delay [ps]	Focus length [mm]	Energy [J]	Intensity $[W/cm^2]$	Gain [1/cm]	gl	Scheme
2004	La (8.8)	1053	200	250	5.3	1	3.0E+12	14.5	8	TCE
		1053	7			16	1.4E+15			
2004	Ta (4.4)	527/1053	100	1500	2 x 6	15	1.3E+13		6	QSS
		527/1053	100			300	2.5E+14			
2001	Sm (7.3)	1060	280	130	10	34	1.0E+13	19.0	15	TCE
		1060	1			36	3.0E+15			
1999	Dy (5.8)	1053	75	2200	2 x 18	12	4.0E+12	9.0	18	QSS
		1053	75			120	4.0E+13			
1998	Ta (4.4)	1053	100	1500	2 x 11	20	1.8E+13			QSS
		1053	100			480	4.4E+14			
1997	Sm (7.3)	1053	75	2200	2 x 18	15	4.0E+12	8.4	15	QSS
		1053	75			150	4.0E+13			
1995	Dy (5.8)	1053	100	400	28	137	7.0E+13			QSS
		1053	100			137	7.0E+13			
1990	Ta (4.4)	530	500		20	5520	4.6E+14	2.3		QSS
1990	W (4.3)	530	500		30	5580	3.1E+14	2.6		QSS

1.2.10 Transient collisional excitation with traveling-wave pumping

With the application of the transient collisional excitation by picosecond short pumping pulses and the generation of a transient population inversion was achieved and the traveling-wave pumping was introduced. Since the life time of the transient gain in the amplifier medium lasts only several picoseconds, the propagation time of the SXRL beam in the plasma is limited. Therefore, it is necessary to increase the effective gain length by using traveling-wave pumping, illustrated in Fig. 1.10. As can be seen there, the pulse front is tilted in such a way that the pump beam travels along the target synchronously with the amplified SXRL beam, enabling the extraction of a short SXRL pulse from the active medium.

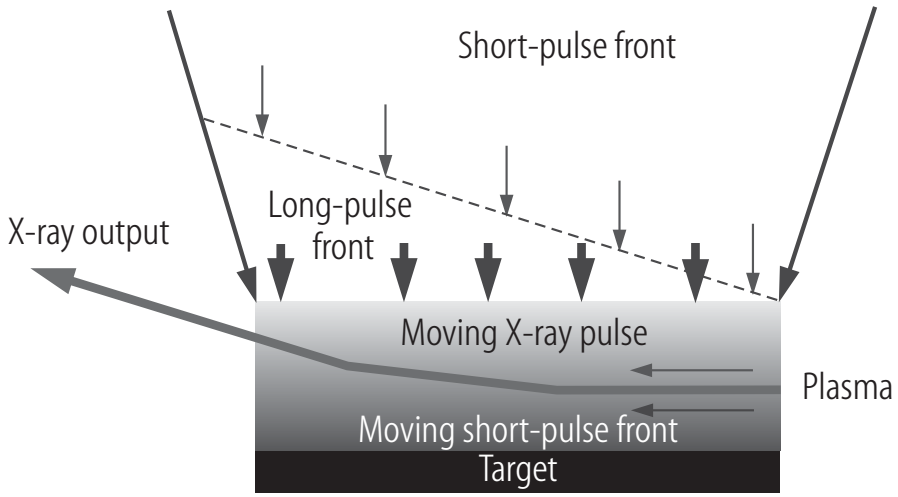

Figure 1.10: The scheme of a transversally pumped SXRL with a traveling-wave introduced by a pulse front tilt of a short pulse (NJS08).

1.2.11 Grazing incidence pumping (GRIP)

The principle of grazing incidence pumping benefits from an oblique irradiation of a slab target by the short main pulse, while the first pulse is still irradiating the target at normal incidence. In this way the main pump beam penetrates a larger volume of the active medium and deposits more energy in the gain zone. In the case of normal incidence, the pump beam is reflected at the critical density n_c and guided out of the plasma after a short interaction path. Under grazing incidence pumping,

the rays are refracted by the density gradients in a large interaction path due to their large incidence angle (Fig. 1.11). Additionally the control over the penetration depth of rays is determined by the grazing incidence angle Φ. The energy deposition is thereby shifted from the critical density to the turning point electron density n_{tp}:

$$n_{tp} = n_c \times (1 - cos(\Phi)^2), \tag{1.19}$$

as shown in Fig. 1.12. With this effect the tuning of the energy deposition at an optimum density region with high gain is possible. Since the turning point electron density is lower than the critical one, an increase of the electron temperature, and thereby gain, can be obtained with the same pump energy. The optimal incidence angle depends strongly on the optimal electron density for the gain zone of the lasing element and on the pump laser wavelength ($n_c \propto \lambda^{-2}$). As an example, an optimal incidence angle for Ni-like Mo was determined to be 19 degrees for a Ti:Sa laser at 805 nm (KCR$^+$08), while an optimum for Ni-like Pd was observed at 29 degrees for a Nd:Glass laser at 1054 nm (ZZB$^+$08).

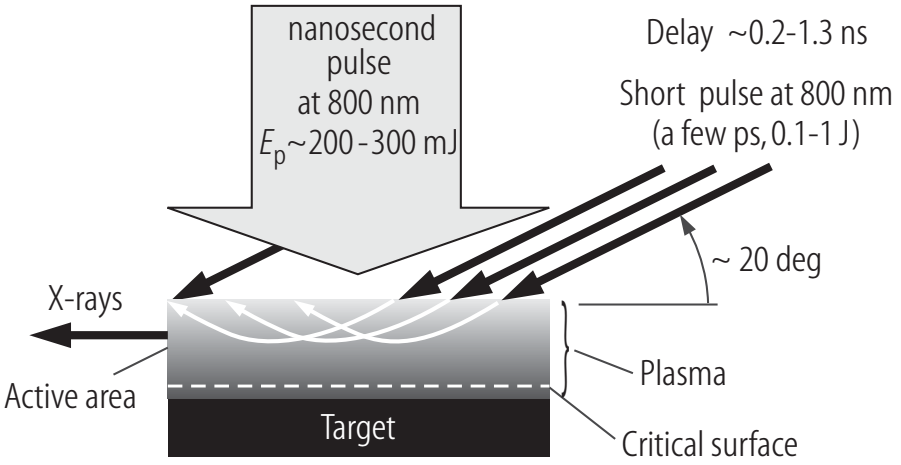

Figure 1.11: The scheme of grazing incidence pumping (GRIP), in which the short pulse is reflected in the active area of the plasma, depositing its energy mostly at the turning point denisty (NJS08).

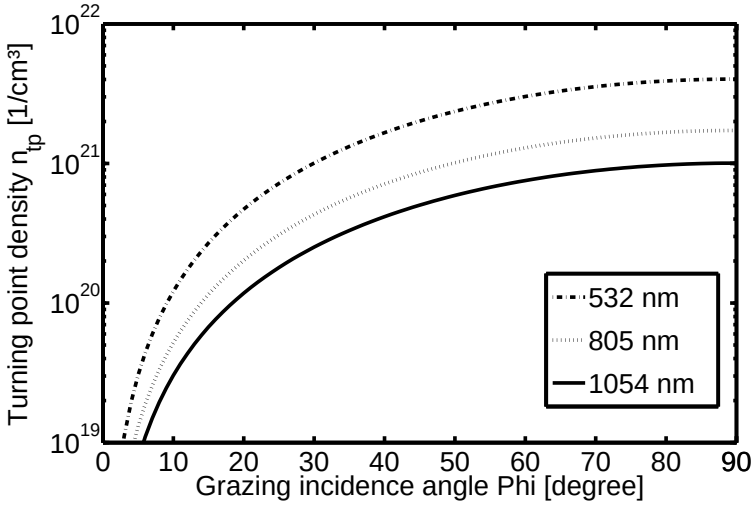

Figure 1.12: The turning point density n_{tp} is shown for Nd:glass pump lasers at 1054 nm and frequency doubled at 532 nm and for Ti:Sa lasers at 805 nm at different grazing incidence angles Φ.

1.2.12 Double-pulse single-beam grazing incidence pumping (DGRIP)

In contrast to the usual scheme of GRIP SXRLs, where a nanosecond long pre-pulse was assumed to provide the optimal plasma preparation and a picosecond short main pulse performed the final heating and excitation process, two collinear pulses of equal short picosecond duration were applied. The two pulses could be readily produced in a set-up resembling a Mach-Zehnder interferometer in the front-end of the CPA pump laser. The set-up will be described in detail in chapter 2. The double-pulse was then focused with the same optics in a single beam under grazing incidence onto the target. The first experiment in the double *short*-pulse single-beam grazing incidence geometry was performed on Ni-like Pd (14.7 nm) at the laser facility PHELIX (BZEK09b). Due to the collinear double-pulse a much simpler and more reliable operation was possible, at comparable efficiencies to the GRIP scheme (ZZB$^+$08).

The development of this pumping geometry resulted in an adapted pumping technique, where a pre-pulse duration of several hundred picoseconds was realized in the same Mach-Zehnder set-up. The pumping scheme allowed for efficient operation below 20 nm in the grazing incidence geometry and with a large grazing incidence angle for the generation of strong sub 10 nm lasing. It was termed

Double-pulse single-beam grazing incidence pumping (DGRIP) (ZZP$^+$10).

The DGRIP was applied for table-top high-repetition-rate longer-wavelength operation at the laser facility LASERIX (PPJC07) and allowed for the first time the full control of all the pump laser parameters, including the pre-pulse duration control thanks to a modification of the Mach-Zehnder, optimally preparing the SXRL amplifier under grazing incidence. On one hand the single-beam geometry of collinear double-pulse propagation guaranteed the ideal overlap of the pre- and main pulse from shot to shot, resulting in an efficient, highly stable SXRL output. On the other hand the grazing incidence of the long pre-pulse and the short main pulse introduced an operation closer to the target in a denser plasma region and thereby an enhancement of the gain in the amplifying zone, compared to the standard GRIP scheme and the short-pulse DGRIP scheme. In this way SXRL energies up to 2 μJ were obtained at 18.9 nm with a total pump energy less than 1 J for several hours at 10 Hz repetition rate without re-alignment under once optimized double pumping pulse parameters including energy ratio, time delay, pre- and main pulse duration and line focus width. The experimental results of DGRIP will be described and a performance comparison with previous schemes will be given in chapter 3.

To achieve shorter wavelengths in the transient collisional scheme, one has to work with higher Z materials in the Ni-like ion-state, which requires higher pump laser energies and a different pumping geometry. The concept of separating the ionization and the excitation is still valid, but the matching of the pumping density in the plasma has to be adapted for optimal gain generation. Issues to overcome were the adverse scaling of the ionization with the temperature for high atomic number ions, the strong thermal conduction at these temperatures and the fact that the optimal electron density equalled or exceeded the critical density for the 1 μm wavelength of solid state lasers. Therefore large grazing incidence angles were applied to bring the pump pulse to the optimal density, with respect to the turning point density.

In this way the DGRIP was applied for shorter wavelength soft x-ray laser generation at the laser facility PHELIX. The set-up included a single optic focusing geometry for large beam diameters, allowing for high energy laser double-pulses with energies up to 150 J and a compressor tuning capability to apply the traveling-wave pumping. A large grazing incidence angle of 73 degree was used to provide a deeper penetration of the pump laser light, beneficial for short wavelength operation. The first demonstration of a 7.36 nm Ni-like Sm SXRL pumped by only 36 J proved the

scheme's suitability for the operation at below 10 nm (ZRG$^+$10). The experimental results obtained at short wavelengths will be described in the first part of chapter 4. Due to the introduction of the new pumping scheme described here, the highly stable and efficient table-top high-repetition rate DGRIP soft x-ray laser became highly attractive to applications. The first application of the DGRIP SXRL at the laser facility LASERIX was the long-time operation in an irradiation experiment of user supplied samples. The capability to deliver reliably high photon doses at 18.9 nm with 10 Hz repetition rate was an achievement of the DGRIP scheme and enabled the stable operation running automatically over exposure times of several hours (ZZH$^+$10). The details of the DGRIP SXRL operation for application experiments will be presented in the second part of chapter 4.

Chapter 2

Mach-Zehnder Double-Pulse Development for Chirped Pulse Amplification Lasers

The development of a Mach-Zehnder (MZ) unit for the generation of double-pulses in a chirped pulse amplification (CPA) laser system is of central relevance for the present thesis. As explained in the introductive chapter the capability of creating two fully controllable pulses allows for the efficient pumping of soft x-ray lasers in the DGRIP scheme. The developed Mach-Zehnder unit produces two pulses with a variable energy balance, time delay and pulse duration in the front-end of the CPA laser system. The chirped oscillator pulse is distributed into two arms with an adjustable energy ratio via the combination of a wave plate and a polarizing beam splitter. Optionally, in one of the arms a variable grating compressor or grating stretcher is installed, adding an extra negative or positive chirp to the pulse. This allows to adjust independently the final pre-pulse duration, while the relative timing of the pulses is defined by an adjustable delay line in the other arm. After polarization matching and recombination, the double-pulse is amplified in the chain of the CPA laser system and compressed to its final temporal shape. In this way, two versions of a Mach-Zehnder were installed at the laser facilities PHELIX and LASERIX, each adapted to the specific requirements of each system. The characteristics of the Mach-Zehnder units and the details on the set-ups are described in this chapter, next to an introduction of the stated laser facilities. Moreover, investigations on the temporal and spectral shape of overlapping chirped double-

pulses are presented, together with a discussion about the influence of nonlinear effects. As an application of this constellation, the B-integral in the CPA laser system is measured by amplifying short pulse replica and analyzing their temporal behavior.

2.1 Chirped pulse amplification (CPA)

The laser systems PHELIX and LASERIX, which are utilized to pump the SXRLs in this thesis, are based on the technique of chirped pulse amplification (CPA) (SM85), which is commonly used in the field of high intensity lasers. CPA avoids nonlinear effects, such as self-focusing and self-phase-modulation leading to a degradation of the temporal and spatial pulse profiles, during propagation. The self-phase modulation is measured in terms of the B-integral giving the nonlinear phase Φ_{nl} accumulated during the propagation of the pulse through a medium at any position across the beam (PDS94):

$$\Phi_{nl} = \frac{2\pi}{\lambda} \int n_2 I(l) dl, \tag{2.1}$$

where λ is the wavelength, n_2 the nonlinear refractive index and I the intensity along the ray path l. To get a reasonable pulse profile at the output, the B-integral should not exceed 1. For most of the glass materials the nonlinear refractive index is $n_2 \sim 3 \times 10^{-16}\, cm^2/W$. Considering a pulse with a duration of 1 ps and a fluence of $0.5\, J/cm^2$ traveling through 1 cm of glass, this results already in a B-integral of 1.5. Since a large fluence is desirable to achieve high pulse energies, long pulses are necessary to avoid nonlinear effects during the amplification.
The principle of the CPA technique (Fig. 2.1) is to stretch the short pulse temporally by a factor of $\sim 10^3$ before amplification to reduce the pulse peak power. This is done by propagating the short laser pulse into highly-dispersive elements, to exploit the broad bandwidth associated with short pulses. A short pulse with the duration τ_p has a spectral width $\Delta\nu$ which follows from the Heisenberg uncertainty principle:

$$\tau_p \Delta\nu \leq K, \tag{2.2}$$

where K is a constant given by the pulse shape: for a Gaussian pulse is $K = 0.44$, for a $sech^2$ pulse is $K = 0.315$. When τ_p is short enough, $\Delta\nu$ becomes large enough to be sensitive to dispersion, resulting in group delay dispersion (GDD). Once the

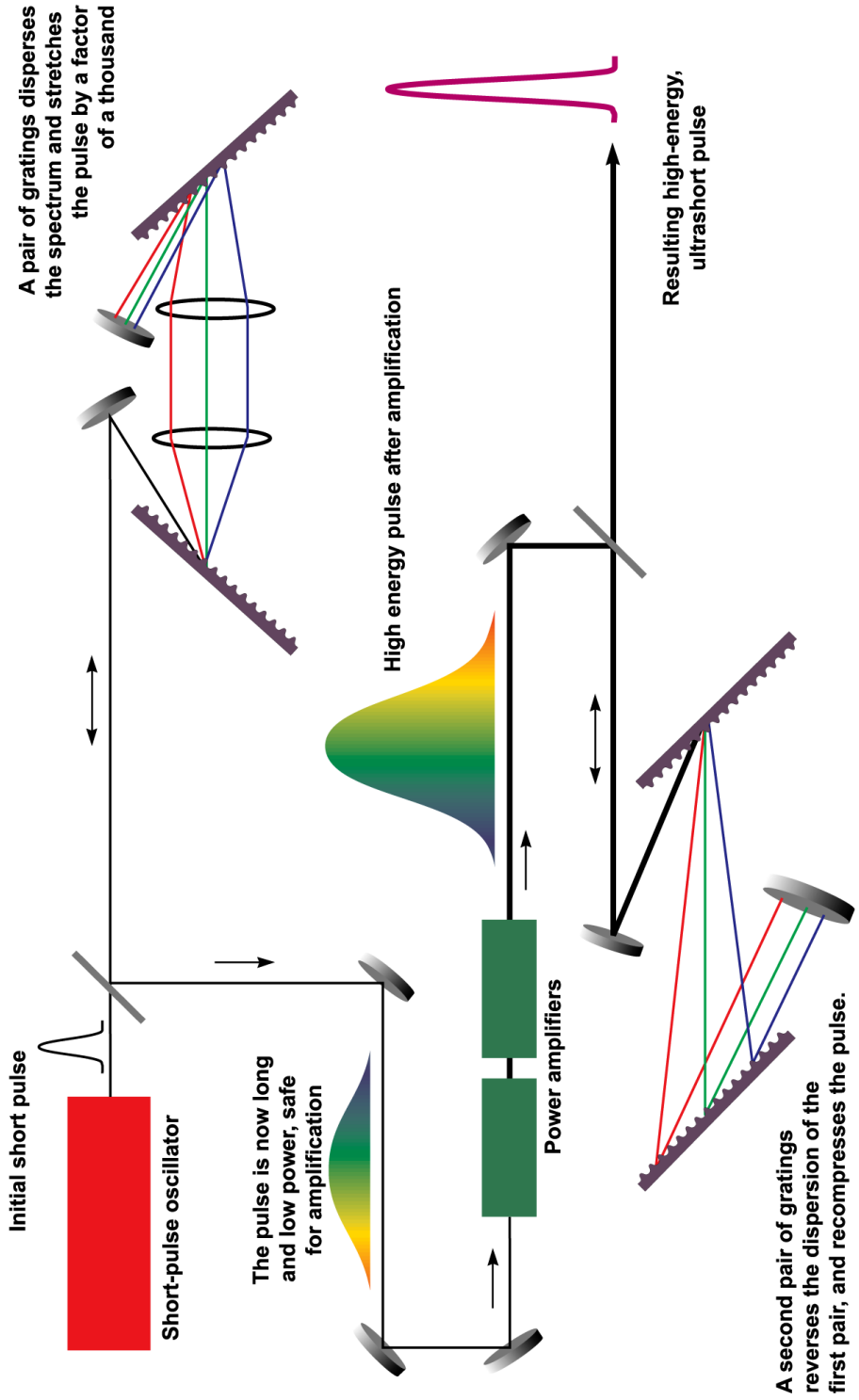

Figure 2.1: Principle of the Chirped Pulse Amplification (CPA) (Per95).

pulse is stretched (typically by introducing positive dispersion), it can be amplified to high energies and then it is compressed by applying opposite sign dispersion (typically negative). Pulse compression is not always fully successful, because it is limited by spectral gain narrowing on one side and GDD mismatch on the other side. For stretching and compression, pairs of dispersive elements like diffraction gratings, mainly for larger beams, or prisms are used, where the stretcher has its GDD sign opposite to the compressor. The most straightforward set-up to achieve the stretching or the compression is by a pair of parallel gratings. Here, the first grating produces the angular dispersion, where the spectral components with an incidence angle α will have diffraction angles $\beta(\lambda)$ following the grating equation:

$$\sin\beta(\lambda) + \sin\alpha = \frac{m\lambda}{g}, \tag{2.3}$$

where m is the diffraction order and g the grating groove spacing. The incidence angles of the different spectral components on the second grating equal their diffractions angles from the first grating so that the second grating re-collimates the different wavelengths of the pulse. At the output, the individual spectral components will have different optical paths lengths and the pulse will be stretched or compressed in time (frequency chirped).

2.2 PHELIX laser system

At the GSI Helmholtz Centre for Heavy Ion Research, the laser system PHELIX (Petawatt High Energy Laser for heavy Ion eXperiments) is in operation in stand-alone mode as well as in combination with ions accelerated by the heavy ion accelerator UNILAC (UNIversal Linear ACcelerator).
The overview of PHELIX presented in Fig. 2.2 shows the schematic arrangement of the laser building and its neighboring experimental area (Z6) in the Experimental Hall of GSI. The femtosecond front-end is used to generate the short sub-picosecond pulses. It consists of a commercial femtosecond laser oscillator (Coherent Mira) delivering pulses with a duration of 100 fs and energies around 4 nJ at a repetition rate of 76 MHz. The pulse is temporally stretched to 2.3 ns FWHM in a pulse stretcher with a distance of 4 m yielding a stretching factor of 190 ps/nm, whose architecture is a modified version of the stretcher architecture found in (PPS$^+$99). The pulse spectrum is limited to 12 nm because of the finite size of the optical grating

stretcher. The optical assembly of the stretcher is located on a translation stage which allows for easy adjustment of the pulse duration up to 20 ps after compression using the motorized stage and pre-set positions. This offers many advantages over the standard technique (adjusting the compressor grating-to-grating distance), which quickly becomes unpractical with grating assemblies that weigh up to 100 kg. The pulses are then amplified by two titanium-doped sapphire (Ti:Sa) regenerative amplifiers with a repetition rate of 10 Hz. The first one is set up in a linear configuration while the second one is a ring amplifier. The typical output energy after the ring regenerative amplifier is 30 mJ. Using ultra fast Pockels cells the achievable intensity contrast ratio is better than 60 dB.

Depending on the application, the pulses generated by the short-pulse front-end are compressed to $\sim$ 300 fs or further amplified in the next amplification stage. This pre-amplifier consists of three flash-lamp-pumped Nd:glass amplifiers (2 x 19 mm diameter, and 1 x 45 mm). The input beam delivered by the front-end is stepwise magnified by Keppler telescopes up to a maximum exit beam diameter of 70 mm in order to keep the fluence within safe limits, below the damage threshold. Furthermore, a deformable mirror (Night N Ltd.), located at the end of the amplifier, can correct wave-front aberrations. This mirror is actively driven in a closed-loop system, which utilizes a Shack-Hartmann sensor as a wave-front measurement device. After the pre-amplifier, the laser pulses of up to 10 J can be sent either to the X-ray lab, or to the main amplifier.

The main amplifier is set up in a double-pass configuration using five flash-lamp-pumped Nd:glass NOVA and PHEBUS amplifiers. The double pass architecture is using a geometrical separation of the incoming and outgoing pulses in the spatial filter. With amplifier modules having an individual clear aperture of 31.5 cm, up to 28 cm diameter beams are amplified and transported through the system; the corresponding output energy available for the experiments exceeds 1 kJ. This energy is only limited by the laser damage threshold of the Faraday isolator protecting the laser against possible back reflections. At this point, the beam enters a switch-yard where it can travel through a periscope and a telescope that sends it to the Experiment Hall, at the end of the GSI UNILAC, where combined laser and ion experiments can be conducted.

For the laser-only experiments, the short pulse capability of PHELIX in the laser bay is applied after the pulses are compressed. The pulse compressor uses multi-

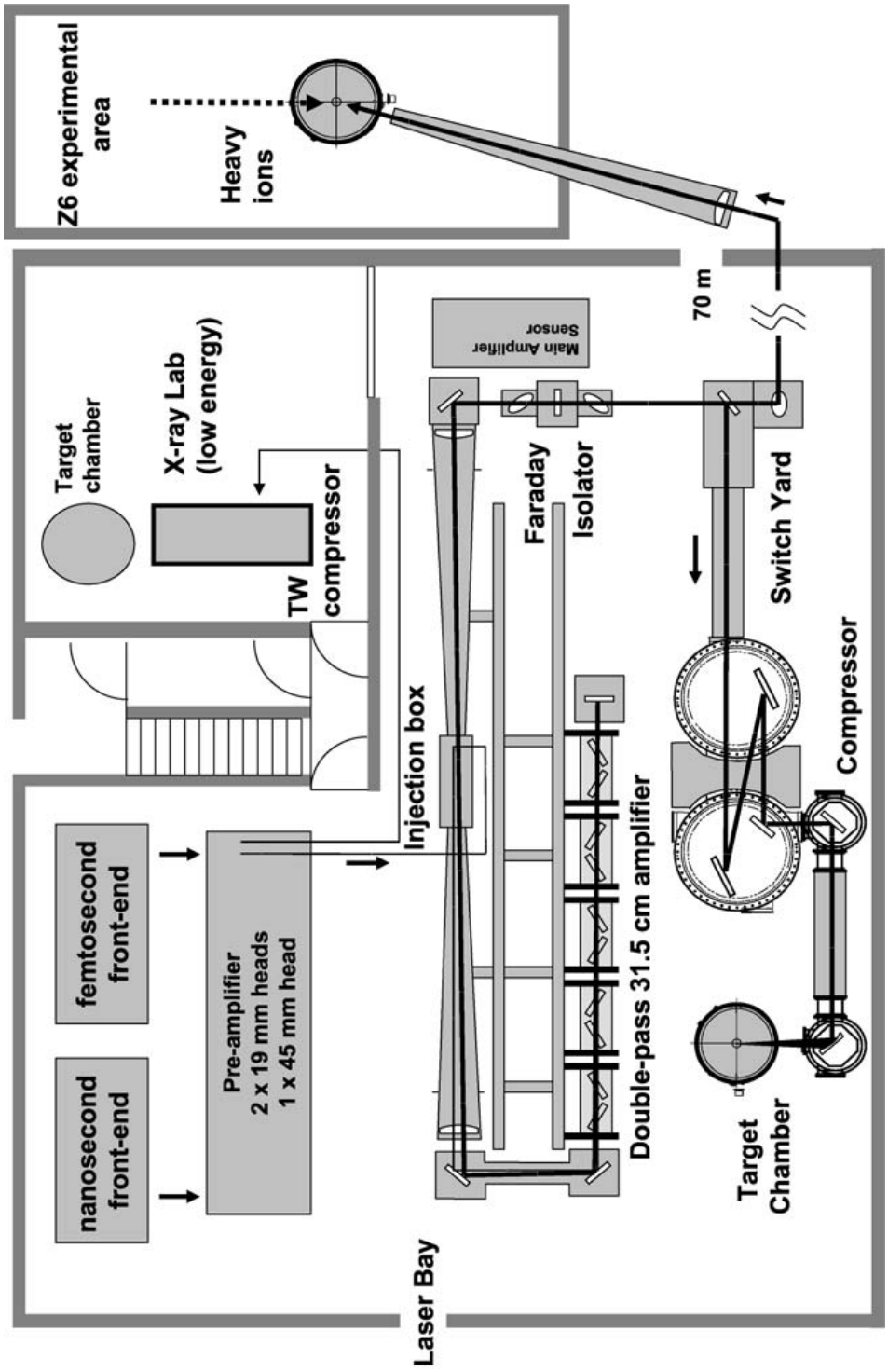

Figure 2.2: Schematic of the PHELIX laser system. The beam can be used at three different target stations: 1. X-ray lab, 2. Target chamber after the compressor, 3. Target station Z-6 at the heavy-ion accelerator beam-line (BAB+09).

Table 2.1: Present operational parameters of the PHELIX laser system. The temporal intensity contrast is given at 1 ns and 40 ps before the main pulse reaches its maximum for the long pulse and short pulse respectively.

	Long pulse	Short pulse
Pulse duration	$0.7 - 20\,ns$	$0.4 - 20\,ps$
Energy	$0.3 - 1\,kJ$	$120\,J$
Max intensity	$10^{16}\,W/cm^2$	$10^{20}\,W/cm^2$
Repetition rate at maximum power	1 shot every 90 min	1 shot every 90 min
Intensity contrast	50 dB	60 dB

layer dielectric (MLD) gratings (Horiba Jobin-Yvon, France) with 1740 lines/mm, which span 47 cm in the horizontal direction (dispersion) and 33 cm in the vertical direction. An incidence angle at the gratings of 72 degrees results in lower alignment and pointing sensitivity, at the expense of a largely increased size of the compressor tank. In this geometry, the incident beam profile is horizontally limited to 12 cm due to the size of the gratings. In the vertical direction the currently used beam extension is 24 cm so that the beam is elliptical. In order to achieve an optimal use of this area, the beam is shaped using lithographically produced serrated apertures, combined with spatial filtering. The serrated aperture in the beam line is located between the front-end and the pre-amplifier. The maximum output energy after the pulse compressor is limited by the damage threshold of the final grating. For 10 to 200 ps long pulses, the maximal throughput energy is 200 J. For the shortest pulses, below 1 ps duration, it is reduced to 150 J. This corresponds to a nominal peak power of 0.5 PW for 300 fs pulses. An overview of the laser parameters can be found in Table 2.1 which summarizes the laser output characteristics as a function of the type of operation.

2.3 LASERIX laser system

LASERIX is a high-power laser facility of the University Paris-Sud 11, embedded in the French "Institut de la Lumiére Extréme" (ILE) and the emanating European project Extreme Light Infrastructure (ELI), dedicated to high repetition rate soft

Table 2.2: The table presentes the different amplification stages of the Ti:Sa laser system LASERIX up to its full laser energy of 40 J.

Amplification stage	Dimension of Ti:Sa crystal	Pump energy	Laser beam diameter	Laser energy
1	10 mm × 10 mm	0.16 J	5 mm	25 mJ
2	16 mm × 16 mm	1.6 J	10 mm	0.5 J
3	30 mm × 30 mm	5 J	20 mm	2 J
4	100 mm^2	100 J	90 mm	40 J

x-ray lasers pumped by Ti:Sa laser drivers. The aim of the laser facility is to offer SXRLs in the 5-30 nm range and auxiliary IR beams that can also be used to produce additional synchronized SXR sources. This experimental versatility highly enhances the scientific opportunities of the facility to realize both SXRL and pump-probe experiments, mixing IR and SXRL sources.

The main technology of the LASERIX driver is based on Ti:Sa crystals. Indeed, due to their large line width, Ti: Sa lasers may emit much shorter pulses (in the range of few tens of fs) than Nd:glass lasers (more than 300 fs). The general architecture of the installed Ti:Sa laser is schematically presented in Fig. 2.3.

The front-end of the laser system delivers pulses energies of 2 J at a repetition-rate of 10 Hz, with a spectral bandwidth of 30 nm enabling less than 40 fs pulses after compression. The oscillator (Femtolasers) pulse is chirped to $\sim$ 500 ps by an Oeffner stretcher and amplified to 30 mJ by a 1 kHz regenerative amplifier followed by a 10 Hz four-pass pre-amplifier (Thales Laser). The power amplifier (Amplitude Technologies) consists of two cryogenically cooled 10 Hz multi-pass amplifiers which boost the energy to 2 J. The output can be seeded into another multi-pass booster amplifier to reach a pulse energy level of 40 J. This last amplifier is based on a 100 mm diameter, 20 mm thick highly doped Ti:Sa crystal (Crystal Systems) which is pumped by eight beams of 12.5 J (total of 100 J) of a frequency-doubled Nd:glass pump laser system (Quantel). After four successive passes through the crystal, the CPA pulse energy amounts to 40 J before compression with a repetition rate of 0.1 Hz. It is planned to perform the compression of half of the energy to reach a peak power in the range of 0.5 PW at the repetition rate of one shot every 10 s.

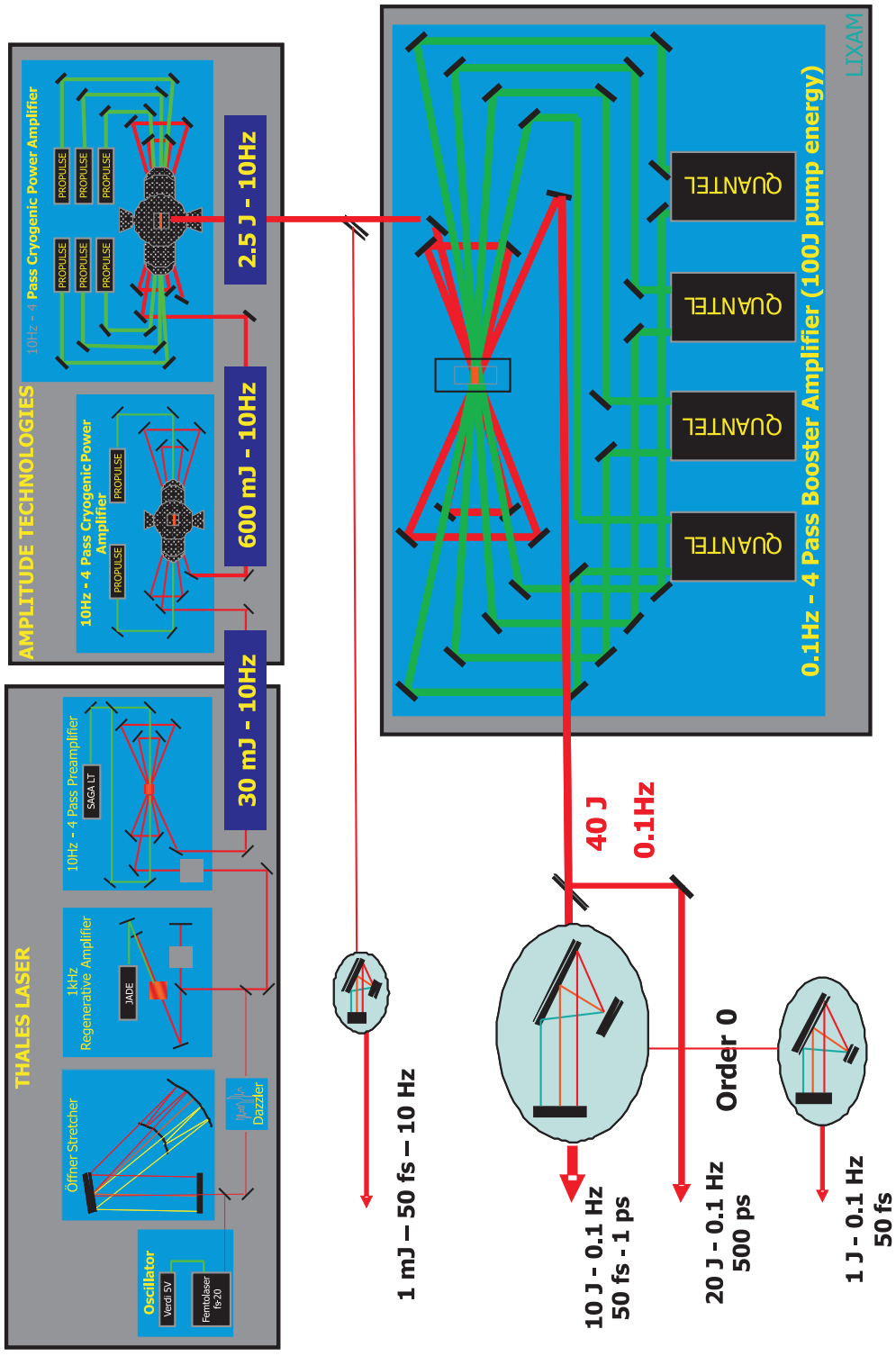

Figure 2.3: Schematic of the LASERIX laser driver (RGK+09).

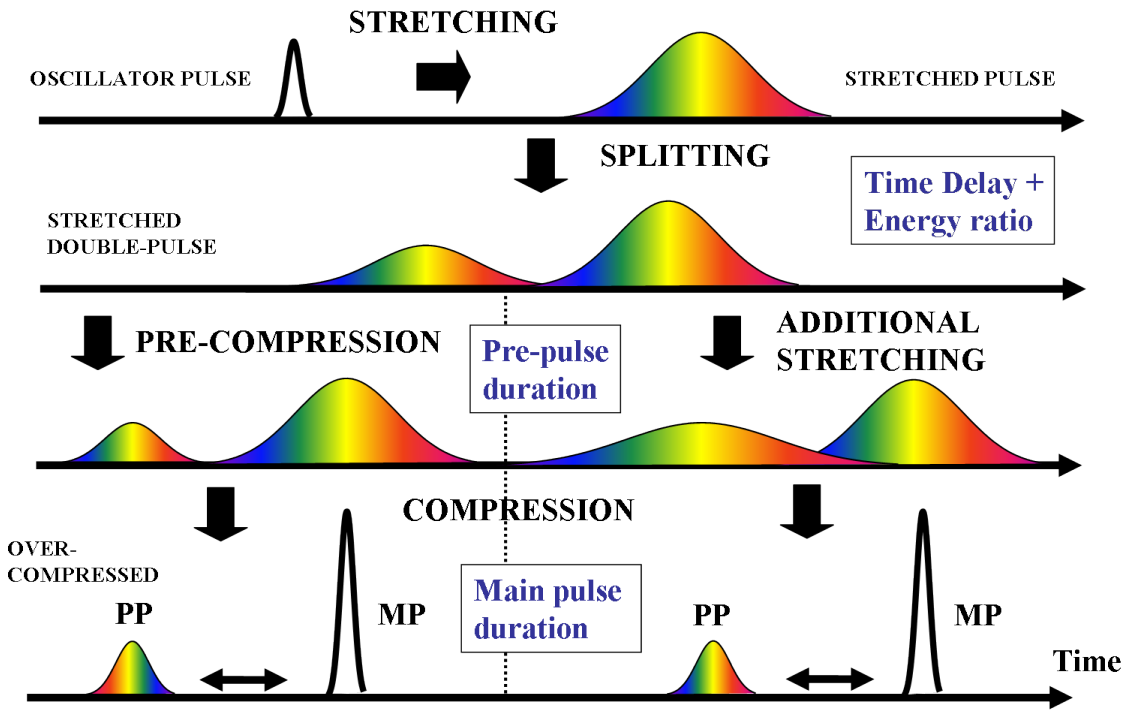

Figure 2.4: The principle of double-pulse generation in CPA lasers. The blue inserts indicate at which point the double-pulse parameters can be configured.

2.4 Mach-Zehnder double-pulse development for CPA lasers

The principle of double-pulse generation in chirped pulse amplification lasers is shown in Fig. 2.4. The oscillator pulse is stretched to a specific pulse duration, later determining the main pulse duration, and split in two pulses with a defined energy ratio and a controlled time delay. Then the first pulse is optionally either pre-compressed or additionally stretched, which determines the final pre-pulse duration. One has to remark that pre-compression and additional stretching - at constant settings of the final compressor - both result in an increase in the pulse duration after the final compression.

2.4.1 Mach-Zehnder set-up at PHELIX

The set-up of the Mach-Zehnder at the front-end of PHELIX is presented in Fig. 2.5 as a photograph and a technical CAD drawing. The installation of the

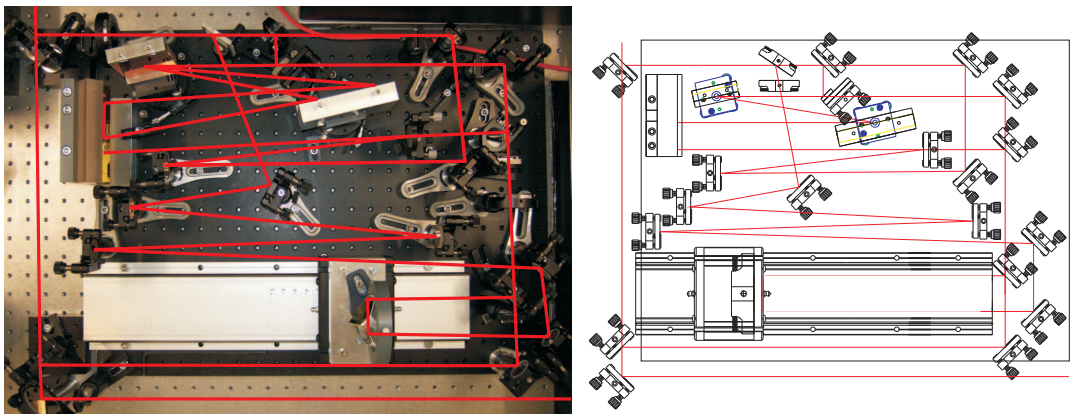

Figure 2.5: A photograph and the technical drawing of the Mach-Zehnder at the front-end of PHELIX together with the laser beam path indicated in red.

unit is placed on the optical front-end table to provide a maximum of stability. The Mach-Zehnder is located between the stretcher and the linear regenerative amplifier, and can be by-passed easily for single pulse operation. It operates in two modes, one for two short pulses, which were used for SXRL pumping, for measurements of the B-integral (in the end of this chapter), and for determination of the pulse front tilt (chapter 4). The second mode applies two differently stretched pulses for the DGRIP SXRL pumping at shorter wavelengths (chapter 4).

2.4.2 Mach-Zehnder set-up at LASERIX

A second Mach-Zehnder unit was installed at the front-end of LASERIX shown in Fig. 2.6 as a photograph and a technical CAD drawing. The unit is also placed on the optical front-end table between the stretcher and the first regenerative amplifier. The by-pass possibility is given as well, but only the differently chirped double-pulse mode is implemented at this laser system to perform the DGRIP SXRL pumping at longer wavelengths (chapter 3). One has to remark, that in this set-up a grating stretcher is used for the additional pre-pulse chirp, instead of a grating compressor as in the set-up at PHELIX. The reason for that lies in the maximal fluence, which can be applied in both laser systems. In the case of PHELIX the oscillator pulse is already sufficiently stretched to $\sim 1\,\mathrm{ns}$, that the additional shortening of 200 ps does not cause any problems. Contrariwise the stretched pulse duration of LASERIX counts only $\sim 500\,\mathrm{ps}$ and a reduction by 200 ps would cause fluence problems, so that an additional stretching has to be applied.

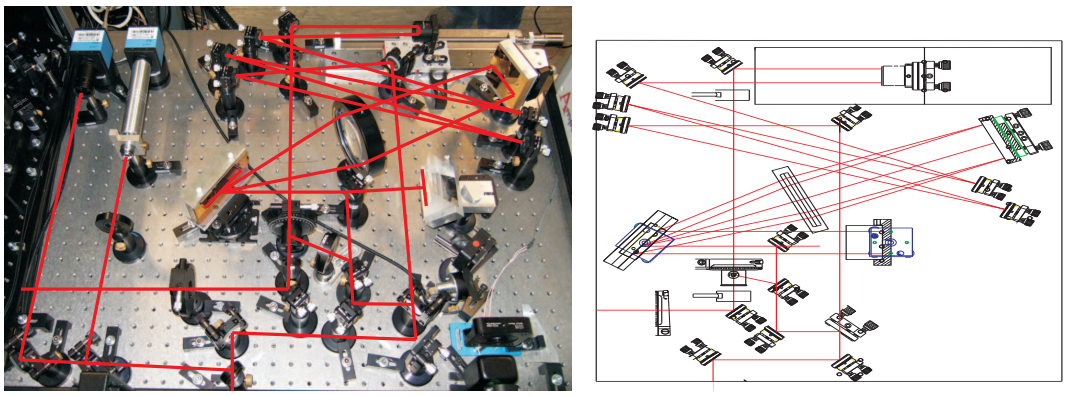

Figure 2.6: A photograph and the technical drawing of the Mach-Zehnder at the front-end of LASERIX together with the laser beam path indicated in red.

2.4.3 Mach-Zehnder grating compressor design

The applied grating compressor is a 2-pass double-grating compressor which follows the design developed by (Tre69). The advantage of this grating geometry is the absence of angular dispersion or spatial chirp. The compressor is designed for a 200 ps pre-pulse duration output, however, it can be adjusted to produce a longer or shorter pulse duration from 300-100 ps by moving the 2nd grating farther or closer to the 1st grating along the diffracted center wavelength. The calculations and simulations for this set-up are done with the Optica Package for Mathematica 5 assuming a 10 mm diameter beam with 12 nm bandwidth (Fig 2.7).
The set-up is optimized for a Group Dispersion Delay (GDD) of $\sim$ -34 ps/nm giving a pulse duration of $\sim$ 200 ps at the compressor output at 6 nm bandwidth. For different pulse durations or bandwidths the necessary GDD has to be changed. The new GDD can be calculated according to:

$$GDD_p\,[ps/nm] = t_p\,[ps]/\Delta\lambda_p\,[nm]. \tag{2.4}$$

The pulse duration of the pre-pulse coming out of the MZ compressor can then be calculated according to:

$$t_p\,[ps] = 190\,ps/nm \times \Delta\lambda_p\,[nm] - GDD_p\,[ps/nm] \times \Delta\lambda_p\,[nm], \tag{2.5}$$

where $\Delta\lambda_p$ is the bandwidth of the laser pulse after the complete amplification chain and 190 ps/nm the GDD of the PHELIX stretcher. To determine the geometrical design of the grating compressor one has to choose a suitable incidence angle α,

Table 2.3: The characteristics of the Mach-Zehnder grating compressor at PHELIX.

Grating constant $N = 1/g$	1800 lines/mm
Incidence angle α	77 degree
Diffraction angle β_0	67.3 degree
Length L	444 mm
Grating distance parameter D_s	222 mm
GDD	-34 ps/nm
Output pulse duration	200 ps at 6 nm
Central wavelength λ_0	1054 nm
Bandwidth transmission	12 nm
Available pulse duration range	100 - 300 ps at 6 nm
Reached with a grating shift of	-111 to +105 mm at 6 nm

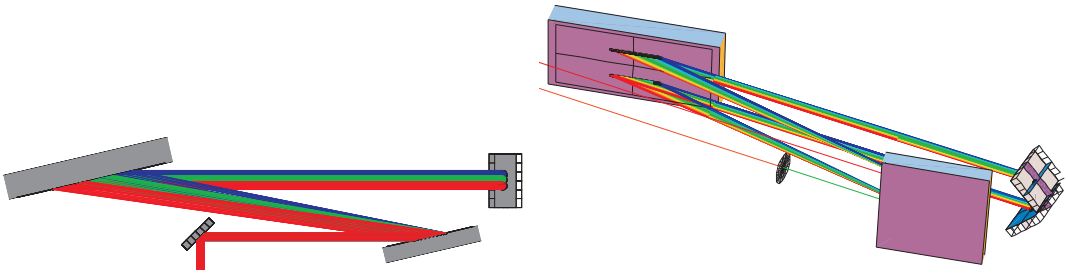

Figure 2.7: A simulation of the grating compressor with Optica.

which results in a diffraction angle of

$$\beta_0 = \arcsin[N\lambda_0 - \sin(\alpha)] \tag{2.6}$$

and in a grating distance parameter of

$$D_s = L/N_s = -\frac{2\pi c^2 cos^2(\beta_0)}{N^2\lambda_0^3}\Phi_2 \tag{2.7}$$

with the phase of a single pass Φ_2 and N_s the number of passes. The specifications of the final grating stretcher can be found in Table 2.3.

Mach-Zehnder grating compressor chirp characterization

The determination of the grating compressor GDD is done by the analysis of the temporal pulse shapes. For this, the unstretched oscillator pulse is injected into the

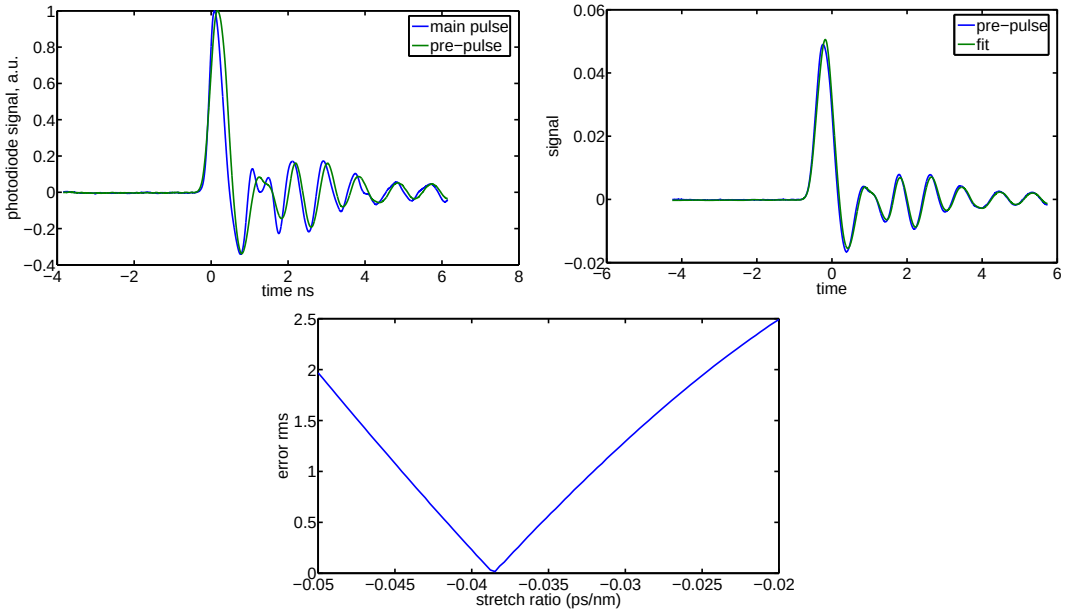

Figure 2.8: The figure on the left-hand side shows the recorded photo diode signal for the "stretched" and original oscillator pulse. The figure on the right-hand side presents the fit to the "stretched" pulse with a convolution of the chirp and the response of the photo diode, which yields a stretch ratio of 38.5 ps/nm shown in the bottom figure.

MZ creating two pulses. One of the pulses is passed through the grating compressor, resulting in an effective stretching by the compressor's GDD. Each of the two pulses is now recorded by a fast photo diode and a 2.5 GHz oscilloscope. The non-chirped pulse gives the impulse response of the scope, while the stretched pulse gives a longer signal. Assuming a Gaussian temporal pulse profile, the correlation of the each pulse with the impulse response of the scope times the one of the diode gives the expected signals. Both signals are normalized to 1 and the RMS of the difference is plotted for different pulse durations. The fit of the smallest RMS error yields the best pulse shape. With the recorded spectrum of the stretched pulse, we look for the best scaling (in ps/nm) for matching the spectrum to the pulse. Again, several stretch ratios are assumed and the error (difference of the two signals normalized to their first moment) is plotted. The stretch ratio fitting best, equals 38.5 ps/nm, which is within 10% of the compressor design value of 34 ps/nm.

Mach-Zehnder performance

Once the pulses are stretched, they overlap in time due to their strong chirp, and a direct temporal measurement is not possible. For the precise determination of the pulse duration of the pre-pulse t_p, the width of the spectrum $\Delta\lambda_p$ has to be recorded and convoluted with its group delay dispersion GDD_p, following Eq. 2.4, while the main pulse duration in the picosecond range is analyzed after compression with a single shot auto-correlator. To get precise timing on the delay of the double-pulse, we used the interference occurring in the spectrum for the differently chirped pulses (Fig. 2.14). An interference peak shows up at the spectral position λ_p depending on the time delay of the pulses t_d and the group delay dispersion difference of the pulses GDD_{diff}, following $t_d\,[ps] = \lambda_p\,[nm] \times GDD_{diff}\,[ps/nm]$. In this way a determination of the time delay is possible with a resolution better than 1 ps.

2.4.4 Mach-Zehnder grating stretcher design

The applied stretcher is a 2-pass single-grating stretcher, with a single-lens plane-mirror telescope following the design of (Mar87). The stretcher is optimized for 200 ps pre-pulse duration output, however, it can be adjusted to produce a shorter pulse duration down to 100 ps by moving the lens and plane mirror closer to the grating along the diffracted center wavelength. The set-up of the stretcher is optimized for a GDD of $\sim +6$ ps/nm giving at the compressor output a pulse duration of ~ 200 ps at 33 nm bandwidth. For different pulse durations or bandwidths the necessary GDD has to be changed, according to Eq. 2.4. The pulse duration of the pre-pulse at the MZ stretcher output can be calculated by:

$$t_p\,[ps] = 15\,ps/nm \times \Delta\lambda_p\,[nm] - GDD_p\,[ps/nm] \times \Delta\lambda_p\,[nm], \qquad (2.8)$$

where $\Delta\lambda_p$ is the bandwidth of the laser pulse and 15 ps/nm the GDD of the LASERIX stretcher. Analog to the compressor design, the geometry of the stretcher (Fig. 2.9) depends on the incidence angle α, and the resulting diffraction angle β_0. The final specifications of the grating stretcher can be found in Table 2.4.

Mach-Zehnder grating stretcher chirp characterization

Another method to determine the introduced chirp is the analysis of the position of the interference peak occurring in the spectrum for different time delays. The

Table 2.4: The characteristics of the Mach-Zehnder grating stretcher at LASERIX.

Grating constant $N = 1/g$	1800 l/mm
Incidence angle α	36 degree
Diffraction angle β_0	59.45 degree
Length L	178 mm
Grating distance parameter D_s	89 mm
Lens type	bi-convex
Focal length f	254 mm
GDD	+6 ps/nm
Output pulse duration	210 ps at 33 nm
Central wavelength λ_0	805 nm
Bandwidth transmission	70 nm
Available pulse duration range	100 - 200 ps at 33 nm
Reached with a lens/plane mirror shift of	-44.5 mm at 33 nm

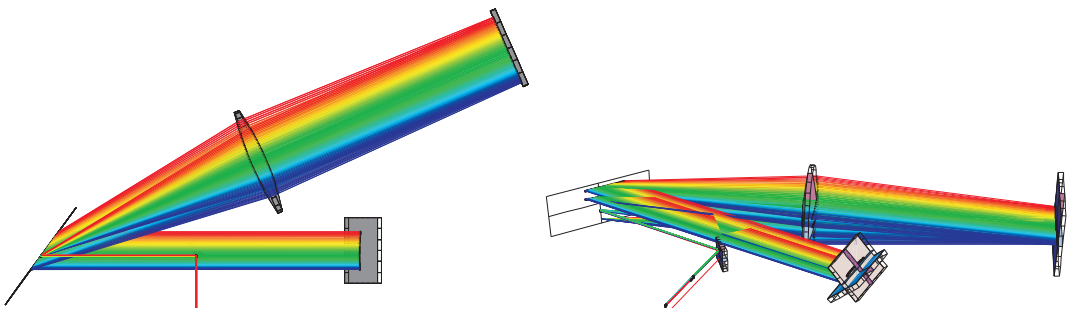

Figure 2.9: A simulation of the grating stretcher with Optica.

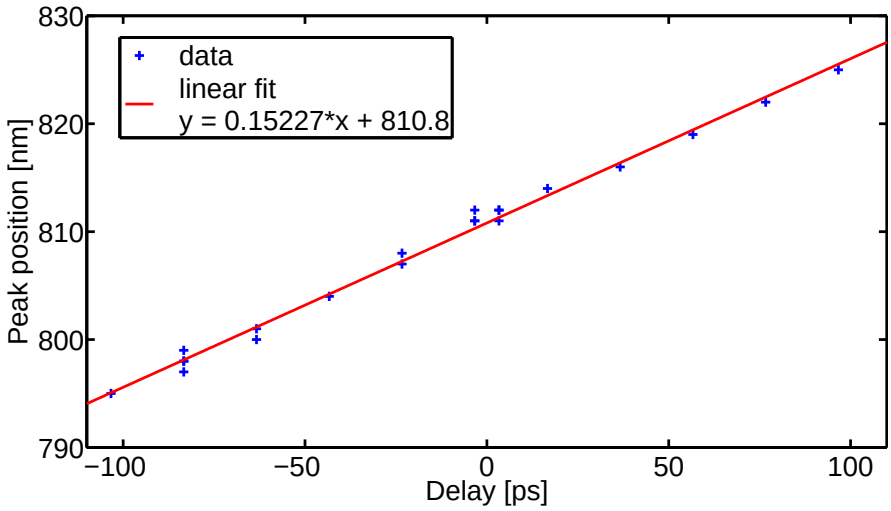

Figure 2.10: The spectral interference peak positions for different time delays and the fit of the gradient yields a group dispersion delay of 6.57 ps/nm.

variation of the double-pulse delay shifts the peak along the spectrum exactly with the difference of chirp between the two pulses. A plot of the peak position in the spectrum in dependence of the time delay is shown in Fig. 2.10. A linear fit of the gradient yields a GDD of 6.57 ps/nm for the installed grating stretcher. This value fits within 10% to the design value of 6 ps/nm. After the calibration of the GDD of the stretcher, the absolute spectral peak position is used to precisely determine the time delay of the double-pulse, as explained in the previous section.

Mach-Zehnder performance

The spectrum, the temporal shape and the energy ratio are analyzed after each unit in the laser system. The spectra are plotted in Fig. 2.11 for the pre-pulse arm, the man pulse arm and the combined double-pulse before and after amplification. The spectral shapes have to be controlled, since the stretcher unit is a dispersive element and one has exclude spectral clipping before combining the two pulses. The dip in the spectra is induced by an acousto-optical modulator to pre-compensate for gain narrowing of the amplifier section. The spectrum of the double-pulse operation shows the typical shape as observed in the single-pulse, means standard operation. The determination of the pulse energy ratio of the double-pulse is done by a measurement with a photo diode. In Fig. 2.12 the temporal pulse shape is shown for a typical double-pulse structure with a dip in each pulse. In this case the delay is

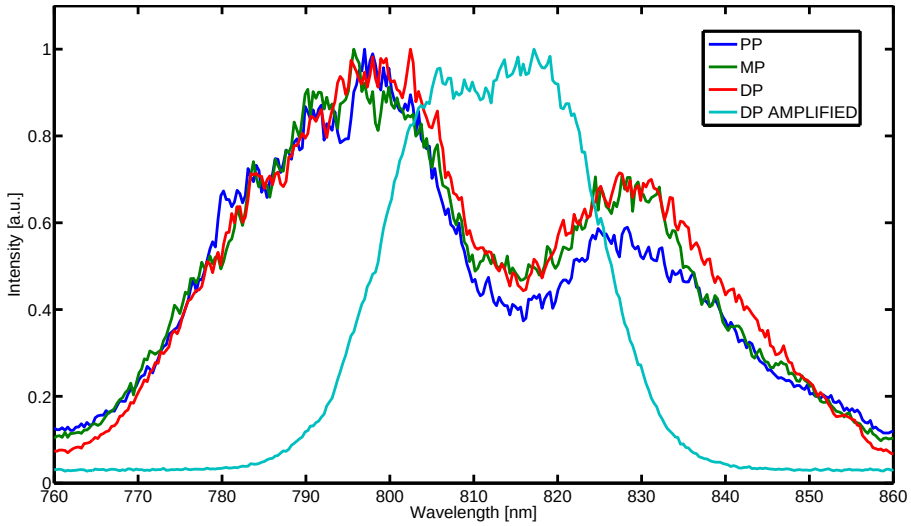

Figure 2.11: The spectrum of the acousto-optically modulated chirped oscillator pulse is presented for the pre-pulse, the main pulse, the combined double-pulse and the amplified double-pulse at the end of the CPA laser chain.

set to 1.3 ns to clearly separate the two pulses for the measurement. In Fig. 2.13 the double-pulse structure is shown for the different sections of the laser system: at the regenerative amplifier, the pre-amplifier, the amplifier 1 and the amplifier 2 in which the dip disappeared due to the amplification profile of the laser. One can notice the nearly constant ($\pm 5\%$) pulse energy ratio of the double-pulses all along the laser chain, allowing for the precise control of the pulse energy ratio already at the Mach-Zehnder set-up.

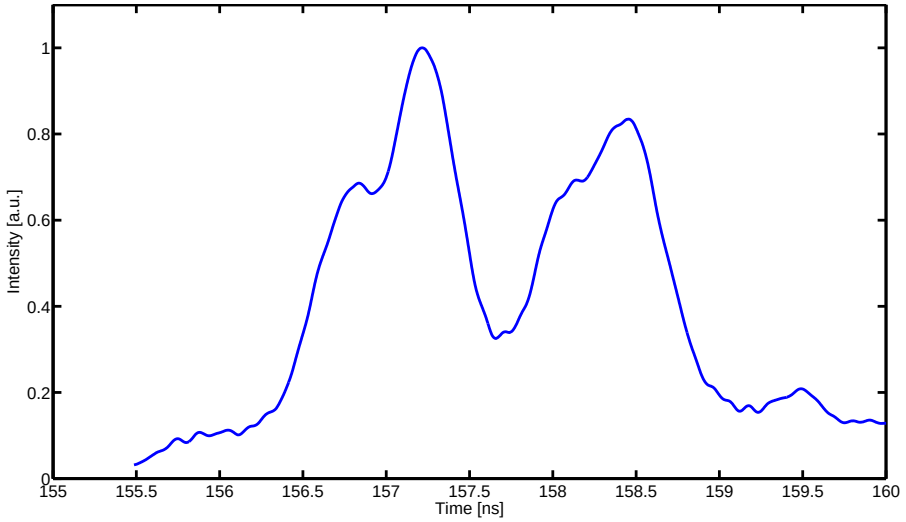

Figure 2.12: The temporal shape of the double-pulse at the Mach-Zehnder exit is plotted for a time delay of 1.3 ns with a dip in each pulse, introduced by the acousto-optical modulator.

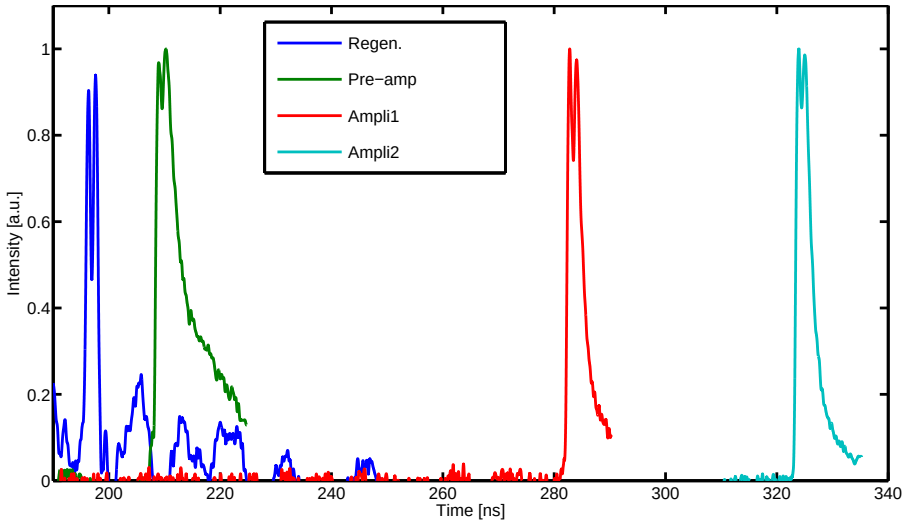

Figure 2.13: The temporal shape of the double-pulse is shown at different positions in the CPA laser chain, preserving the double-pulse energy balance.

2.5 Influence of B-integral on CPA double-pulses

The influence of nonlinear effects in CPA laser systems is well known, but the speciality of double-pulses introduces some interesting effects which are discussed in this section. The temporal overlap of two chirped pulses results in an interference which influences the temporal and spectral characteristics of the pulses, especially when nonlinear effects are involved. For this purpose spectral and temporal measurements are compared with simulations to provide information on the final temporal shape of double-pulses after compression, at the end of the CPA laser chain. For the application of SXRL pumping, possible problematic effects caused by the influence of the B-integral on CPA double-pulses could be excluded, and a safe operation in the CPA chain was demonstrated. The observed effects for equally chirped pulses were used as an application to determine of the total amount of accumulated B-integral in the CPA system.

2.5.1 Spectral and temporal analysis

A simple model has been developed to describe the pulse-replica together with a space-to-time analogy to show that diffraction theory results obtained in the Fraunhofer approximation can be extended here and justify the time-diffraction qualification.

The analogy between spatial and temporal diffraction can be analyzed by the pulse stretching effect. A short pulse of duration δt which is sent through a temporal pulse-stretcher, is described in the spectral domain as the addition of a quadratic phase term to the pulse spectrum, where E_{st} is the complex field of the stretched pulse, E_0 the field of the initial pulse and Φ_2 the second derivative of the phase introduced in the stretcher, taken at ω_0.

$$E_{st}(\omega) = E_0(\omega) exp[i\Phi_2 \frac{(\omega - \omega_0)^2}{2}] \tag{2.9}$$

In this case, the spectral phase applied by the stretcher is simplified, so constant and linear terms together with higher order terms are neglected. In the time domain, the temporal stretching of the pulse corresponds to the following convolution:

$$E_{st}(t') = \int E(t) exp[i\frac{1}{\Phi_2}(t' - t)^2] dt \tag{2.10}$$

$$\frac{\delta t^2}{\Phi_2} << 1 \tag{2.11}$$

An important simplification can be made if the condition 2.11 is fulfilled, which means that the stretched pulse is much longer than the original pulse, which is valid in most CPA systems, as large stretching factors are applied. Using condition 2.11 in Eq. 2.10 yields Eq. 2.12, which describes the electric field of the stretched pulse using the Fourier transform of the initial field. The temporal profile of the stretched pulse is directly related to its spectrum, using the scaling factor Φ_2. This is called frequency-to-time mapping or frequency chirping present in CPA laser systems.

$$E_{st}(t') = exp[i\frac{t'^2}{\Phi_2}] \int E(t)exp[-2i\frac{1}{\Phi_2}t't]dt = exp[i\frac{t'^2}{\Phi_2}]FT(E(t))_{\omega=t/\Phi_2} \tag{2.12}$$

The interference of two short laser pulses with equal amplitude $E(t)/\sqrt{2}$ can be derived from a single pulse with amplitude $E(t)$, carrier pulsation ω and relative time delay τ. The electric field $E_{int}(\omega)$ can be written in the spectral domain as:

$$E_{int}(\omega) = FT(\frac{E(t)exp(i\omega_0 t)}{\sqrt{2}} + \frac{E(t)exp(i\omega_0 t)}{\sqrt{2}} * \delta_\tau) = [\frac{E(\omega)}{\sqrt{2}}(1 + exp(i\omega\tau)) * \delta_{\omega_0}, \tag{2.13}$$

where FT is the Fourier transform operator and the convolution with a Dirac function δ represents the offset in either time or frequency. The spectral intensity is then modulated at a frequency $\omega\tau$ (LCJ95) and, in the case of a pulse with a linear chirp, the modulation is also present in time, because of the frequency-to-time mapping. The set-up in Fig. 2.17 shows the experimental configuration, where a short pulse is replicated and stretched in time using a dispersive element as pulse stretcher. Using the space-to-time analogy, the intensity distribution in time after the stretcher will be equivalent to the far field distribution in a Youngs slit experiment, which is a time-modulated pulse. In the case of a fully linear system, the effect of the compressor will be to re-compress the two pulses independently of each other. But in the presence of Kerr effect, the modulated pulse structure can be written in the form:

$$E_{mod}(t) = exp[i\frac{t^2}{\Phi_2}]E_{int}(\omega)_{\omega=t/\Phi_2}exp[ib(1 + cos(\frac{t\tau}{\Phi_2}))], \tag{2.14}$$

where b is the nonlinear Kerr effect factor or B-integral one would get for the single stretched pulse. The effect on the compressed pulse structure is a periodic peak structure, with a period related to the modulation period. The amount of energy diffracted into these peaks strongly depends on the amplitude of the phase modulation, thus on the amount of Kerr effect in the amplifier. In comparison to the

method of (VBR07), where the nonlinear effect is analyzed in the intermediate field, using Fresnel numbers higher than one, our method is based on a far-field analysis, thus reducing the complexity of interpreting the data.
The simulations presented in this section for the temporal and spectral analysis are done with Matlab 7, a numerical computation software. Differently and equally chirped overlapping pulse configurations are simulated.

Differently chirped pulses

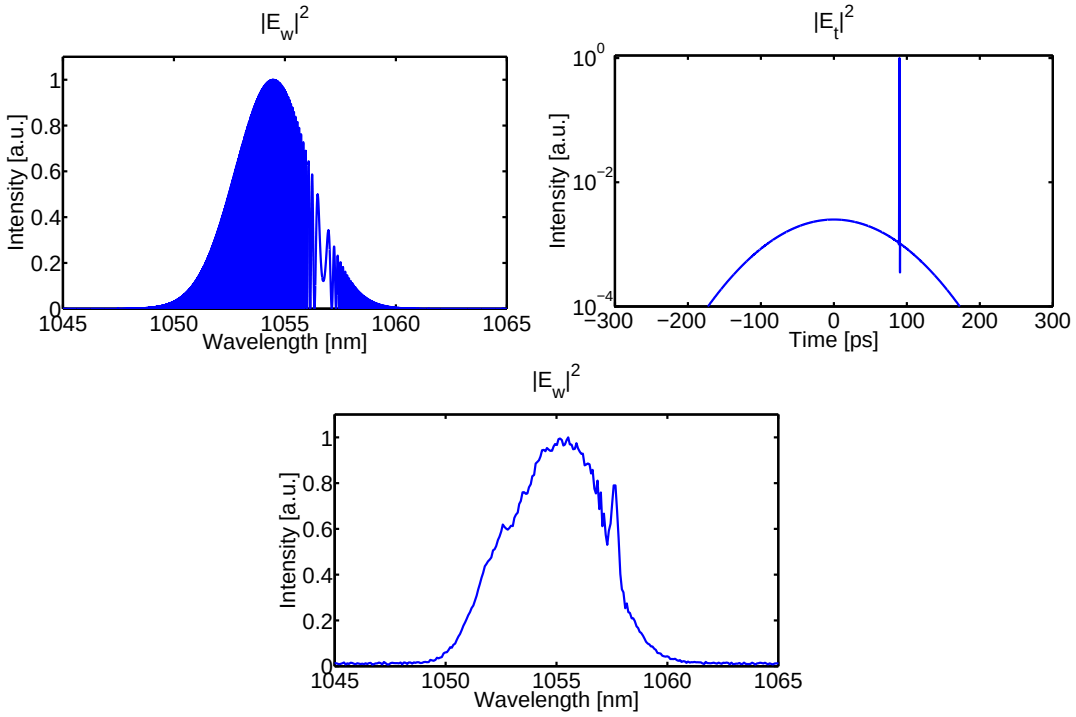

Figure 2.14: Simulations of the double-pulse spectrum and the temporal shape after compression for two differently chirped pulses together with the corresponding experimental spectrum.

For soft x-ray laser experiments it is necessary to simulate typically applied double-pulse pump parameters in the CPA laser to exclude uncertainties and to understand the occurring interference effects. The spectral and temporal domain of two differently chirped pulses (GDD of 160 ps/nm and 200 ps/nm) with a time delay of 90 ps and a bandwidth of 5 nm at the center wavelength of 1055.5 nm are presented, as typically used for short wavelength SXRL pumping (Fig. 2.14). The signal is fully modulated and shows a peak structure at 1057.75 nm which translates

into a double-pulse time delay of 90 ps for the chirp difference of 40 ps/nm. This result is confirmed by an experimental spectrum obtained at the $\sim$ 100 J level after the main amplifier at PHELIX, showing exactly the simulated feature. The simulated temporal shape of the double-pulse after the compression is shown as well, to reveal the temporal shape of the double-pulse, which cannot be measured experimentally. One sees that the experimental spectrum with 5 nm FWHM and a center wavelength of 1055.5 nm fulfils the double-pulse parameter requirements of a 200 ps pre-pulse and a 1 ps short pulse for SXRL pumping. In this way the temporal structure of the double-pulse is controlled during the SXRL experiment by monitoring the spectrum of the amplified CPA pulse.

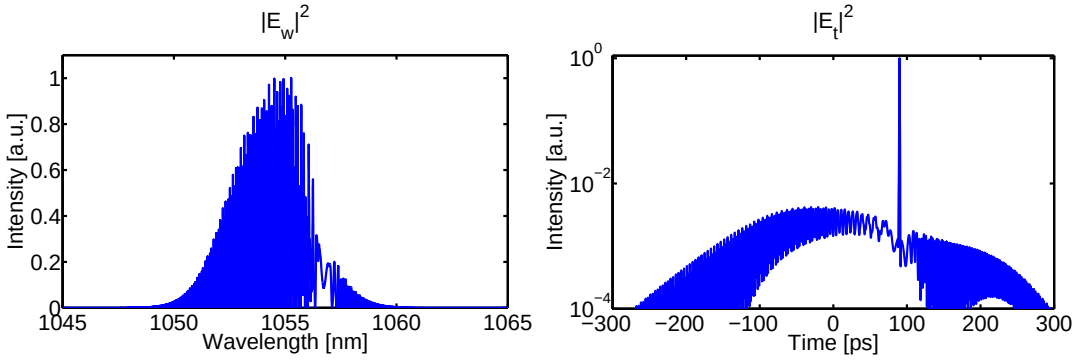

Figure 2.15: Simulations of the double-pulse spectrum and the temporal shape after compression for two differently chirped pulses with the consideration of nonlinear effects.

A simulation under consideration of non-linear effects occurring in the regenerative Ti:Sa amplifiers in the front-end of the PHELIX laser system is shown in Fig. 2.15. The introduction of a B-integral of 1, a value having been experimentally determined for the amplifier system (BZEK09b), changes the spectral shape of the double-pulse. The spectral and temporal shapes become strongly modulated, but the average value does not change and thereby the temporal shape is preserved, avoiding a reconfiguration of the original double-pulse configuration for SXRL pumping. The simulation shows as well that problematic effects do not occur, in terms of unexpected intensity spikes in the spectral and temporal domain. With this knowledge a safe operation of double-pulses in the CPA laser system could be ensured. With the demonstration of CPA double-pulses with high energies up to 150 J without any problematic effects at PHELIX, the requisite for the transfer of the double-pulse

pumping technique to CPA laser system LASERIX was fulfilled.

Equally chirped pulses

For the case of equally chirped pulses the simulations reveal several differences compared to the previous results. Especially the creation of replica in the temporal domain has to be considered here. In Fig. 2.16 the undisturbed case without nonlinear effects and the case with a present B-integral of 1 is shown. In the latter, equally distant peaks, like a picket fence, appear for originally two balanced pulses with a delay of 8 ps. The replica have a decreasing intensity, starting at 10% of the original pulse intensity. This effect is explained in more detail in the next section and leads to a benchmark for nonlinear effects.

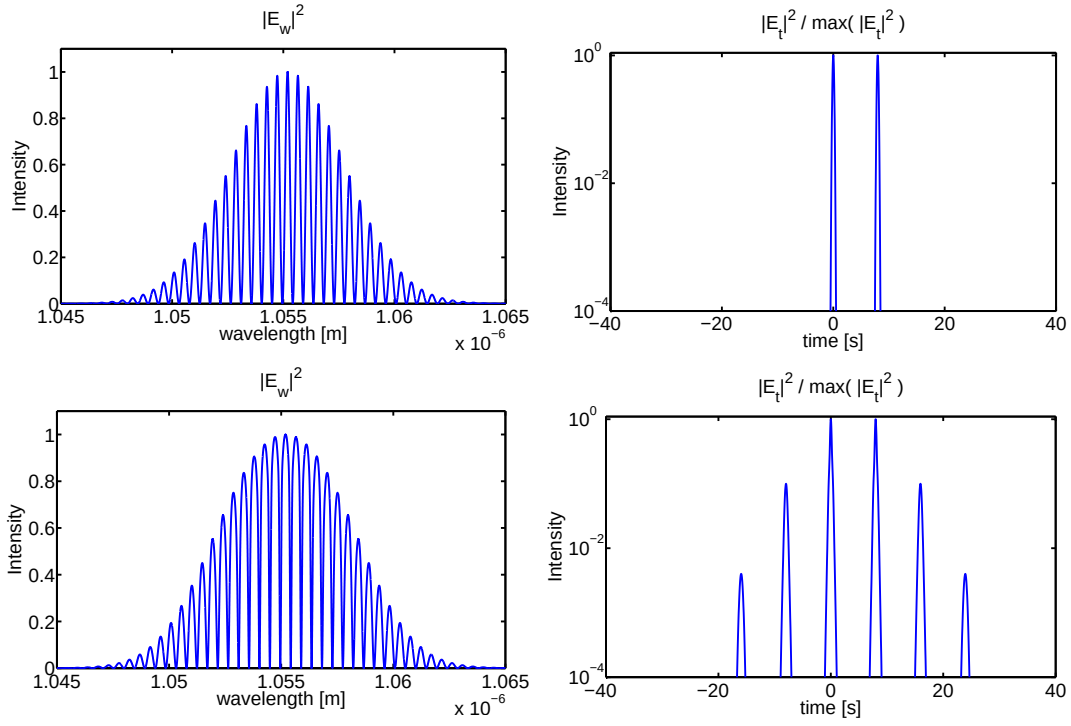

Figure 2.16: Simulations of the double-pulse spectrum and the temporal shape after compression for two equally chirped pulses. The figures show simulation data without and with nonlinear effects in the first and second row, respectively.

2.5.2 Measurement of B-integral in CPA lasers with double-pulses

A simple method for measuring the B-integral accumulated in chirped-pulse amplification laser systems based on temporal diffraction is presented in this section. Two identical pulses, which are sent into the amplifier create temporal replica, as shown in the previous section, are used to retrieve the amount of B-integral accumulation. The nonlinear Kerr effect accumulation can be estimated in a laser system via careful computation of the laser intensity in the presence of material exhibiting nonlinear index properties. However, this task is not easy as it requires complete knowledge of the material and laser parameters, not accounting for the fact that these can evolve in time. For this reason, a method for directly measuring the B-integral accumulated in CPA systems is highly desirable.

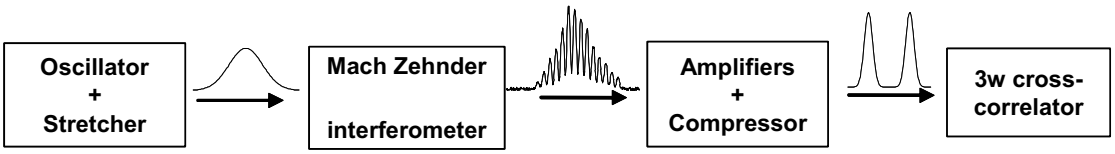

Figure 2.17: Experimental principle showing how a short pulse is stretched in time and replicated (BZEK10).

Experimental results

A measurement in the time domain is applied to determine the value of the accumulated B-integral. We used two laser pulses to be amplified and analyzed the temporal pulse structure after compression. In the presence of nonlinear Kerr effect satellite pulses are created on either side of the main pulses with a relative amplitude directly related to the amplitude of the nonlinear modulation, i.e. the amount of B-integral. Two experiments were carried out to measure the B-integral, one with a sub-picosecond laser system using the Mach-Zehnder at PHELIX and the other with a carrier-envelope-phase (CEP) controlled ultra-short pulse femtosecond-laser system at LOA Palaiseau, where an acousto-optical programmable dispersive filter or AOPDF (Dazzler TM) creates the double-pulse structure.
In the first experiment, pulses from the front-end of PHELIX are generated using the arrangement showed in Fig. 2.17. For this case the front-end was operating at centre

wavelength of 1053 nm with an energy of 20 mJ for both pulses at 10 Hz repetition rate. The +200 ps/nm stretched pulses were compressed to 300 fs and temporally analyzed by a commercial third-order cross-correlator (Sequoia, Amplitude Technologies). Because of the low cross-section of Ti:Sa at the wavelength of 1053 nm, the laser fluence is high in the amplifier and the amount of material crossed by the laser pulse large compared to regenerative amplification performed at 800 nm. The B-integral can be calculated by accumulation close to unity, using nonlinear-index values of Ti:Sa crystals and by estimating laser intensities in the amplifier.

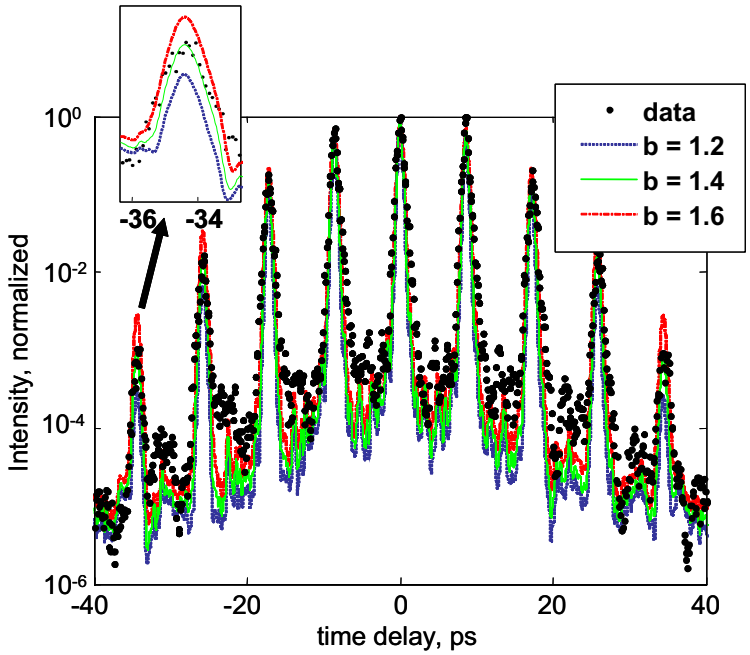

Figure 2.18: Experimental trace (dots) and fit (solid line) of the measurement, using a three different fit parameters b of 1.2, 1.4 and 1.6, respectively (BZEK10).

A typical measurement is shown in Fig. 2.18 where the simulation in solid line is compared to the experimental data shown as dots. A fit algorithm is applied which computes the pulse delay and searches for the B-integral parameter that minimizes a least-square error-function calculated for the temporal side bands. In the absence of B-integral, the simulated 3-ω cross correlation shows only three peaks and the energy ratio between the two pulses dictates the symmetry of the resulting trace. This can be used as an important experimental control element to precisely adjust the relative injection efficiency of the two pulses into the amplifier. In the simulation, the energy splitting ratio is adjusted numerically to fit any experimental asymmetry.

In the presence of B-integral, side bands appear and the number and magnitude of the side bands is adjusted to match the experimental data, using b as fit parameter. Fig. 2.18 shows three fits obtained for b values of 1.2, 1.4 and 1.6. The close-up view of the leftmost peak, located around -35 ps, shows that a setting of $b = 1.4$ yields the best fit to the data.

Though the pulse is split before the amplifier, the total output energy remains unchanged because the regenerative amplifier is saturated and its output is relatively insensitive to the amount of input energy. This effect is taken into account in the simulation to preserve the same b parameter in the single and two-pulse configuration. The estimated sensitivity of the measurement to variation of the pulse delay has been obtained by the adjustment of the pulse separation τ between 4 and 28 ps. The corresponding data and their respective best fits are presented in Fig. 2.19. The variation of the b parameter is $\pm$ 0.1, that is 7% of its value. The numerically sensitivity of the experiment is determined with a large enough time delay τ to have a time-intensity background lower than 10^{-6}, indeed, one finds the minimum b parameter that overcomes the noise is 0.02. The applied measurement scheme allows to cover a large measurement range from nearly no B-integral to B-integrals larger than unity.

An additional experiment was carried out using shorter pulses with a 25-fs Ti:Sa CEP-stabilized CPA laser. In this system, the sub-7 fs pulses generated by the oscillator (Rainbow, Femtolaser) are stretched using bulk material and an AOPDF to about 7 ps and amplified first up to 600 μJ in a commercial multi-pass amplifier (Femtolasers) and then up to 3.6 mJ in a second, home-made multi-pass amplifier. 25 fs, 1.8 mJ pulses are obtained after a transmission grating compressor. In order to minimize CEP fluctuations, pulse stretching is maintained at a minimal value, thus creating B-integral values greater than one, but still within the compensation-range of the AOPDF. We use the AOPDF to reduce the output energy of the first amplifier by a factor of two and to create two pulses of equal amplitude delayed by τ. The applied delay was 1 ps due to the temporal resolution of the correlator which does not allow for longer delays. The cross-correlation trace shows as well the expected pulse replica, even when the laser output energy is decreased. An unexpected asymmetry is visible in the recorded traces probably caused by a sizeable frequency shift of the replicas when the pulse-to-pulse delay is comparable to the stretched pulse width. The delay of 1 ps leads to a frequency shift of about 15 nm between the two first

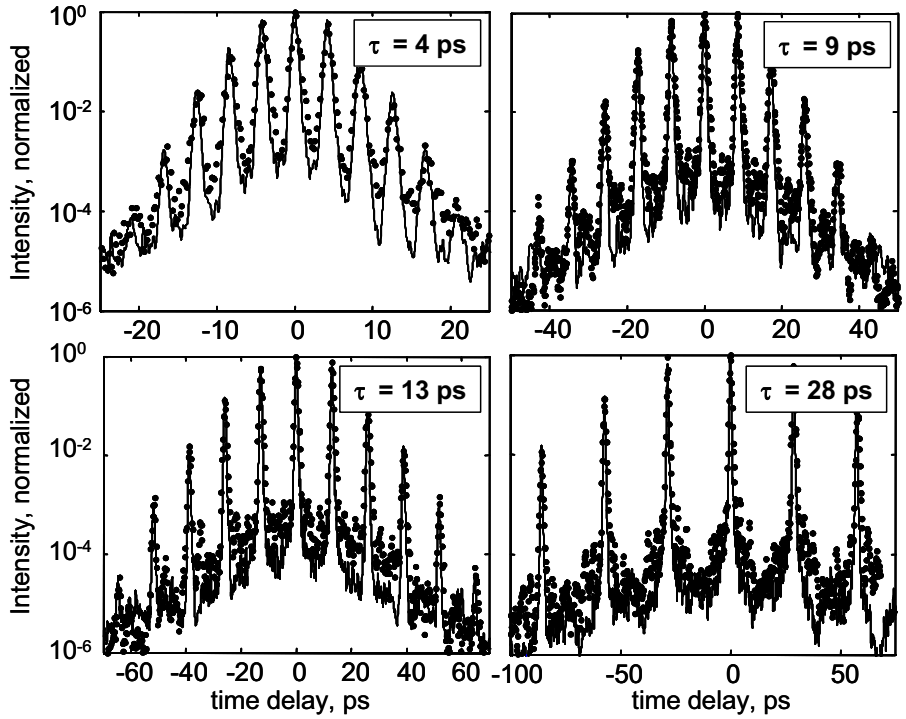

Figure 2.19: 3-ω cross correlation data and their corresponding fits for 4 different pulse-to-pulse delays (BZEK10).

replica on either side of the main pulses. Such a frequency shift certainly impacts the linearity of the measurement set-up because of the finite spectral acceptance of the frequency mixing crystals in the cross-correlator. As a result of this limitation, the asymmetry increases the experimental uncertainty of the fit parameter as can be seen on the error bars of Fig. 2.20.

A measurement was performed by varying the input pulse energy, using the AOPDF, and measuring the accumulated B-integral as a function of the amplified energy from 50 to 500 mJ (Fig. 2.20). The applied linear fit uses the zero-energy output point and the first three experimental points as input data, because the behavior of the B-integral is expected to be a linear function of the output energy in the small signal amplification case. The plot shows a different behavior, which can be explained as a signature of defocusing of the beam due to the nonlinear spatial Kerr effect, that is, a reduction of the laser intensity in the laser amplifier.

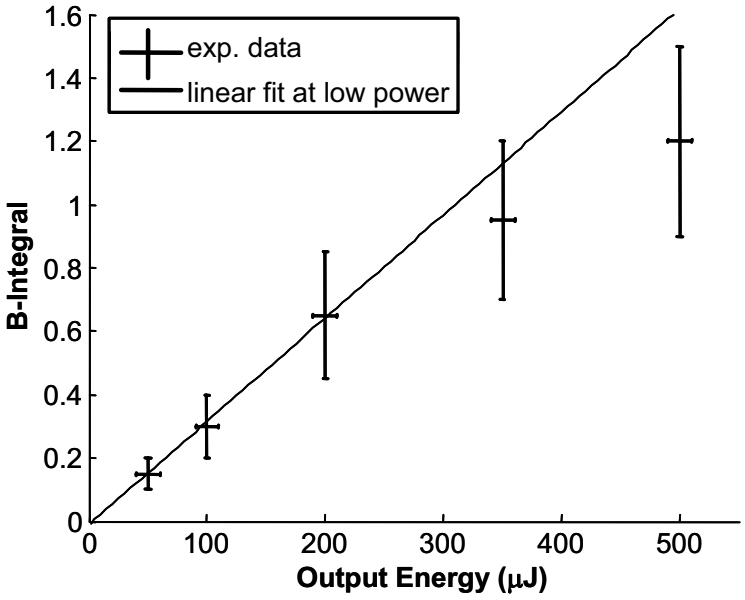

Figure 2.20: Comparison between the measured B-integral accumulation (crosses) in the laser amplifier and a linear fit (line) of the data at low output energies (BZEK10).

Conclusion

In conclusion, we demonstrated the measurement of the B-integral in CPA laser systems, using the presented method, which relies on amplifying pulse replica in the system followed by an analysis in the time domain. The measurement scheme was successfully applied to two independent laser systems exhibiting different laser parameters. The first involved a relatively long, heavily-stretched sub-picosecond laser in combination with a Mach-Zehnder unit and the second an ultra-short femtosecond CPA laser with limited stretching and an AOPDF. We measured B-integral values in the 0.1 to 1.5 radian range, only limited by the reachable laser parameters, while a measurement range starting at 20 mrad and extending to several radians is expected.

Chapter 3

Double-Pulse Single-Beam Grazing Incidence Pumping (DGRIP)

In this chapter, the principle of the Double-pulse single-beam GRazing Incidence Pumping (DGRIP) for soft x-ray lasers, as introduced in chapter 1, is described and the results obtained with this new pumping scheme are discussed. The capability to create two configurable pulses with the Mach-Zehnder in the CPA laser system which strike collinearly the target under grazing incidence, allowed for an improved generation of SXRLs. In the primary part of the chapter, the experimental results obtained with two short-pulses in the DGRIP geometry at PHELIX and LASERIX are presented. In the second part, the obtained results of the highly efficient DGRIP SXRL operation at LASERIX are discussed and compared with previous pumping schemes.

3.1 Short-pulse DGRIP

The first experimental realization of short-pulse DGRIP was performed with two collinear short pulses hitting on the target under grazing incidence, optimized for efficient traveling-wave excitation and gain zone heating. The two short pulses were of equal duration in the range around 10 picoseconds, which was different from usual approaches, where nanosecond pre-pulses and picosecond main pulses were used. The first experiment at PHELIX was carried out on Ni-like palladium (14.7 nm) and reliable lasing was achieved at less than 500 mJ total pump energy on the target. The second experiment at LASERIX investigated Ni-like molybdenum (18.9 nm)

confirming the obtained results and determining the optimal pump parameters for short-pulse DGRIP.

3.1.1 Short-pulse DGRIP at PHELIX

Set-up

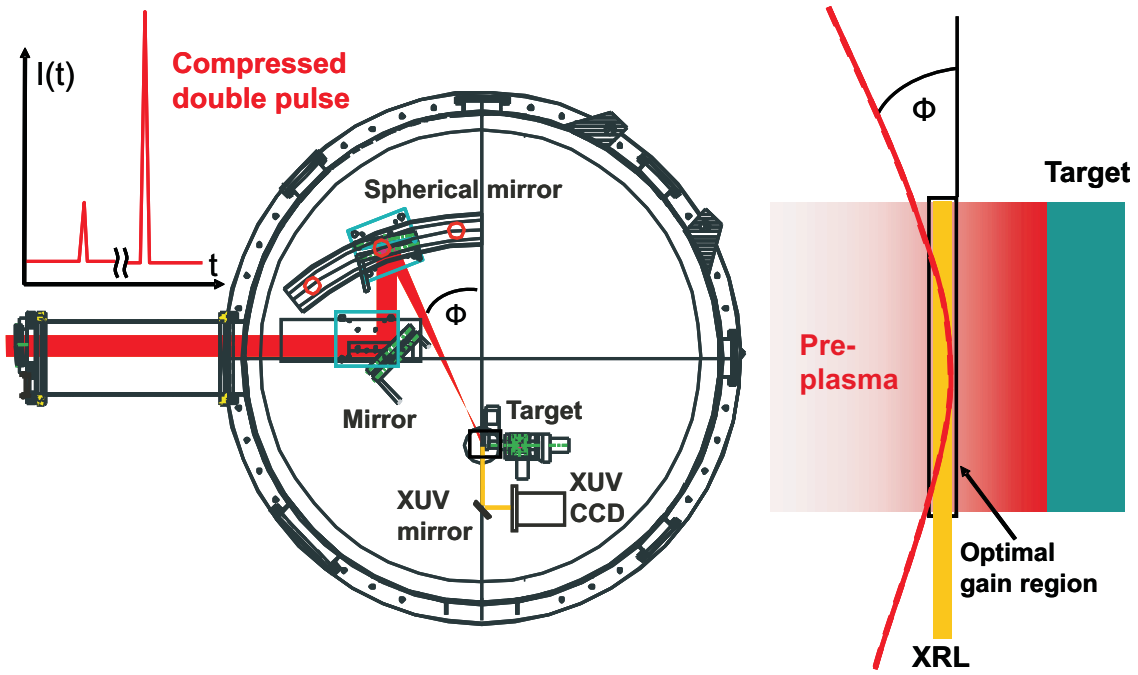

Figure 3.1: The experimental set-up on the left shows the beam line of the focussing system for the pump laser and the soft x-ray laser diagnostics. The insert to the right shows the schematic view of the grazing-incidence pumping scheme (ZZB+08).

The experimental set-up shown in Fig. 3.1 applied the focusing system of (NSC+04) which produced a line focus with an intrinsic traveling-wave speed of 1.2 c. The beam from the compressor was deflected by a flat mirror onto a spherical mirror with a focal length of 600 mm which was positioned off the normal incidence. The line focus on the Pd slab target was $5.5\,mm \times 50\,\mu m$ FWHM. Both pulses hit the target at the same grazing incidence angle Φ of 29 degrees, a value determined to be the optimal GRIP configuration in the classical scheme for the operating pump laser as shown in Fig. 3.2 (Zie07). For the wavelength of 1054 nm the electron density at which the energy is absorbed amounts to $n_{e,abs} \sim 2.3 \times 10^{20}\,cm^{-3}$, following equation 1.19.

The insert in Fig. 3.1 shows the effect of the geometry for the absorption of the two pulses on the target. The pre-pulse was - except for a possible weak pre-plasma, produced by the $< 10^{-3}$ pedestal - hitting directly onto the target, creating an expanding plume of plasma, in which the second pulse was refracted. In view of the formation of the pre-plasma, the fact that the pre-pulse had the same short time duration as the main pulse certainly introduced some difference to the typical scheme. This might have possibly caused a slight deterioration of the efficiency. However, it was assumed that thermalization should be reached before the main pulse is impinging onto the plasma. The dramatic influence of choosing the correct GRIP angle was demonstrated in Fig. 3.2. The data obtained at the apparatus in the standard pumping geometry are given, together with a spectrum of the SXRL emission. For the new geometry the optimal angle determined in the standard GRIP scheme was used. Laser operation was achieved using a pulse separation of 1 ns, seemingly benefiting from the perfect overlap of both pulses due to the same optical path, which allowed an optimized pumping of the gain region.
In the experiment the intensity ratio between the two pulses was fixed to 1:4 and the level of other pre-pulses created in the chain by ASE and other effects was below 1:1000. The resulting irradiances on the target were $\sim 3.5 \times 10^{12}\, W/cm^2$ for the pre-pulse and $\sim 1.5 \times 10^{13}\, W/cm^2$ for the main pulse respectively. The quality and orientation of the line focus were checked with a microscope imaging its shape on a glass diffuser at the final target position. The SXRL diagnostics consisted of a 2-D SXR far-field camera. The image was detected on a 16-bit back-thinned SXR charge-coupled CCD camera after a deflection by a flat multi-layer mirror optimized for 14.7 nm, and a total propagation path of 30 cm. The resolution was limited by the 26 μm pixel size. Zirconium filters were used to adjust the signal level. In the experiments using the standard pump geometry, the lasing output was also identified by a flat-field spectrometer. The clear signal as shown in the insert of Fig. 3.2 gave proof, that the recorded far-field images (Fig. 3.3) represented the Pd-SXRL emission.

Results

The SXRL output was measured by integration of the plasma background corrected counts on the SXR CCD. The SXRL intensity was recorded for pumping energies of 600 $\pm$10% mJ. To obtain comparable results the output intensities were

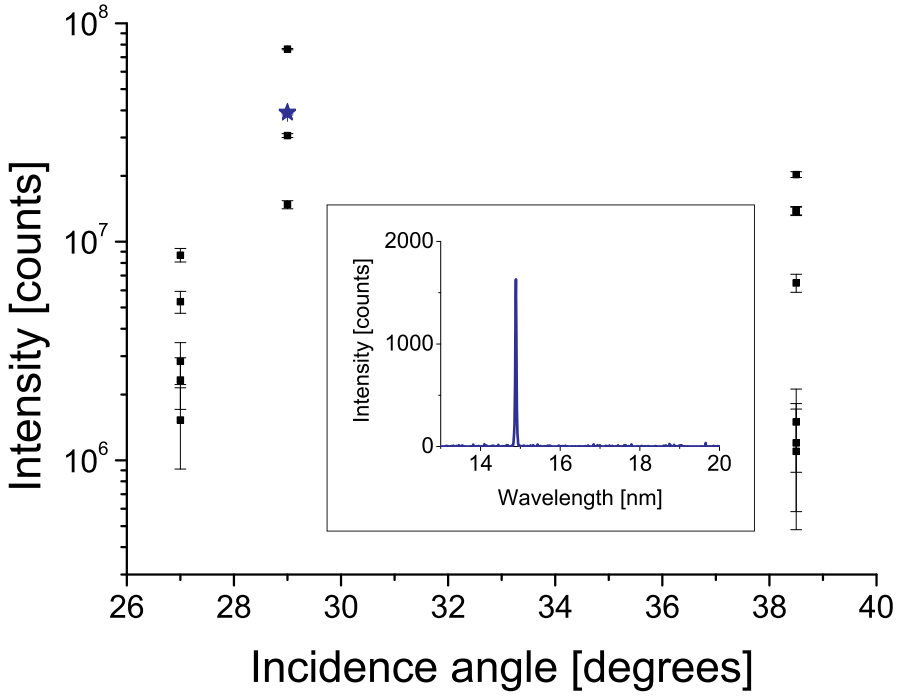

Figure 3.2: SXRL intensity as a function of the pump pulse incidence angle in the standard GRIP scheme at 27, 29 and 38.5 degrees, compared with results of the double-pulse scheme at 29 degrees (blue star). The insert shows a spectrum of the Pd-SXRL at 14.7 nm produced in the standard scheme (ZZB$^+$08).

normalized to 600 mJ pump energy and used to investigate the influence of pulse delay and pulse duration. The dependence of the SXRL output energy on the pulse separation is shown in Fig. 3.4. A maximum of the SXRL output was identified around 1 ns of delay. The width of the distribution was in the order of 0.5 ns. This indicated that the influence of the timing is similarly or even slightly less critical than reported for GRIP schemes (CKR$^+$07).

Figure 3.4 shows the result for different pulse durations, adjusted by tuning the grating-to-grating distance of the compressor, affecting both pulses equally. The pulse duration was changed between 6 ps and 28 ps. A wide maximum was observed around 16 ps, indeed a factor of 4 to 5 longer than the typical value for optimized pumping in the standard scheme (WLL$^+$05), (RWL$^+$05) even longer than used in (BGIS07) and (KKC$^+$08).

The effect of the long pump pulse duration could be related to a longer interaction time necessary to enable suitable pre-plasma conditions. In the scheme with two

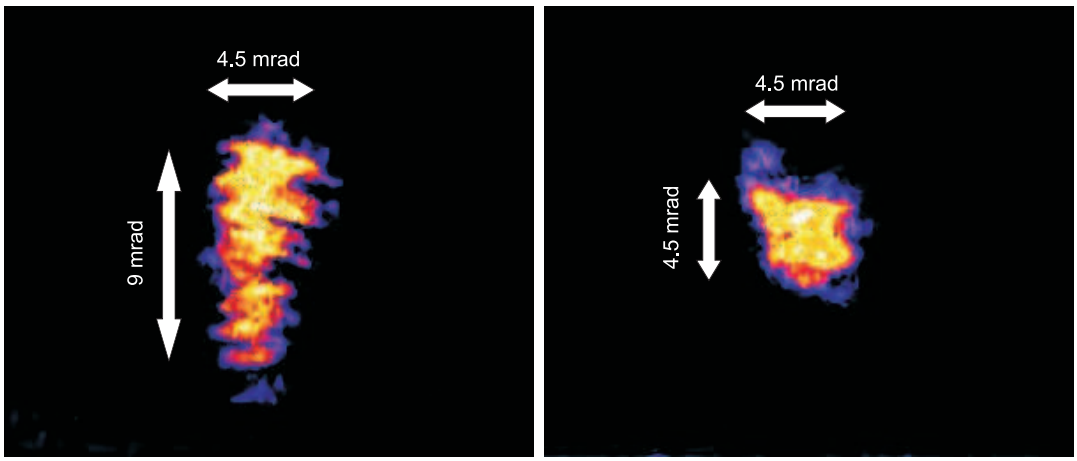

Figure 3.3: On the left: The SXRL far-field image pumped by the double-pulse scheme with 500 mJ with a vertical and horizontal divergence of $\sim$ 9 mrad and $\sim$ 4.5 mrad respectively. On the right: The SXRL far-field image pumped in the standard scheme with 700 mJ showing a divergence of $\sim$ 4.5 mrad in both dimensions (ZZB$^+$08).

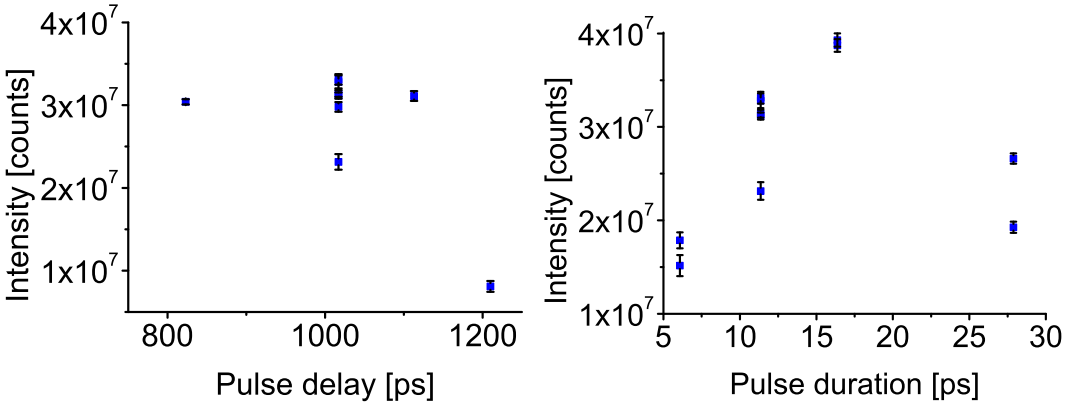

Figure 3.4: On the left: Dependence of the SXRL intensity on the time delay of the pumping pulses with a pulse duration of 11 ps. On the right: Dependence of the SXRL intensity on the time duration of the pumping pulses with a pulse delay of 1 ns (ZZB$^+$08).

equally short pulses, the duration of the pre-pulse might have been problematic in terms of the production of a homogeneous plasma plume. This could have been the reason for the untypically long optimal pulse duration. With the optimal timing and delay, lasing was achieved at pump pulse energies below 500 mJ, which is was reduction by 25% compared to the threshold of 680 mJ obtained under optimized

conditions in the standard geometry. In Fig. 3.2 the output energies at the optimum incidence angle of 29 degrees demonstrated a similar pumping efficiency for both configurations.

3.1.2 Short-pulse DGRIP at LASERIX

The obtained promising results opened the way for further investigations at high repetition-rate facilities. So a study of the short-pulse DGRIP was conducted at the laser system LASERIX for a more detailed pump parameter scan. In this case the target material was molybdenum instead of palladium, which changes the pump parameters, but gives a benchmark of the performance of the applied scheme. The set-up was similar to the previous one, but the incidence angle was set to 20 degree grazing incidence, due to the Ti:Sa wavelength of 805 nm and the target material molybdenum. The total pump energy on the target was set to 900 mJ. Double-pulse delay, pulse duration, pre-pulse energy fraction and focus size scans were carried out at 10 Hz and an optimal pump configuration was determined.

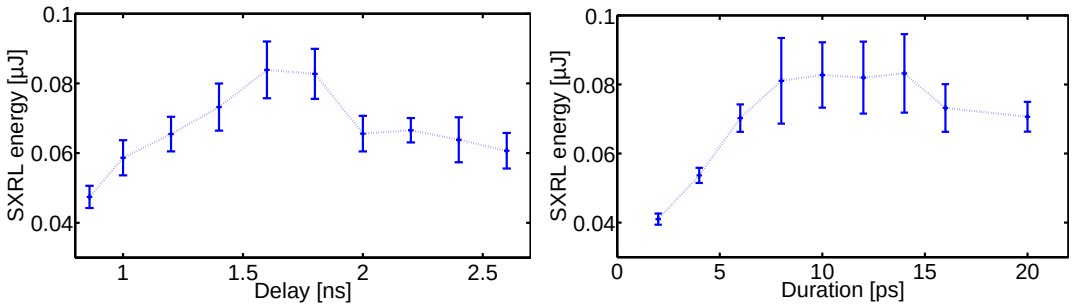

Figure 3.5: The SXRL energy is plotted versus the double-pulse delay, maximal at $\sim$ 1.7 ns, and versus the main pulse duration, maximal at $\sim$ 11 ps.

Here, the time delay between the pulses was varied from 0.86 ns to 2.6 ns for a pulse duration of 8 ps and a pre-pulse energy fraction of 15%. A maximum SXRL output is obtained at $\sim$ 1.7 ns, with a FWHM of $\sim$ 2 ns (Fig. 3.5). This shows that the delay parameter is not critical for lasing, confirming the observation for Ni-like Pd earlier in this chapter and the results by (GISB09) for similar pump conditions in Ni-like Pd. In all cases for double short pulse pumping the lasing is not as sensitive to the time delay as compared to GRIP and especially DGRIP lasers (next section). The second optimization was the variation of the pulse duration of both pulses from 2 to 20 ps for a delay of 1.6 ns and 15% pre-pulse energy fraction. In this case the

maximum SXRL output is located in a plateau at $\sim 11\,\mathrm{ps}$ with a FWHM of $\sim 10\,\mathrm{ps}$ (Fig. 3.5). The shortest pulse duration reduced the energy by a factor of two, while the longest durations only slightly decreased the output. The influence of the pulse duration is very similar to the results for Ni-like Pd. A long pulse duration plateau yields the best SXRL output, which shows the large time interval for suitable plasma conditions for SXRL lasing with this pumping scheme.

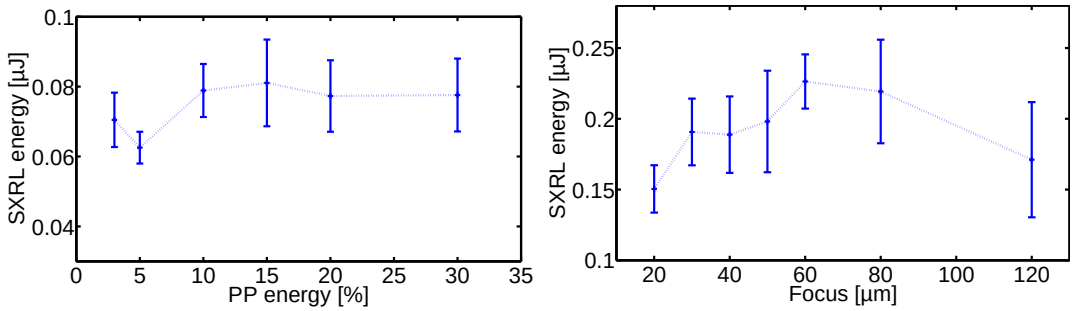

Figure 3.6: The SXRL energy is plotted versus the pre-pulse energy fraction, maximal at 15%, and versus the focus width, maximal at $\sim 60\,\mu\mathrm{m}$.

As a third investigation the pre-pulse energy fraction was scanned between 3% and 30% for a pulse duration of 8 ps and a delay of 1.6 ns. The best SXRL output was obtained at 15% (Fig. 3.6). The output did not change with increasing the energy fraction, while with lower pre-pulse fraction it decreased by 20%. This result is different from observations of (GISB09), in which they obtained a maximum output at 4.5%, but for the case of Ni-like Pd. The fourth parameter varied in this series of experiments was the focal width of the line focus. A study was done for widths of 20 to $120\,\mu\mathrm{m}$ with pump parameters of 1.6 ns delay, 10 ps duration and 15% pre-pulse fraction. Best lasing is obtained at $\sim 60\,\mu\mathrm{m}$ (Fig. 3.6). The outputs for the widest and narrowest line foci are a factor of two lower. The best focal width observed here is in agreement with the width of $50\,\mu\mathrm{m}$ applied by the previous experiment and the one from (GISB09). One has to remark that the total output energy is higher compared to the other scans, because of optimized horizontal line focus positioning on the target.

The near-field image of the SXRL was also recorded to provide the total SXRL energy as well the SXRL fluence and the source size and position (Fig. 3.7). The source size is determined to $35\,\mu\mathrm{m}$ FWHM and $8\,\mu\mathrm{m}$ FWHM for the vertical and horizontal dimension respectively. The source is located $\sim 20\,\mu\mathrm{m}$ away from the

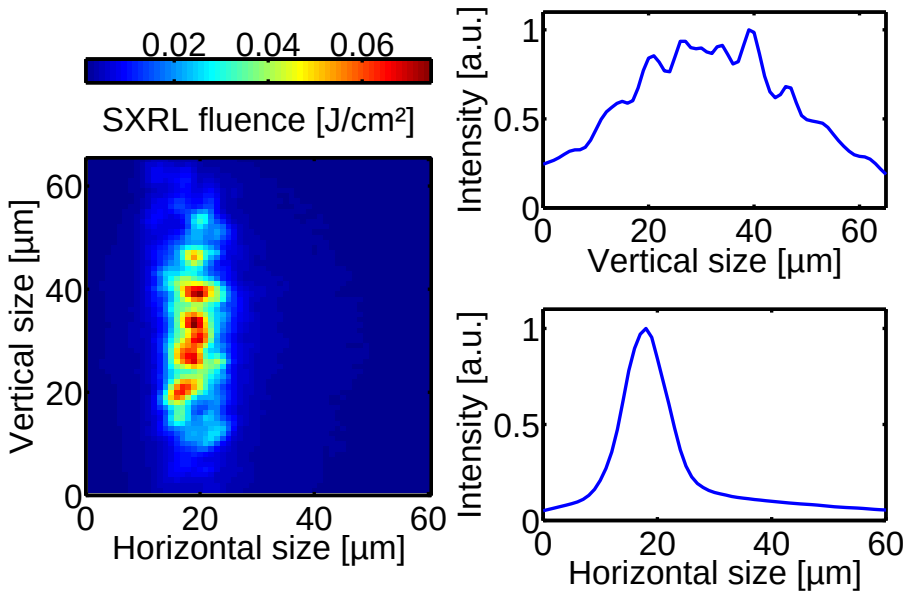

Figure 3.7: The fluence of a near-field image of a typical SXRL beam is plotted together with the line outs in vertical and horizontal dimension.

target. The divergence and the beam profile of the SXRL is recorded in 1 m distance and gave a divergence of 8.5 mrad and 5 mrad in vertical and horizontal dimension (Fig. 3.8), which reproduces the divergence values of the previous study of 9 and 4.5 mrad (Fig. 3.3).

3.1.3 Conclusion

The introduction of double short-pulse DGRIP provided a simple and efficient way to produce reliable SXRL output at close to 100 eV photon energy. In comparison to earlier work using similar double-pulse schemes the pumping energy for a reliable operation of a Ni-like Pd SXRL was strongly reduced from above 1 J ((BGIS07)) to less than 500 mJ. The improvement was attributed mainly to the optimized GRIP angle, pulse separation, and duration. The highest intensity registered on the CCD camera for Ni-like Pd corresponded to $\sim$0.3 μJ of SXRL energy at 700 mJ total pump energy. The maximum output energy for the Ni-like Mo SXRL was determined to $\sim$0.25 μJ for a total pump energy of 900 mJ, a value which was overbid in the advanced DGRIP scheme, presented in next section. However, the possibility for strong SXRL operation at pulse durations above 20 ps could be used for a further reduction of pump laser system requirements for applications (KUB$^+$07a), requiring

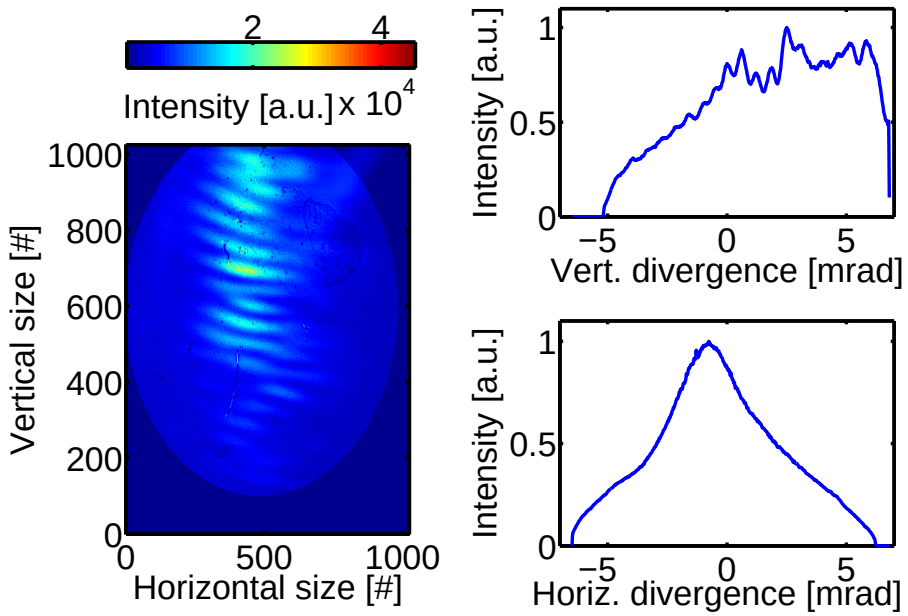

Figure 3.8: The far-field of a typical SXRL beam with a divergence of 8.5 mrad and 5 mrad in vertical and horizontal dimension, respectively, shows a structure with speckles mainly occurring along the vertical axis.

very high repetiton rates (TSJ+09).

3.2 DGRIP (long/short pulse)

In this section the further development of the short-pulse DGRIP scheme is introduced, which was termed as the double-pulse single-beam grazing-incidence pumping (DGRIP). In the DGRIP scheme the individually set long pre-pulse duration lead to a higher SXRL output energy compared to the previous short-pulse DGRIP scheme. A pump parameter optimization and an output energy evaluation of the Ni-like Mo SXRL operating at 18.9 nm were carried out at 10 Hz at LASERIX. Applying the DGRIP scheme, the full control of the pump laser parameters including the pre-pulse duration contributed to optimally generating the SXRL amplifier under grazing incidence. With this technique SXRL energies up to 2.2 μJ were obtained with a total pump energy less than 1 J. The optimized double-pulse parameters included the energy ratio, the time delay, the pre- and main pulse duration and the line focus width. The experimental results were confirmed by plasma simulations with EHYBRID.

3.2.1 Set-up

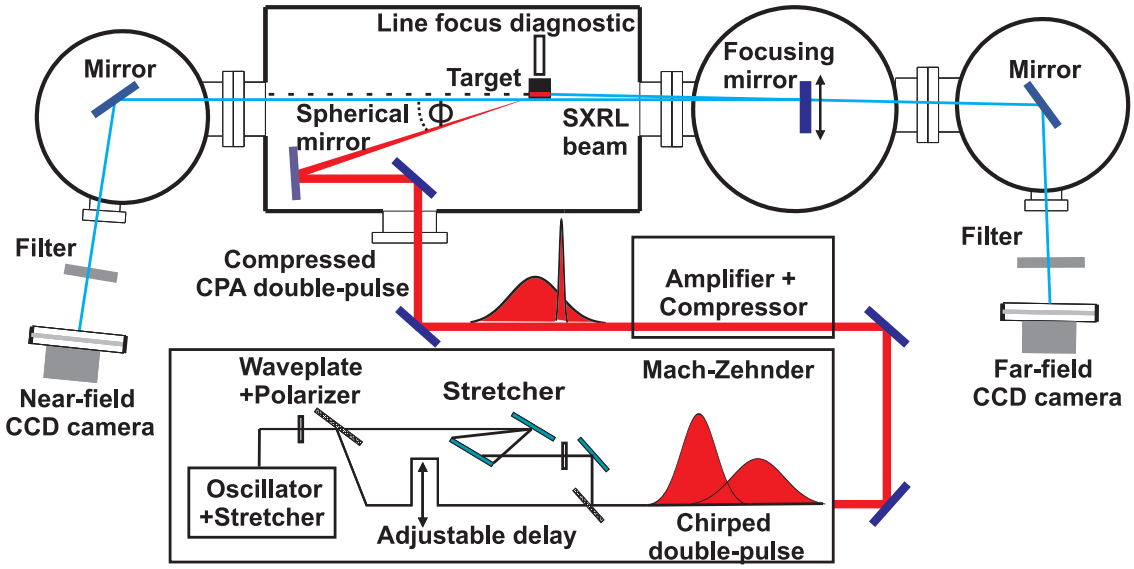

Figure 3.9: The insert box shows the creation of the chirped double-pulse, which is amplified and compressed. The double-pulse is then focused by a spherical mirror in a line onto the target, generating the SXRL beam propagating to the far-field diagnostic on the right or by a back reflection to the near-field diagnostic on the left (ZZP$^+$10).

The DGRIP set-up is shown in Fig. 3.9. After the double-pulse generation, the pump laser beam is guided in the focusing system consisting of a spherical mirror with a focal length of 600 mm aligned 10 degrees off the normal incidence, generating the line focus of $\sim$ 3 mm FWHM length and $\sim$ 60 μm FWHM width. The line focus width monitoring was realized in the IR using a high resolution imaging device (KCR$^+$08). The optimal grazing incidence angle of 20 degrees was chosen in accordance to earlier results of (KDP$^+$05) and (CKR$^+$07). This corresponded for 805 nm irradiation to a turning point electron density of $n_e \approx 2.0 \times 10^{20}\, cm^{-3}$.
The target was a 5 cm high and 4 mm wide slab of polished molybdenum. Since Mo was weakly ablated by the pump laser compared to other lasing materials, it was suitable for an operation at 10 Hz repetition rate (LLP$^+$07), allowing for up to 200 shots at the same target position, with still high SXRL output. The generated SXRL beam propagated either to near- or far-field diagnostics. A monochromatic near-field imaging system showed the SXRL source size and position relative to the

target surface and a far-field imaging system provided the divergence and profile of the SXRL beam after 1 m propagation.

3.2.2 Results

An optimization of the SXRL output inferred from the near-field has been performed in an extensive parameter scan of double-pulse time delay, pulse duration, energy balance and line focus width. Each data point represented the mean of at least 10 shots with the standard deviation as the error. The data value was taken from the integration of the counts on the CCD camera and subtracting the background from the plasma emission. Taking the quantum efficiency and the gain of the CCD camera, the filter transmission and the mirror reflectivity into account, the absolute number of SXRL photons was determined. For each parameter scan position a new target position was taken, to ensure the comparability between the scanned points. The total pump laser energy on the target was 925 ± 25 mJ for all parameter scans. By adding the extra chirp of +6 ps/nm in the Mach-Zehnder, the pre-pulse duration is set to 200 ps FWHM, different from usual pre-pulse durations of 500-1000 ps (KDP+05),(CKR+07).

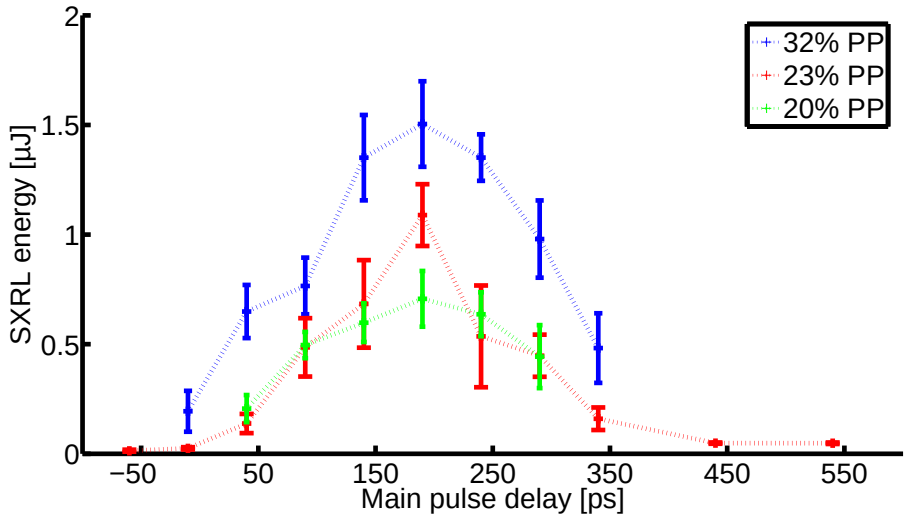

Figure 3.10: The SXRL energy is plotted versus the double-pulse delay at different pre-pulse energy fractions, maximal at 190 ps (100 ps FWHM) (ZZP+10).

The delay scan in Fig. 3.10 was performed for different pre-pulse energy fractions of 20%, 23% and 32%, and a fixed main pulse duration of 1 ps FWHM. The precise

delay timing with an error of 1 ps was done by an interferometric analysis of the two pulses. The strongest SXRL output was found at 190 ps, with a FWHM of 100 ps for all three pre-pulse conditions. The scan of the main pulse duration, shown in Fig. 3.11, was carried out for a pre-pulse fraction of 23% and a fixed optimal time delay of 190 ps. The strongest SXRL output was obtained at 1 ps, with a FWHM of 3 ps. The dependence of the energy ratio in Fig. 3.12 was analyzed with a fixed time delay of 190 ps and a main pulse duration of 1 ps FWHM. The strongest SXRL output was obtained around 27.5%, with a FWHM of 10%.

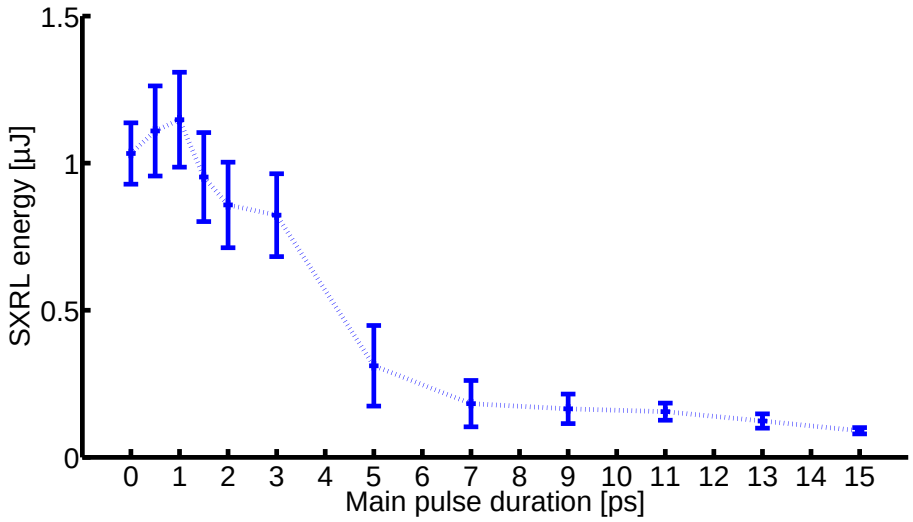

Figure 3.11: The SXRL energy is plotted versus the main pulse duration, maximal at 1 ps (3 ps FWHM) (ZZP$^+$10).

Additionally the line focus width was optimized for the strongest SXRL output at 60 μm FWHM. The influence of the horizontal line focus position on the target was crucial. An optimal position was found by moving the line focus horizontally along the target, balancing the effective length of the target against the re-absorption by the colder plasma at the exit of the amplifier. By the variation of the effective gain length up to 2.5 mm, the SXRL gain coefficient was determined to $g \sim 65\,cm^{-1}$.
The near-field of a typical SXRL beam with speckles is shown in Fig. 3.13 with an energy of 2 μJ. It had a source size of 35 μm FWHM in vertical dimension, meaning ~60% of the 60 μm focus acted as SXRL amplifier, and 10 μm FWHM in horizontal dimension, half the size compared to (KCR$^+$08). The horizontal distance of the SXRL to the target surface was only ~18 μm, which was much closer than in GRIP SXRLs (CKR$^+$07). For the same shot series, the far-field profile of the SXRL in

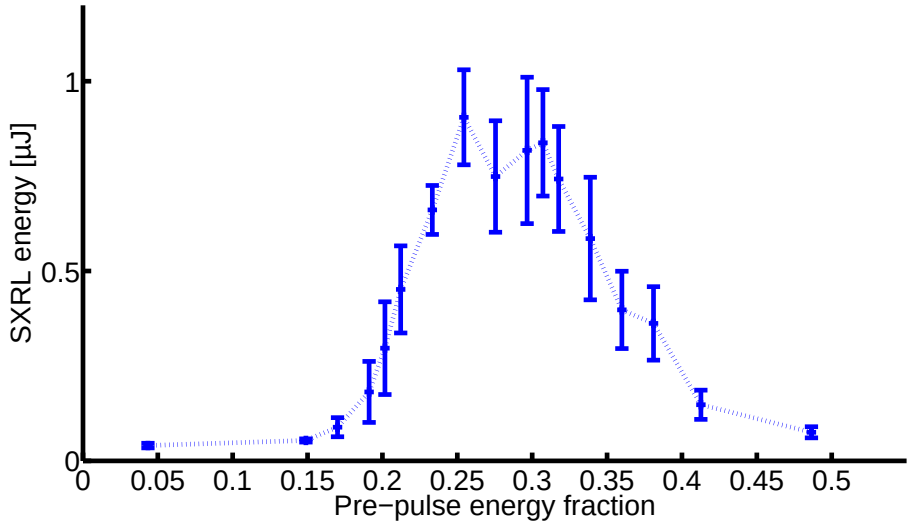

Figure 3.12: The SXRL energy is plotted versus the double-pulse energy ratio, maximal at 27.5% (10% FWHM) (ZZP$^+$10).

Fig. 3.14 showed a beam divergence in vertical and horizontal dimensions of 10 mrad and 4 mrad FWHM respectively. The horizontal divergence was comparable with GRIP SXRLs (KDP$^+$05), but the vertical divergence is increased by factor of 2, as observed in the double short pulse DGRIP scheme. The fact that in DGRIP the pre-pulse has the same small focal width as the main pulse, compared to the larger pre-pulse widths in GRIP, could produce steeper vertical density gradients, leading to stronger refraction in the vertical dimension.

A SXRL output of 2.2 μJ was obtained with an estimated gain length of only 2.5 mm, at optimized double-pulse parameters, meaning a pre-pulse to main pulse ratio of 1 : 3, a time delay of 190 ps, a pre-pulse duration of 200 ps and main pulse duration of 1 ps. The output energy was a factor 10 higher compared to the previous double short-pulse DGRIP operation. For a focus line width of 60 μm this corresponded to an irradiation intensity of $6.4\times10^{11}\,W/cm^2$ for the pre-pulse and $3.8\times10^{14}\,W/cm^2$ for the main pulse. Compared with the values of (KCR$^+$08) the pre-pulse irradiation was two times higher and the main pulse irradiation even ten times higher, introducing a difference to the plasma hydrodynamics in the gain zone.

The pre-pulse, striking the target under grazing incidence, seemingly created a pre-plasma with a steeper electron density gradient than in the case of normal incidence, so that the turning point electron density and thereby the absorption of the main pulse and the gain zone were closer to the target at $\sim$18 μm. Figure. 3.13 shows as

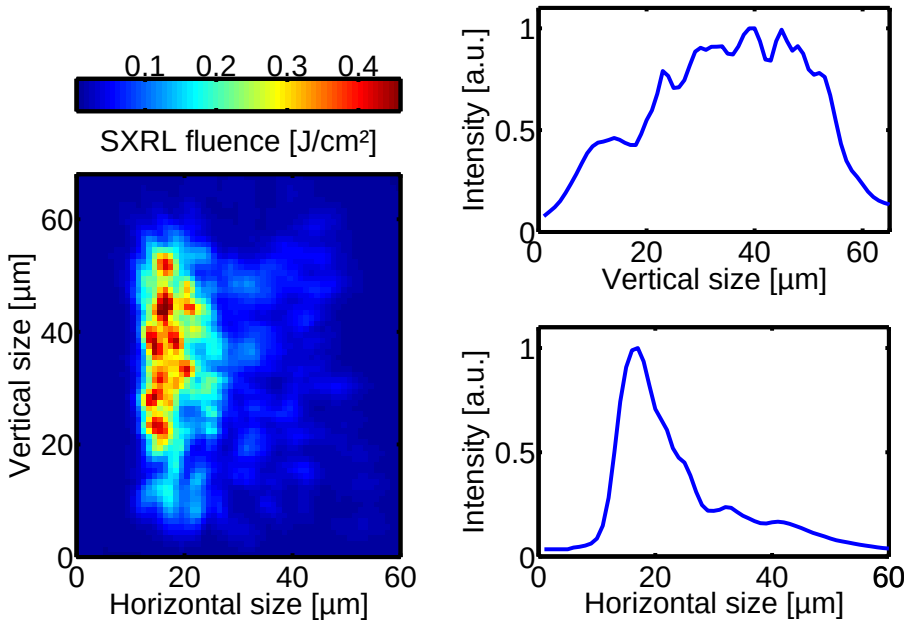

Figure 3.13: The SXRL fluence of up to $0.5\,J/cm^2$ from a near-field image of a $2\,\mu$J SXRL is plotted together with the line outs in vertical and horizontal dimension (vertical axis = target surface) (ZZP$^+$10).

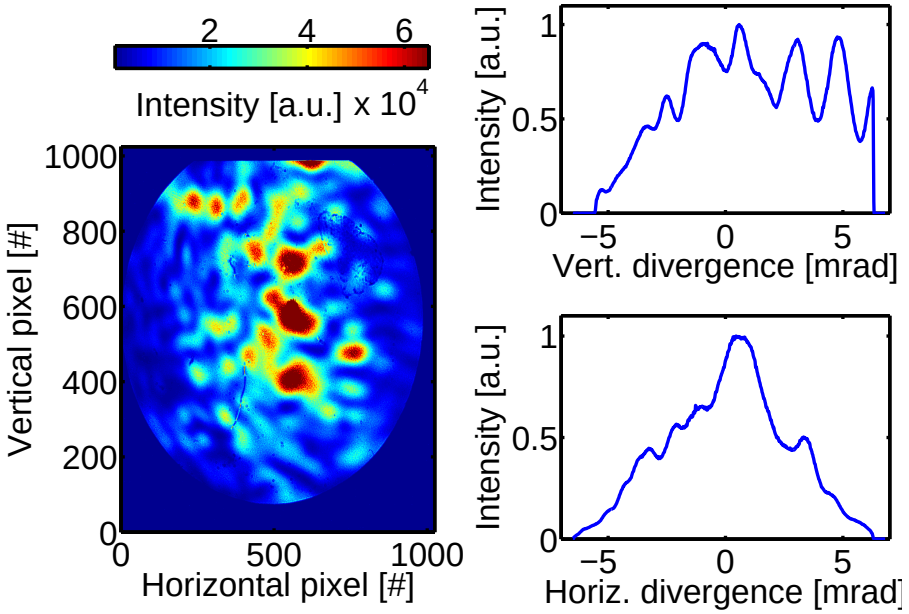

Figure 3.14: The far-field image of a SXRL beam is plotted together with the divergence line outs in vertical and horizontal dimension.

well that the gain zone expands horizontally only about 10 μm FWHM. This could also be explained by the steep electron density gradient of the pre-plasma. Since the gain was only built up in a certain electron density range, the strongly varying electron density limited the total gain expansion. However, the generation of gain in the close-by high electron density region with up to $10^{21}\,cm^{-3}$ required a high peak power of the main pulse to reach the necessary electron temperature in short time, which was fulfilled by the applied high main pulse intensity.

3.3 Simulations

In this section plasma hydrodynamic simulations are presented which were calculated with the code EHYBRID. The findings provided statements on the plasma density and gain of the DGRIP amplifier. Pump parameter scans were carried out to find the best pump pulse configuration and to compare the results with the experimental values.

3.3.1 The code EHYBRID

The analysis is primarily based on the code EHYBRID, which is used to calculate the dynamics of the pump laser/plasma interaction. It consists of a 1.5 D hydrodynamic model in which the hydrodynamic flow is treated by the one-dimensional von-Neumann-Richtmyer algorithm in the direction normal to the target surface and by a modified self-similar expansion tangential to the surface. The initial geometrical plasma width is determined by a pre-set value usually taken as the FWHM of the pumping laser pulse, and is assumed to be cut off at the plasma edge. The transition of the transverse flow from the initial quasi-rectangular profile to a Gaussian is accomplished by an empirical fit to a classical rarefaction propagating toward the center from the outer edge at a rate determined by the growth of the Gaussian $1/e$ profile width. Laser absorption occurs within the geometrical cross section of the plasma only, and is due to inverse Bremsstrahlung. For radiation normal to the target, a pre-set dump at the critical density is introduced. The laser beam may alternatively be introduced at an arbitrary angle to the target normal and refracted through the plasma, in which case resonant absorption is directly included using the standard linear form. The code considers a two temperature fluid with ion and electron (flux limited) thermal conduction and ion/electron equilibration. Ioniza-

tion and population dynamics are treated self-consistently with the hydrodynamics using an overall electron energy balance. The code can describe the ionization either by using simple modified forms of the ionization/recombination rates developed by (Gri05), as well as by a time-dependent collisional-radiative model based on either screened hydrogenic levels, or a detailed set of accurately calculated atomic levels. In the calculations presented here, the modified Griem's model (MGM) is used for the different ionization stages. For the Ni-like stage the full level populations are calculated, and used to determine the laser line characteristics, spontaneous emission rate, gain, saturation irradiance, and Lorentz and Doppler line widths (Per06).

3.3.2 Working point of short/short pulse DGRIP

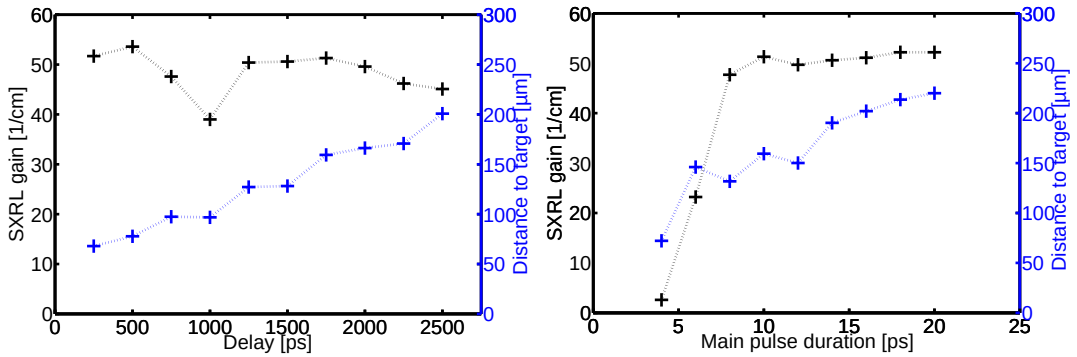

Figure 3.15: The influence of the double-pulse delay and pulse duration of both pulses on the SXRL gain are simulated for 250 to 2500 ps and 4 to 20 ps, respectively, together with corresponding the distances to the target.

The simulation of the working point of the DGRIP SXRL was performed to obtain information about the electron density distribution and temporal evolution of the gain. First, the parameters were set in the simulation to fit the experimental pump laser double-pulses for the short/short pulse DGRIP configuration. In the simulation, a pump laser wavelength of 1054 nm and a grazing incidence angle of 30 degree were applied, which corresponded to 20 degree of incidence for a Ti:Sa laser. The pre-pulse and the main pulse duration were each set to 10 ps and the laser pulse intensities were matched to fit the experimental double-pulse values. In this way a delay scan was carried out. For the pulse duration scan, the pre- and main pulse had the same duration and a fixed delay of 1.75 ns was applied. In Fig. 3.15 the simulated the results are presented. The SXRL gain was plotted for different delays

from 100 to 1000 ps with a main pulse duration of 10 ps. A maximum of $\sim 50\,cm^{-1}$ occurred at ∼500 ps and at ∼1750 ps. The second optimum is in agreement with the experimentally determined optimal delay of 1600 ps for the Ni-like Mo. The dependence of the SXRL gain on the pulse duration of both pulses for a fixed delay of 1750 ps is plotted in as well in Fig. 3.15. The maximum gain occurred at a plateau from 10-20 ps confirming the optimal pulse durations of 10-12 ps and ∼16 ps which were found in the experiments in Ni-like Mo and Ni-like Pd, respectively.

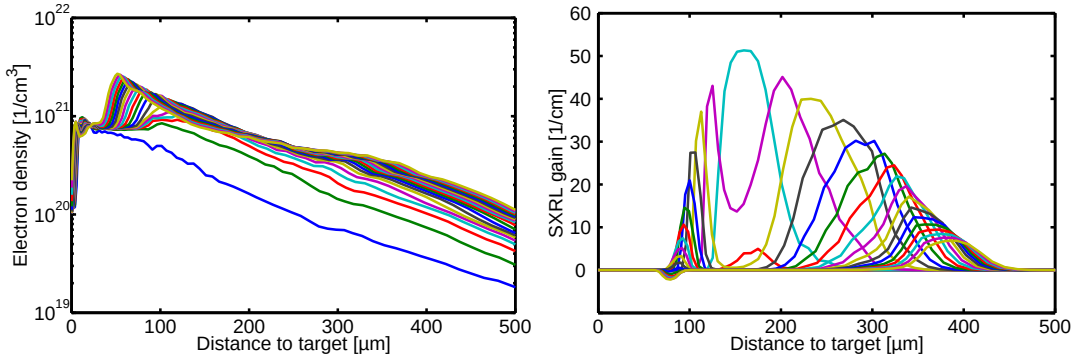

Figure 3.16: The electron density and the gain of the optimal short/short pulse DGRIP amplifier are simulated for a time interval from 0 ps (arrival of the main pulse) to 100 ps, indicated as colored 5 ps steps: green, red, turquoise, purple, yellow, brown, blue, green, red, turquoise, purple, yellow, brown, blue

In Fig. 3.16 the electron density and the gain were simulated for the optimal double-pulse parameters in the short/short pulse DGRIP scheme, determined in the previous parameter scans. The delay was set to 1750 ps and the pulse duration of pre- and main pulse to 10 ps. The graphs were plotted for 5 ps time steps in the time interval of 0 to 100 ps after the main pulse arrival. The highest gain is generated at $\sim 150\,\mu m$ at an electron density of $\sim 1-2\times 10^{21}\,cm^{-3}$. The simulated source position for the maximal gain and the corresponding electron density seem to be rather high. Unfortunately, the source position cannot be compared with experimental data due to the absence of the absolute source position.

3.3.3 Working point of long/short pulse DGRIP

The simulation of the working point of the long/short pulse DGRIP SXRL is described in this section. Again, the parameters were set in the simulation to fit the experimental pump laser double-pulses. The pre-pulse duration was set to 200 ps

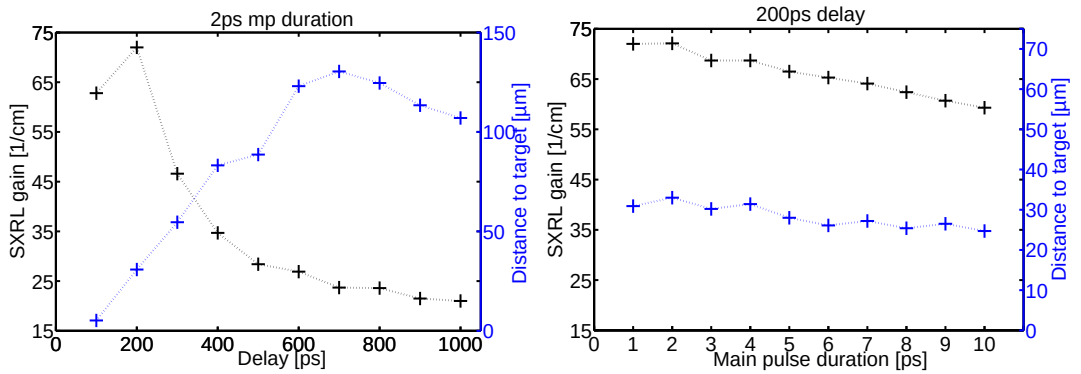

Figure 3.17: The influence of the double-pulse delay and main pulse duration on the SXRL gain are simulated for 100 to 1000 ps and 1 to 10 ps, respectively, together with corresponding the distances to the target.

and the laser pulse intensities were matched to fit the experimental double-pulse values. In this way a delay scan and main pulse duration scan were carried out. In Fig. 3.17 the simulated the results are presented. The SXRL gain was plotted for different delays from 100 to 1000 ps with a main pulse duration of 2 ps. A maximum of $\sim 75\,cm^{-1}$ occurred at ∼200 ps with a FWHM of 200 ps. These values are in agreement with the experimentally determined optimal delay of 190 ps and the determined gain value of $\sim 65\,cm^{-1}$. The dependence of the SXRL gain on the main pulse duration for a fixed delay of 200 ps is plotted in as well in Fig. 3.17. The maximum gain occurred at 1-2 ps agreeing to the main pulse duration of 1 ps which was found in the experiments to give the best performance. In the simulation the main pulse duration did not influence the gain as strongly as in the experimental study. The simulated source position for the maximal gain was located at $\sim 25\mu m$. This gain region close to the target is in good agreement with the maximal gain zone at ∼18 μm from the experiment.

In Fig. 3.18 the electron density and the gain were simulated for the optimal double-pulse parameters in the DGRIP scheme, determined in the previous parameter scans. The delay was set to 200 ps and the main pulse duration to 2 ps. The graphs were plotted for 1 ps time steps in the time interval of 0 to 20 ps after the main pulse arrival. The fact that the highest gain is generated at $\sim 30\,\mu m$ with $20\,\mu m$ FWHM leads to the interesting point that the corresponding electron density amounts to $\sim 1 - 2 \times 10^{21}\,cm^{-3}$, while the main pulse heating is fixed to the turning point density of $\sim 0.25 \times 10^{21}\,cm^{-3}$. An explanation of this discrepancy can

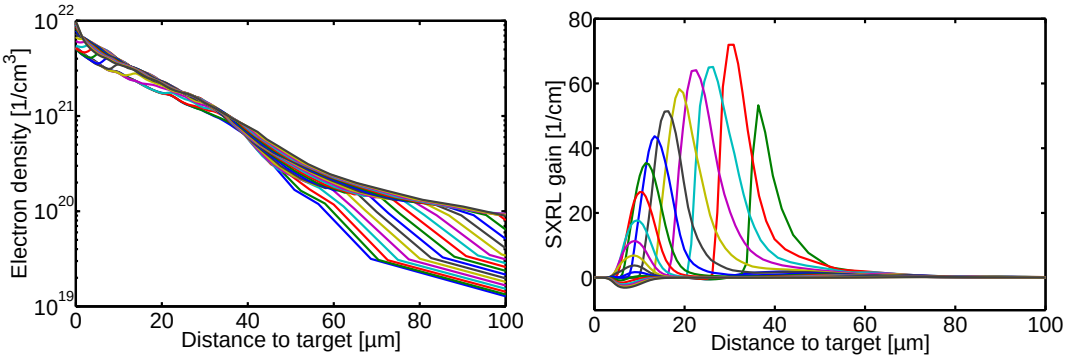

Figure 3.18: The electron density and the gain of the optimal long/short pulse DGRIP amplifier are simulated for a time interval from 0 ps (arrival of the main pulse) to 20 ps, indicated as colored 1 ps steps: green, red, turquoise, purple, yellow, brown, blue, green, red, turquoise, purple, yellow, brown, blue

be the strong gradient of the plasma which transports the main pulse energy faster to the adjacent higher density regions than in the case of smaller gradients, where longer distances have to be overcome. Such high electron densities might lead to strong refraction, and could possibly limit the maximal gain length of the amplifier. However, the measured gain coefficient of $g \sim 65\,cm^{-1}$, a value 50% stronger than reported by GRIP schemes (CKR$^+$07),(LWL$^+$05), corroborates the assumption of a higher electron density in the gain region, since the gain is proportional to the electron density. Moreover, the SXRL operation in denser plasmas allows in principle for larger spectral width, giving the possibility to reach a shorter pulse duration in an injection-seeded amplifier.

3.4 Conclusion

3.4.1 Comparison between short/short pulse DGRIP and long/short pulse DGRIP

The two variants of DGRIP apply the common principle of double pump pulses in a single beam under grazing incidence, allowing for the same set-up, but by changing the pre-pulse duration from ∼10 ps for the short/short pulse configuration to ∼200 ps for the long/short pulse configuration, significant differences occur. Completely other optimal pump parameters were obtained during the SXRL output optimization

Table 3.1: Comparison between the short/short pulse and long/short pulse DGRIP with pump and output parameters

DGRIP	short/short pulse	long/short pulse
PP duration	$\sim 10\,\mathrm{ps}$	$\sim 200\,\mathrm{ps}$
MP duration	$\sim 10\,\mathrm{ps}$	$\sim 1\,\mathrm{ps}$
PP energy	$\sim 250\,\mathrm{mJ}$	$\sim 250\,\mathrm{mJ}$
MP energy	$\sim 750\,\mathrm{mJ}$	$\sim 750\,\mathrm{mJ}$
Delay	$\sim 1600\,\mathrm{ps}$	$\sim 200\,\mathrm{ps}$
Focus width	$\sim 60\,\mu\mathrm{m}$	$\sim 60\,\mu\mathrm{m}$
PP intensity	$\sim 3 \times 10^{12}\,W/cm^2$	$\sim 6 \times 10^{11}\,W/cm^2$
MP intensity	$\sim 5 \times 10^{13}\,W/cm^2$	$\sim 4 \times 10^{14}\,W/cm^2$
Number of pulse trains N	~ 5	~ 2.5
Max. output fluence	$\sim 0.07\,mJ/cm^2$	$\sim 0.5\,mJ/cm^2$
Max. output energy	$\sim 0.3\,\mu J$	$\sim 2\,\mu J$

resulting in SXRL beams with different near- and far-field characteristics.
In Tab. 3.1 a summary of the optimal pump parameters is given together with the output characteristics for both DGRIP variants. The strongest differences in the pump parameters are observed in the delay and duration of the double-pulses. The main pulse duration of 10 ps in the short/short pulse configuration differs strongly from the long/short configuration, in which a main pulse duration of only 1 ps is applied. Moreover in the case of short/short pulse pumping the very long delay of $\sim$ 1500 ps clearly stands in contrast to the rather short delay of 200 ps for the long/short pulse configuration. The different pump parameters clearly show the differences in the plasma hydrodynamics leading to very different near and far-field SXRL beam characteristics which will be discussed here.
The observed far-field SXRL intensity patterns result from the interferences between the field amplitudes emitted by numerous small regions of uniform phase at the source exit. The observed speckles in the far-field of the long pre-pulse short main pulse DGRIP configuration have a typical angular size of 0.1 to 0.5 mrad and are randomly distributed in the beam profile. They result from diffraction of the spatially coherent beam by a random phase. Contributing to the observed beam profiles are the low spatial coherence, the high longitudinal coherence associated

with the short pulse duration. One can define the factor $N = \frac{\tau}{\tau_c}$ with the ratio of the pulse duration τ and the coherence time τ_c. This factor determines the contrast V of the far-field speckles by $V = \frac{1}{\sqrt{N}}$, it decreases with the square root of N. Since N is in the order close to unity for TCE SXRL, strong speckles can be observed. A typical speckle pattern shown in Fig. 3.14. The factor N is also termed as the pulse train number, describing the number of coherent pulse trains contained in the total SXRL pulse envelope. To determine the number of pulse trains the contrast of the far-field pattern was analyzed. The contrast V was determined by the ratio between the standard deviation σ_N of the intensity and the averaged intensity $< I_N >$. For a typical far-field pattern (Fig. 3.14) a pulse train number of $N \sim 2.5$ was determined, which agreed well with the values from (GKC$^+$06).

For QSS SXRL the pulse duration is typically about 100 ps while the coherence time stays ∼2 ps. This leads to a much higher ratio of $N \sim 50$ and the far field pattern becomes uniform without speckle structures, as shown in (RMP$^+$02). A uniform intensity pattern can also be obtained with TCE SXRLs by the accumulation of multiple shots, as reported in (ZZH$^+$10). The original speckle structure is smeared out with the square root of the number of shots and results in a similar pattern obtained with stationary partially coherent sources like QSS SXRLs. The experimental data in (ZZH$^+$10) proved that an integration of 100 shots provided a homogeneous illumination profile. An integration of 100 shots corresponds to an accumulation time of about 100 ps, which equals the pulse duration of one QSS SXRL shot.

A totally different pattern is observed in the far-field of the short/short pulse DGRIP configuration which shows mostly interference fringes instead of the typical speckle pattern. The fringes have a lower contrast compared to the speckles of the long/short pulse DGRIP far-field resulting in a higher number of pulse trains which was determined to $N \sim 5$. This value is about a factor of 2 higher than the one measured in the long/short pulse DGRIP. Assuming for both cases a similar coherence time, this leads to two times shorter SXRL pulse duration in the long/short pulse DGRIP. The observation is also supported by the shorter main pump pulse duration of 1 ps applied in long/short pulse DGRIP (Fig. 3.11) compared to the 10 ps duration in the short/short pulse scheme (Fig. 3.5).

The observation of fringes can be explained either by the fact that the horizontal source size of about 8 μm is 30% smaller than the value from the long/short pulse DGRIP (Fig. 3.7, Fig. 3.13), causing fringe-like far-field patterns, as reported

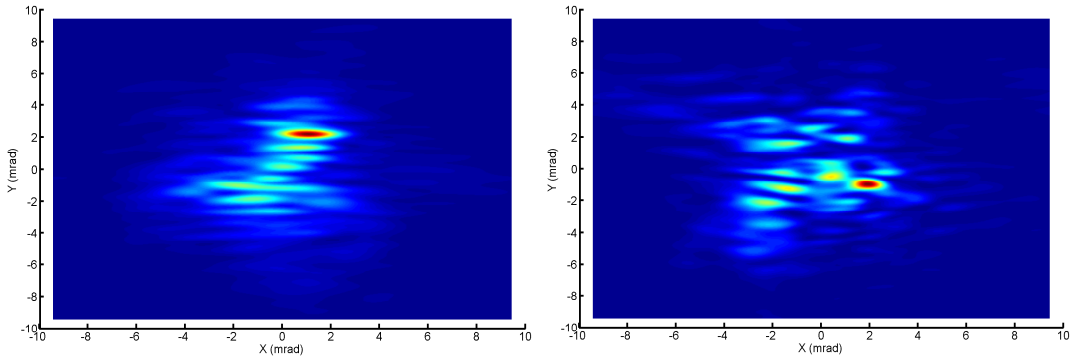

Figure 3.19: Simulations of the SXRL far-field for a gaussian source with a vertical size of 35 μm and a horizontal size of 8 μm (left) and 12 μm (right), respectively.

by (GKC+06). In Fig. 3.19 the far-field pattern are simulated for different gaussian sources with a vertical size of 35 μm and a horizontal size of 8 μm and 12 μm, respectively. One can see that by changing the aspect ratio of the source size the far-field pattern changes from a fringe-like structure to a speckle-like structure, similar to the observations in the experiment.

Another explanation for the far-field fringes in Fig. 3.8 can be the existence of multiple sources in the emitting near field of the plasma amplifier which then interfere in the far-field. As can be seen in the near field in Fig. 3.7, multiple strong point-like sources are located along the vertical axis, which support the assumption of a multi-source interference. However, this kind of interference implies that the sources are mutually coherent, which is typically not the case in ASE lasers. But if one investigates the spacing of the fringes, which was determined to $\sim$0.6 mrad, one finds a distance of $\sim$30 μm between two possible emitting sources. This distance is well within the total vertical dimension of the near field of $\sim$35 μm.

To determine the more elaborated pump configuration in the DGRIP scheme, one of the most important values, the total output energy, has to be considered. Here, the SXRL output clearly identifies the long/short pulse DGRIP configuration as the much more efficient approach. With a SXRL energy of $\sim$2μJ, which is a factor of 7 higher than in the double short pulse configuration, the long/short pulse DGRIP scheme easily reaches the efficiencies obtained in the standard GRIP scheme (CKR+07).

3.4.2 Comparison between GRIP and DGRIP

In conclusion, a comparison between DGRIP and GRIP in terms of efficiency and stability during the experiment has been considered. Since the DGRIP scheme applied two collinear pulses, which passed through the grating compressor at LASERIX with a transmission of $\sim 50\%$, the total pump energy was reduced by $\sim 25\%$ from $\sim$ 1.2 J on target for the GRIP operation to ~ 0.9 J on target for the DGRIP operation. Despite the lack of pump energy in the DGRIP case, both methods yielded about the same maximal output energy of $\sim 2\mu J$, resulting in a higher efficiency of the DGRIP scheme. This corroborated the high gain value of $\sim 65\,cm^{-1}$ in DGRIP. Moreover, the more compact source size of $\sim 350\mu m^2$ in DGRIP compared to $\sim 700\mu m^2$ in GRIP lead to a doubled SXRL fluence of $\sim 0.5\,J/cm^2$. Instead, the vertical divergence in the DGRIP output was increased to ~ 10 mrad, contrary to the horizontal divergence of ~ 4 mrad, which is a typical value for both dimensions in the GRIP scheme. The resulting peak brilliance of $\sim 2\times10^{25}$ photons$/(s\,mm^2\,mrad^2)$ in 0.01% bandwidth for the DRIP scheme equalled again the values of GRIP SXRLs, and amounted to a factor of ten less than the brightest seeded GRIP SXRL (WGP$^+$08). Since in this study only a gain length of ~ 2.5 mm was investigated, possible limiting refraction effects due to the higher density operation, could not be observed. In terms of stability, the DGRIP scheme came with an intrinsically perfect overlap of the line foci for both pulses, resulting in a more stable SXRL operation, compared to the jittering output of GRIP. On top of that, the easy and rapid alignment procedure simplified the utilization of the DGRIP scheme for applications.

Chapter 4

Application of DGRIP

This chapter is divided in two parts. The first part reports on the application of DGRIP for shorter wavelength SXRL pumping with unique high-energy double-pulses at the laser facility PHELIX, showing the potential of the DGRIP scheme for the expansion to shorter wavelengths. The second part deals with the application of the DGRIP SXRL for high repetition rate irradiation experiments of user samples at the laser facility LASERIX. Regulated SXRL energy doses were deposited automatically on samples, which were under investigation by an external user group.

4.1 DGRIP for short wavelengths

The previous successful results of generating transient collisionally excited soft x-ray lasers at sub 20 nm in the double-pulse single-beam grazing-incidence pumping scheme, justified its application also to shorter wavelengths. The experiment presented here was aiming at the optimizing of the pump parameter configuration, to reach as short a lasing wavelength as possible and to give limits for the feasibility of such soft x-ray lasers at pump energies below 40 J for the implementation at the high repetition rate facility LASERIX. The study was performed at the PHELIX facility with its unique installation of fully configurable high-energy double-pulses of up to 150 J. The application of DGRIP, enabled to achieve - with a much simplified set-up - lasing down to the shortest wavelength reached to date for TCE SXRLs. 7.36 nm Ni-like Sm soft x-ray lasing was achieved only by a pump laser energy of 36 J (ZBE$^+$09a), reducing the pump energy requirements by a factor of two compared to (KPM$^+$01). The set-up of (KPM$^+$01), which used two separate laser beam lines

to interact with the target, was a non-trivial complication, because of the delivery of two beams with large dimensions required by the high pump laser energy. More suitable was the approach of (KST$^+$04) to pump Ni-like La at 8.8 nm, with two collinear pulses interacting with the target under normal incidence. This set-up is similar to the DGRIP scheme for operation at short wavelengths (ZRG$^+$10), which is presented here.

4.1.1 Set-up

The experimental set-up in Fig. 4.1 shows the DGRIP geometry for short wavelengths. The focusing system consisted of a diamond free-formed 90 degree copper off-axis parabola (OAP) with a diameter of 300 mm and a focal length of 1500 mm. The aberrations, produced by a tilt Θ of 4 degrees off the normal off-axis angle, created the line focus without requiring additional optics. The target was rotated to fit the plane of the line focus, resulting in a total incidence angle Ω of 73 degree under which the laser double-pulse stroke the target with s-polarisation. This corresponded to a grazing incidence angle of 73 degree, a much higher angle as compared to the geometries for softer x-ray lasers shown in the previous chapter. The range of incidence angles that could be reached in the geometry of the focusing system applied here, was well suitable for higher electron density laser absorption. The 73 degree of grazing incidence on the target resulted in an absorption at $9.2 \times 10^{20}\, cm^{-3}$ for the pump laser wavelength of 1.054 μm.

The size of the line focus was $\sim 9\, mm \times 20\, \mu m$ (Fig. 4.2), giving an irradiance of $\sim 5 \times 10^{13}\, W/cm^2$ for the pre-pulse and $\sim 1.5 \times 10^{15}\, W/cm^2$ for the main pulse respectively, for a total pump laser energy of 40 J. The size and the positioning were controlled via an infra-red CCD camera in the 10 Hz low laser energy mode. For maximal soft x-ray laser output the line was shifted horizontally to the amplifier exit of the target reducing the total length to $\sim$ 7 mm, which was enough for efficient operation, and probably in the saturated regime. During a full laser shot the focus control was done with a x-ray pinhole camera with filters consisting of 1 μm of C3H6 and 20 μm of Al imaging the full line focus onto the camera chip. The magnification was $f_{mag} = 2.36$ and together with a pinhole size of s_{pin}=20 μm the resolving power was determined to be 28 μm. The line width of the plasma line s_{obj} gave 66 μm

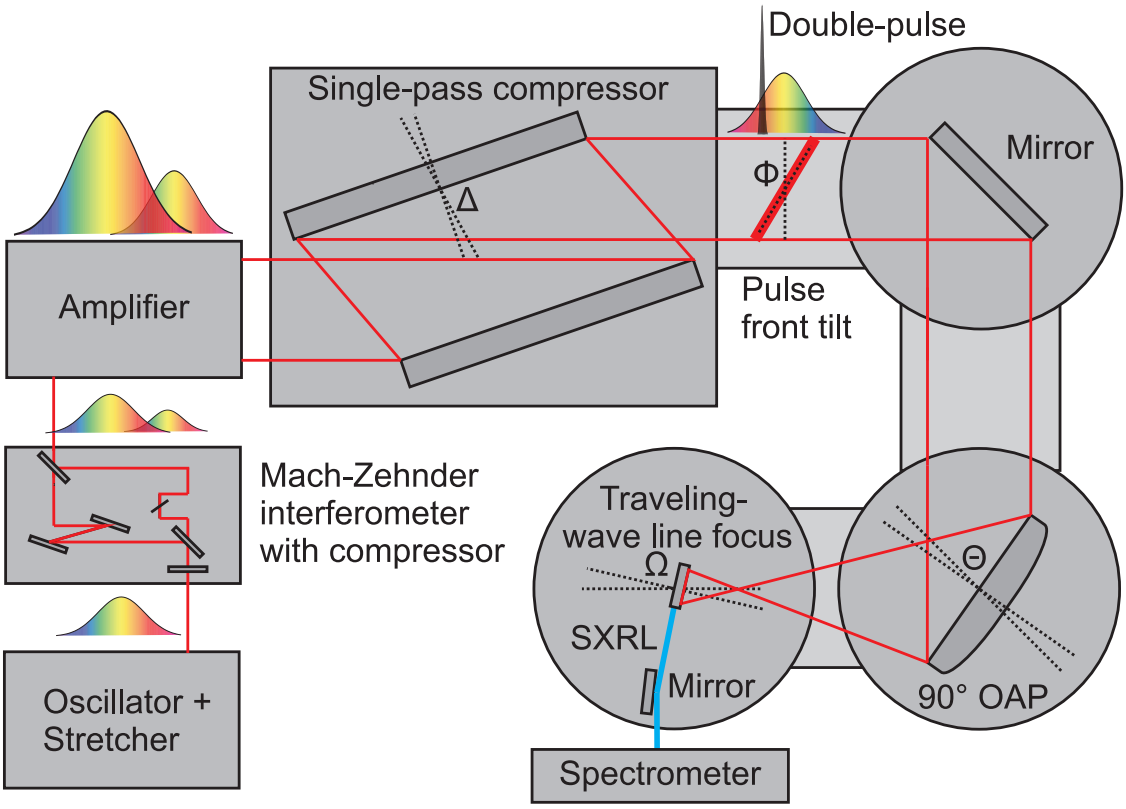

Figure 4.1: The experimental set-up shows the double-pulse generation, the pulse front tilt control, the focusing geometry and the soft x-ray laser diagnostic.

FWHM and 78 μm FWHM for a $\sim$ 40 J and $\sim$ 100 J shot, respectively, with

$$s_{obj} = \frac{\sqrt{w_{img}^2 - (s_{pin} \times (1 + f_{mag}))^2}}{f_{mag}}, \tag{4.1}$$

where w_{img} was the size of the line focus in Fig. 4.3.

The targets were $10 \times 10\,mm^2$ samarium slabs polished to the crystalline surface structure. The targets were stored under high purity inert gas until shortly before mounting them on the target holder and evacuating the chamber. For each shot a new target position was chosen, far enough from the previous position to be free from the debris created by the pump laser. With the given target size typically 4-5 shots could be placed on one target.

The tuning of the traveling-wave speed was done by the rotation of the second grating of the two-grating compressor, thereby changing the pulse front tilt, similar to (CSS$^+$00). Tilting the grating introduced a different path length for each point

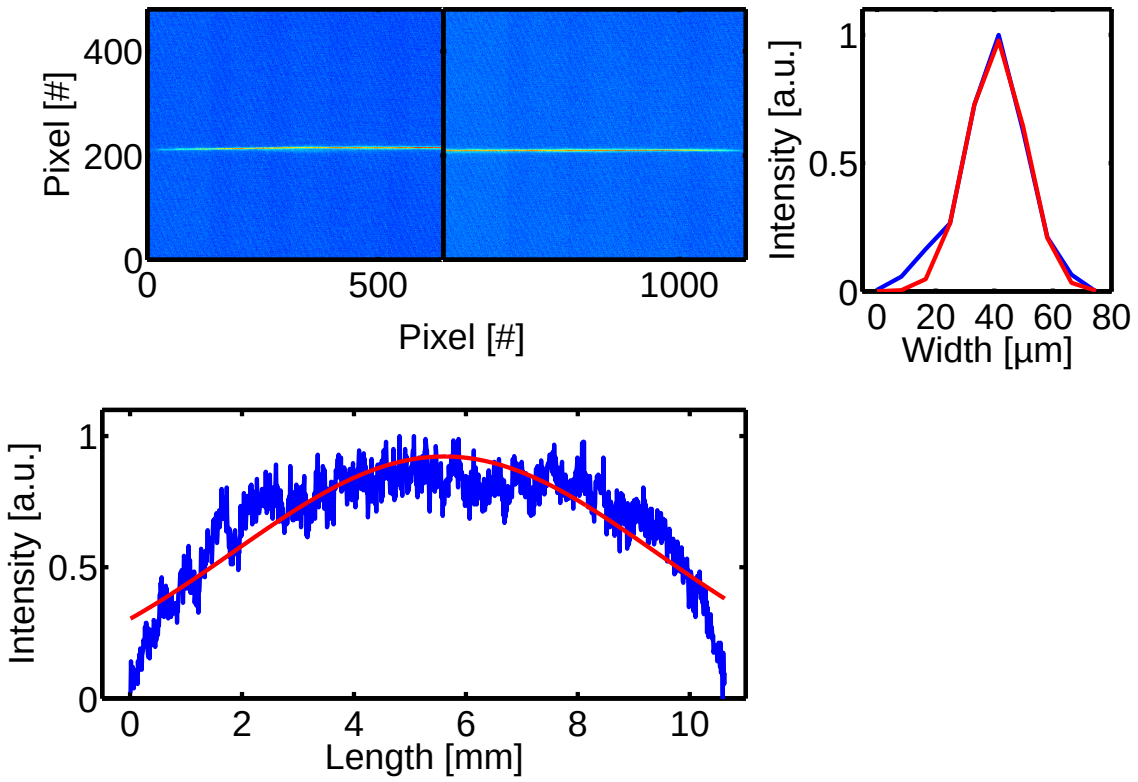

Figure 4.2: The line focus produced by the OAP has a length of 9 mm and and width 20 μm.

along the beam horizontal axis according to:

$$\Phi(\omega) = \Delta \frac{\omega}{c} \frac{x}{cos(\Theta_i) sin(\Theta_r)} [1 + cos(\Theta_i - \Theta_r)] \tag{4.2}$$

where x was the extension of the beam along the horizontal axis, Δ was the grating tilt angle, Θ_i and Θ_r were the incidence and diffracted angles at the pulsation ω in the case of the aligned compressor respectively. This equation showed that a spatially dependent additional phase term was added to the pulse, meaning that the compression was not spatially uniform. However, one could show that, when the beam was large compared to the spectral spread on the grating, the increase in pulse duration at the edge of the beam was minimal. For instance, a 0.17 degree grating tilt yielded a 30 ps delay at the focus when a 12 cm beam was used, but at the expense of an increase of pulse duration by 250 fs at the edge of the beam only. During the alignment phase, a test plate with two holes separated by 10 mm was located at the target plane. The two beams were then focused into a nonlinear

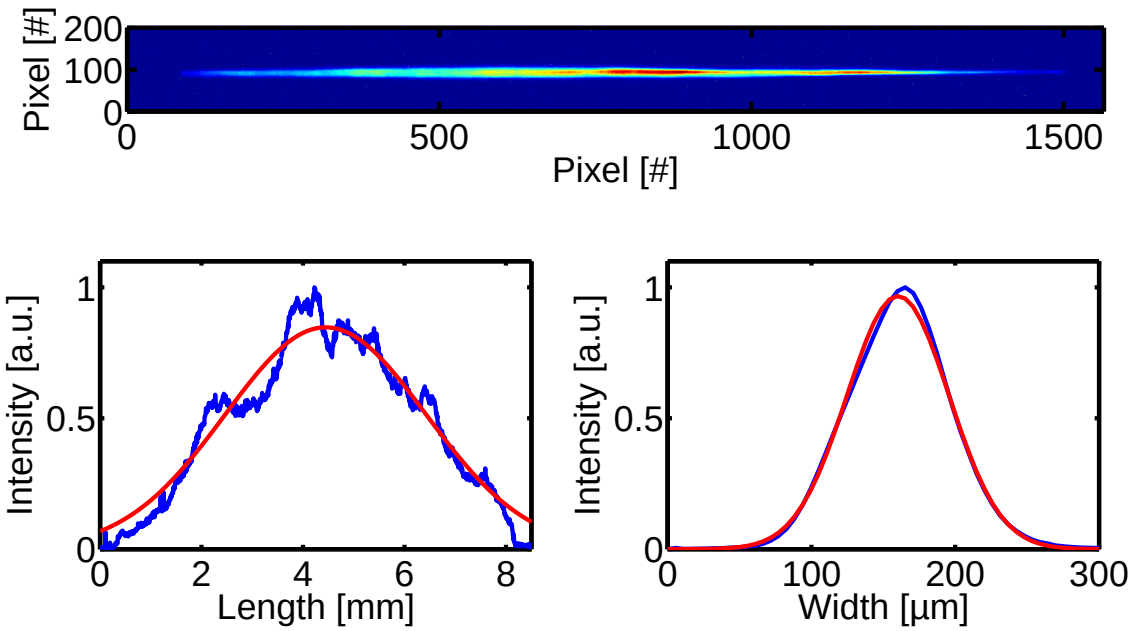

Figure 4.3: The line focus for a laser energy of 100 J shows slightly modulated intensity along the line focus length of 7 mm. The width is determined to 78 μm FWHM.

crystal were second harmonic light was generated (Fig. 4.4). A double-pulse of two delayed 1 ps pulses was used at this point to control the amount of pulse front tilt introduced by the compressor. Practically, this corresponded to turning the grating in the compressor until the delay necessary for getting a traveling-wave speed of 1 c along the line focus was reached, which equalled 33 ps or a distance of 10 mm on the delay stage of the double-pulse set-up, an autocorrelation mechanism. In this way the intrinsic traveling-wave speed of 2 c of the line focus was compensated to $1 \pm 0.1\,c$. Due to the traveling-wave pumping the soft x-ray laser emission exited the target on one side as shown in Fig. 4.1. High energy background radiation from the plasma plume was partly eliminated by a grazing incidence reflection of the SXRL beam at 6.5 degrees on a polished fused silica substrate with a roughness of 5 nm rms, guiding 20% of the SXRL beam into the spectrometer. The infra-red and visible background was suppressed by two 0.8 μm thick carbon filters. The SXRL output was imaged via a flat-field gold grating spectrometer with 1200 lines/mm onto a CCD camera at 1.25 m distance to the target.

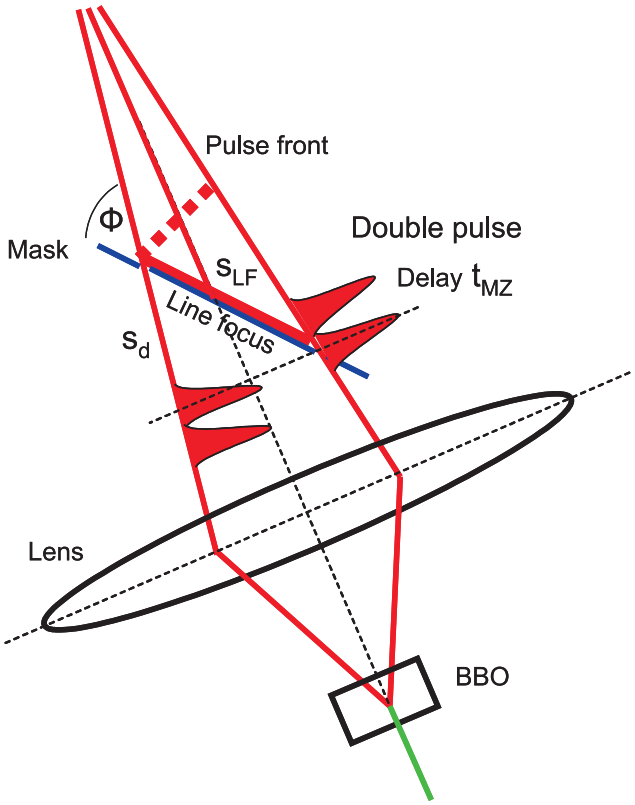

Figure 4.4: The set-up for the pulse front tilt tuning to optimize the traveling-wave speed of the line focus on the target.

4.1.2 Results

The pump parameters for highest SXRL output were determined by a delay scan from 20 ps to 375 ps, a scan of the double-pulse energy ratio between 10% and 70% and a scan of the total pump energy from 85 J to 36 J. The pre-pulse and main pulse duration was set to 200 ps and 7 ps respectively for this study. The contrast level was better than 10^{-6}, except an extra pulse of 10^{-3} located 900 ps before the double-pulse. The obtained spectrum (Fig. 4.5) showed the lasing of the $4d_{(3/2)} - 4p_{(3/2)}$ transition at 168.5 eV (7.36 nm) and also the second weaker lasing $4d_{(3/2)} - 4p_{(1/2)}$ transition at 181 eV (6.85 nm). The line out of the spectrum was corrected with the reflectivity of the gold grating and the fused silica substrate and the transmission values of the carbon filters. Since the resolution of the spectrometer was about $\Delta\lambda/\lambda = 10^{-3}$ and the line width of an SXRL in the order of $\Delta\lambda/\lambda = 10^{-4}$ (SDH$^+$03b),(KGR$^+$06) one found that the signal to noise ratio shown by the spectrum was underestimating the strength of the laser line by a factor of 10, which

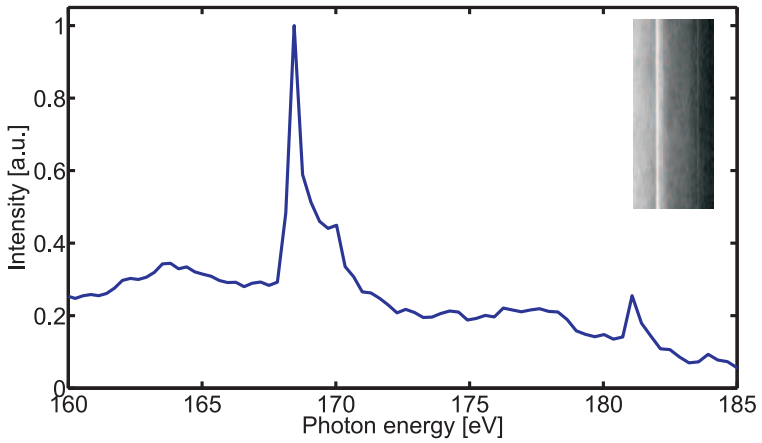

Figure 4.5: The line profile of the recorded spectrum (see insert) shows the lasing lines of Ni-like Sm at 168.5 eV (7.36 nm) and at 181 eV (6.85 nm).

was not included in further calculations.

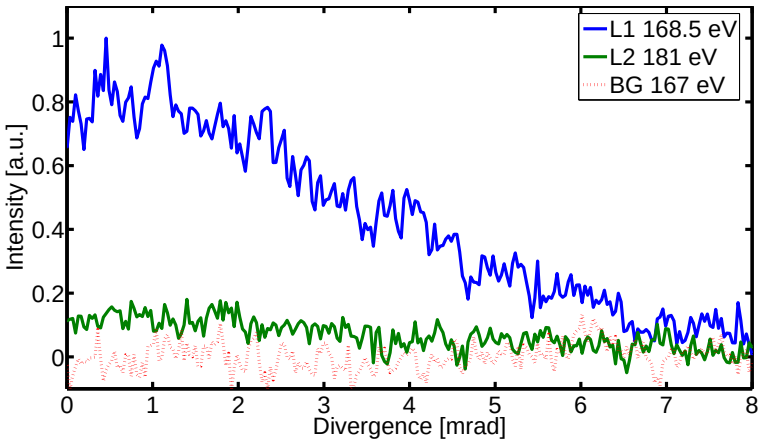

Figure 4.6: The spatial profile of the two laser lines and the background recorded in the spectrometer exhibits a divergence of $\sim$ 6 mrad FWHM for the full SXRL beam at 168.5 eV in the vertical dimension.

The vertical divergence of the SXRL was determined to be $\sim$ 6 mrad FWHM, as shown in Fig. 4.6. The divergence, which was smaller than vertical divergence of 10 mrad for longer wavelength DGRIP soft x-ray lasers, could be explained by the reduced refraction effects at the shorter wavelength, and the narrower gain zone for this laser.

The absolute output energy of the soft x-ray laser was determined by the integration of the background corrected counts of the lasing line on the back-illuminated CCD

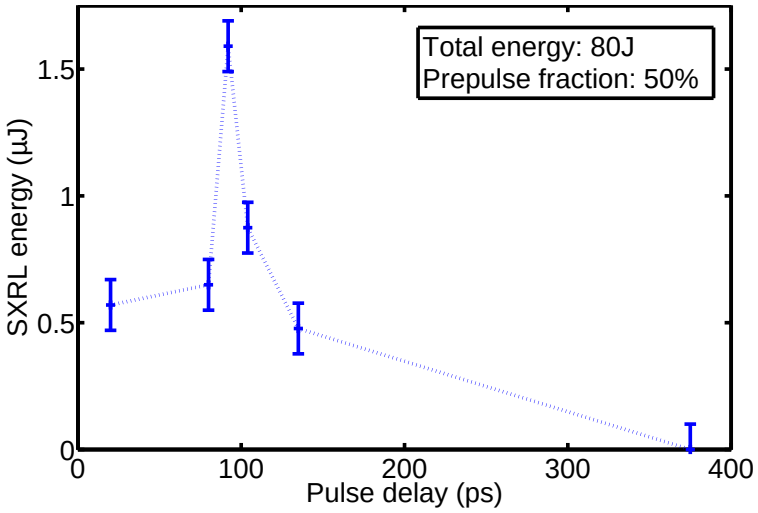

Figure 4.7: The scan of the double-pulse delay shows a maximum SXRL output for 90 ps with a FWHM of 50 ps.

camera. Here, an ANDOR CCD camera was used with a quantum efficiency Q_{CCD} of 0.325 for 7.36 nm radiation. One had also to consider that the multi-electron generation depended on the photon energy of the SXRL E_{ph}, being a multiple of the band gap of the Si transition E_{Si} of 3.45 eV. The absolute photon number C_{real} determined by the counts on the camera C_{CCD} was then calculated as

$$C_{real} = \frac{C_{CCD}}{Q_{CCD}} / \frac{E_{ph}}{E_{Si}}. \tag{4.3}$$

The highest obtained SXRL energy was determined to be $\sim 1.6\,\mu$J with respect to the solid angle of the spectrometer, the reflectivity of the gold grating and the fused silica substrate and the transmission values of the carbon filters. The obtained SXRL energy was in agreement with the modelling in (KPM$^+$01).

By changing the delay in the Mach-Zehnder set-up, the dependence of the SXRL output on the delay in the double-pulse was studied. For this series, the total pump energy was kept constant at ~ 80 J with $\sim 50\%$ in the pre-pulse and the delay was varied from 20 ps to 375 ps. The maximum SXRL output was found at 90 ps with a FWHM of 50 ps (Fig. 4.7). The small time delay and its narrow window were alluded to fast changes in the hydrodynamics of the pre-plasma (Per06). The optimum agrees with the results of (KPM$^+$01), in which an optimal delay of 130 ps was obtained.

The effect of the double-pulse energy ratio was studied with a total pump energy of ~ 100 J and a double-pulse delay of ~ 80 ps. The SXRL output increased by

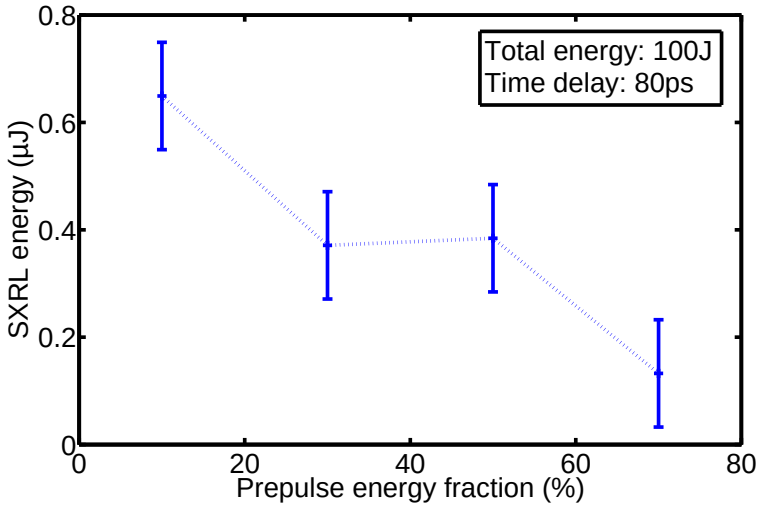

Figure 4.8: The scan of the double-pulse energy ratio shows an increase of the SXRL output with smaller pre-pulse energy fractions.

factor of 5 with the variation of the pre-pulse energy fraction from 70% to 10%. This showed the strong influence of the pre-pulse energy on the SXRL emission, indicating a maximum at a lower pre-pulse energies towards $\sim$ 10 J (Fig. 4.8). The experimental estimation of a total pump energy threshold was done by reducing the total pump energy from 85 J down to 36 J. In this case the pre-pulse energy fraction was kept constant at $\sim$ 50% and the delay of the double-pulse was $\sim$ 120 ps. Under these conditions the SXRL output increased by a factor of 3 with the reduction of the energy from 85 J to 42 J, where the maximum was found. This showed that a pre-pulse energy of $\sim$ 20 J creates a suitable pre-plasma condition for this configuration. Reducing the total pump energy to 36 J, SXRL emission was still observed. At this pump energy the observed emission was 5 times weaker compared to the maximum. The increase of the SXRL output with lower pump energy might have been caused by the smaller pre-pulse energy amount, confirming the pre-pulse energy ratio scan in (Fig. 4.9).

4.1.3 Conclusion

The application of DGRIP proves also to be a simple and efficient method for the generation of short wavelength soft x-ray lasers. Ni-like Sm soft x-ray lasing at 7.36 nm was achieved at a low total pump energy threshold of 36 J, a value predicted by simulations of (Per06), and half the total pump energy applied by

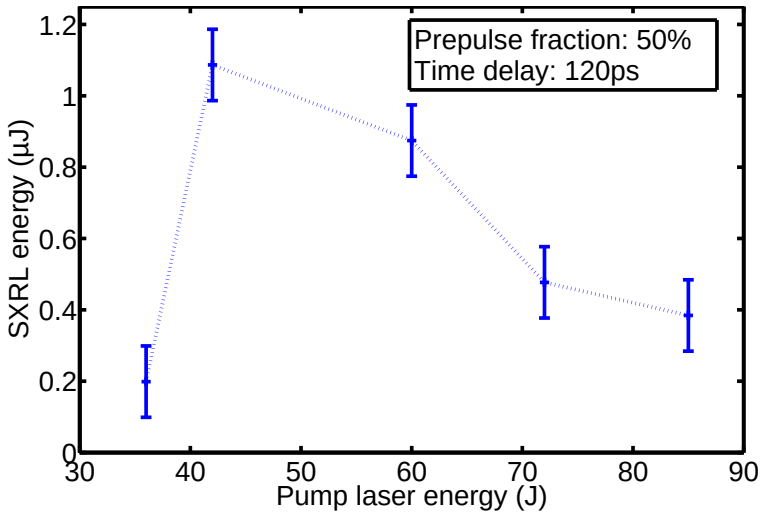

Figure 4.9: The scan of the total pump laser energy identifies the pump threshold of 36 J and the optimum at 42 J.

(KPM+01). This confirms the advantages of the applied pumping scheme for the photon energy region close to 200 eV. The efficiency of the soft x-ray laser generation in the experiment presented here is $\sim 4 \times 10^{-8}$, which is not comparable with SXRL operation above 10 nm. A reliable and stable SXRL operation is observed, due to the DGRIP characteristics. The generation of the double-pulse is controlled in the front-end and applied for high energy double-pulses up to 150 J without any restrains. With the single-beam single-focusing geometry the adjustment is fast and stable. The capability to produce a line focus with an excellent homogeneity and optimized dimensions at pump laser energies up to 150 J is demonstrated. The tuning of the pulse front tilt to match the traveling-wave speed along the line focus by the turning of the compressor grating is straightforward and precisely controlled with a novel autocorrelation mechanism using short double-pulses from the Mach-Zehnder. The gain in reproducibility and efficiency as compared to other experiments at high pump laser energies, which were based on two separated beams, plus the guaranteed exact spatial overlap of the two pump pulses, proves to be the major advancement for the development of short wavelength soft x-ray lasers.

4.2 DGRIP for applications

The implementation of the DGRIP scheme at the high repetition rate laser facility LASERIX allowed for irradiation experiments with user supplied materials. The capability to deliver continuously high photon doses onto user samples in a stable operation running automatically over exposure times of several hours, was an achievement of the DGRIP scheme. The long-term operation and performance characteristics of the DGRIP SXRL are described in this section, which were of great importance for the experiment planning of users.

4.2.1 Near- and far-field characterization

The real-time evolution of the SXRL output and source position is presented in Fig. 4.10. An operation at constant SXRL energy was possible over at least 200 shots on the same target position before the energy decreased almost linearly with the number of shots down to 40% of the initial value for the 300th shot. The long output energy stability was the result of using very low energetic pre-pulse arriving several nanoseconds before the pump laser double-pulse. In the absence of this pre-pulse, less than 100 shots could be performed on the same target position. The pre-pulse was generated by changing the timing of a Pockels cell in the laser front-end. The shot-to-shot energy fluctuations were of the order of 20%, but if one compared the dose accumulations for 200 shots, the integrated dose fluctuations were limited to less than 5%. The latter consideration appeared to be the most relevant for users requiring accumulation of photons.

The position of the SXRL source fluctuated in the order of a few microns in the vertical direction due to pointing instabilities of the pump laser. The slow monotonic movement in the horizontal position was caused by the ablation of the target material for each shot. The source position change towards the target was about 0.25 μm per shot. The average SXRL energy at the exit of the source was about 1 μJ per pulse for a series of 200 shots, corresponding to an average soft x-ray laser power of 10 μW for the long-term operation.

A reproducible drift of soft x-ray laser pointing was observed during a sequence of shots performed on the same target position. This drift was in the horizontal direction, towards higher refractive angles, corresponding to approximately 3 mrad for a 200-shot series on the same target position. The origin of the effect might

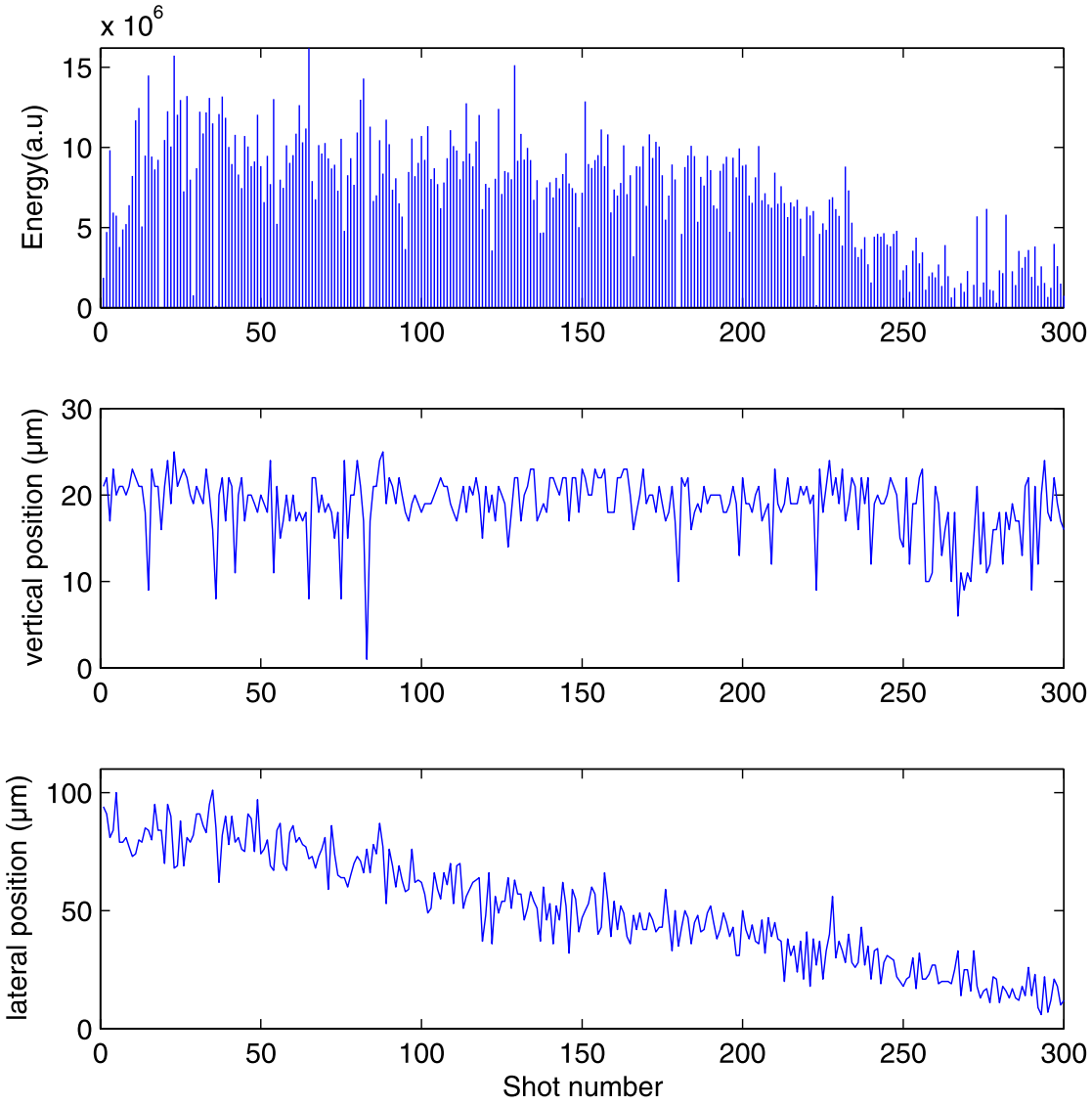

Figure 4.10: The figure shows the integrated SXRL energy and the relative positions of the SXRL source in vertical and lateral dimensions, respectively, as a function of the SXRL shot number for the same target position ($ZZH^{+}10$).

have been caused by inhomogeneous digging of the target groove due to the lower laser intensity at the line focus edges or from increased refraction due to higher electron density gradients in the plasma. Experimentally it was compensated by automatically turning the target holder with an angular speed of 8×10^{-3} degrees per second. In our experimental configuration, this effect was not critical due to the short distance to the interaction chamber and the irradiation close to the source image plane.

4.2.2 Target consideration

Continuous SXRL operation was achieved by vertically translating the target by an amount of 200 μm every 200 shots maintaining the high SXRL output energy. Smaller translations were also investigated but appeared to be inefficient for the lasing. As the target height of 5 cm was limiting the total length of the translation stage, the maximum number of shots per target was 50.000, corresponding to 250 target craters and a total acquisition time slightly longer than one hour. This kind of operation was successful due to the robustness of the DGRIP scheme against pump laser fluctuations. The target longevity could be related to the specific hardness and high melting point of molybdenum and might have been different for other SXRL materials. Replacing an old target by a fresh one by vacuum break and re-pumping took only 10 minutes and did not require any re-alignment of the pump laser beam. Fig. 4.11 presents a photograph of a used target, showing the periodic craters. The very simple rectangular shape of the target as compared to the proposition of a helicoidal shape (WLW$^+$06), allowed the recycling of used molybdenum pieces by milling them after irradiation. No loss in efficiency was observed using this fast, simple and cost-efficient technique. Despite the very high number of laser shots inside the chamber, we did not observe severe problems of optics pollution by the molybdenum plasma plume or damages from target debris. This was a common problem in the GRIP scheme, using a lens close to the target for the pre-pulse beam focusing, which is dispensable in the DGRIP geometry.
The total SXRL energy accumulated for one completely used target slab reached $\sim$ 50 mJ in 80 minutes, but it is expected to be increased to by further optimization of the shot number per target position. The average energy deposition per hour of the DGRIP SXRL was even higher than the QSS SXRLs with pulse energies of 4 mJ every 20 minutes (RMP$^+$02). So the DRIP operation is especially appealing for irradiation experiments of samples well standing vacuum exposure.

4.2.3 Irradiation of samples

The application chamber was placed 1.5 m away from the SXRL source. After a pre-filtering of visible and harder x-ray emission from the plasma by a 150 nm Al filter, the SXRL beam was guided onto a one-inch spherical mirror with multilayer Mo:Si surface that induced an additional filtering of the SXRL wavelength. The

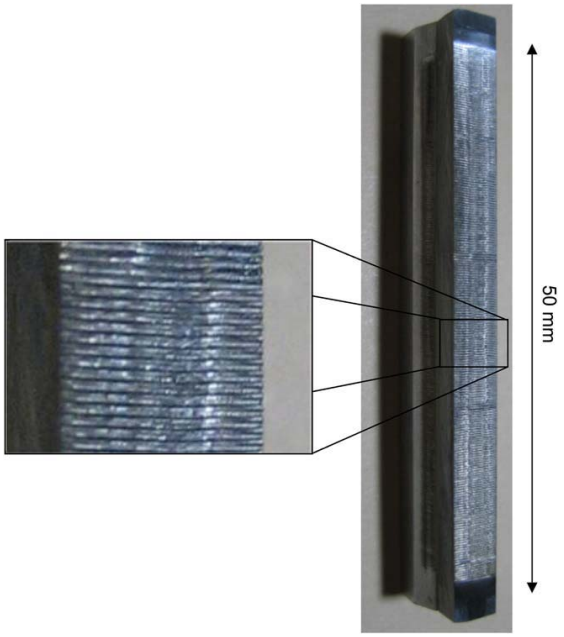

Figure 4.11: The nickel-like molybdenum SXRL target with a height of 50 mm shows grooves for each line focus position on the target. After $\sim$ 50000 shots the target is completely structured and has to be exchanged (ZZH$^+$10).

mirror aperture was sufficient to collect the full beam with respect to its relatively high vertical divergence. A 200 nJ SXRL energy per shot on-sample was measured at 18.9 nm with a calibrated SXR photo diode connected to a synchronized pico-amperemeter. This was in good agreement with the cross-calibration of the energy inferred at the source from the near-field diagnostic, with respect to the mirror reflectivity and the filter transmission.

To irradiate the sample of 3 mm diameter, required to work with a collimated SXRL beam to fully control the irradiation spot size by translating the target holder along the propagation axis around the focus position. The control of the spot profile was done with a CCD camera near the focus, to match the spot to the sample sizes. The spatial homogeneity of the dose deposition on the samples was realized despite the intrinsic speckle structure of the SXRL beam (GKC$^+$06). As the speckles were random, the position of the maxima in intensity for each single shot was changed from one shot to shot and smeared out to $\frac{1}{\sqrt{N}}$, with N as number of shots.

The automatic target movement was software controlled together with the laser shot sequences. For each shot, the actual SXRL energy was recorded and the total

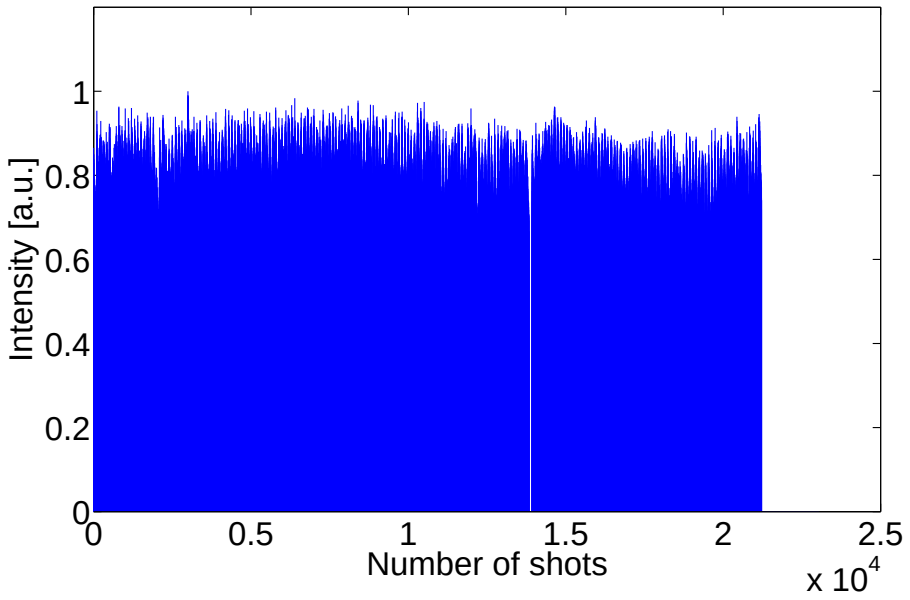

Figure 4.12: The photo current on a Mo:Si SXRL mirror is recorded for a sequence of 21000 shots to demonstrate the long time stability of the SXRL output energy.

energy deposited on the sample was deduced from the integrated photo current produced by the SXRL reflection on the focusing Mo:Si mirror and measured with a pico-amperemeter (Fig. 4.12). The graph shows the good stability of the energy deposition over more than 20.000 shots. With the real-time energy measurement, the system was able to start the laser, proceed to the sequence of shots, translate the target, and to stop the irradiation when the required dose on target was reached.

4.2.4 Conclusion

The successful installation of the DGRIP SXRL at the facility LASERIX opened the way to apply the source in the fields of irradiation experiments. A first application was the irradiation of DNA samples to identify the physical mechanisms underlying the formation of DNA lesions induced by ionizing SXR radiation and the biological response (CRK$^+$05). During the experiment the stable and reliable operation of DGRIP was demonstrated for more than one hour, corresponding to a few ten thousand shots. The spatial and temporal energy deposition was very homogeneous and did not fluctuate by more than 5%. A total integrated energy of up to 50 mJ at 18.9 nm was deposited on user samples. This application proved the attractiveness of the DGRIP SXRL as a valuable tool for research.

Chapter 5

Conclusion and Outlook

5.1 Conclusion

In this work, a new double laser-pulse pumping scheme for transient collisionally excited soft x-ray lasers was developed, characterized and utilized for applications. Using this concept, efficient SXRL operation from $\sim 50\,\mathrm{eV}$ up to $\sim 200\,\mathrm{eV}$ was demonstrated. With the implementation of a specially developed Mach-Zehnder unit in the CPA laser front-end, the generation of fully controllable double-pulses was accomplished and applied to optimally pump SXRLs and additionally to evaluate the amount of nonlinear effects in the CPA laser system.

The fully configurable Mach-Zehnder allowed for the creation of two pulses of different pulse duration and variable energy balance with an adjustable time delay. As an application of the double-pulse configuration, besides the SXRL pumping, the B-integral in the CPA laser system was measured by amplifying short pulse replica in the system, followed by an analysis in the time domain. This method was applied at two independent CPA laser systems exhibiting distinctively different laser parameters. The measurement of B-integral values in the 0.1 to 1.5 radian range, only limited by the reachable laser parameters, proved to be a precise tool to characterize nonlinear effects in the laser systems and it is expected to extend the attainable measurement range starting from as low as 20 mrad to several radians. The creation of a pulse train of equally spaced pulses will be of interest not only for the characterization of the laser system itself, but also for pump-probe experiments where a strobe detection scheme is necessary.

Contributing to the issue of SXRL pumping, the double-pulse was configured to optimally generate the gain medium of the SXRL amplification. The focusing geometry of the two collinear pulses under the same grazing incidence angle on the target, significantly improved the generation of the active plasma medium. On one hand the effect was induced by the intrinsically guaranteed exact overlap of the two pulses on the target, and on the other hand by the grazing incidence pre-pulse plasma generation, which allows for a SXRL operation at higher electron densities, enabling higher gain in longer wavelength SXRLs and higher efficiency at shorter wavelength SXRLs. The observation of gain enhancement was confirmed by plasma hydrodynamic simulations.

The first introduction of double short-pulse single-beam grazing incidence pumping for SXRL pumping below 20 nm resulted in a reliable operation of a Ni-like palladium SXRL at 14.7 nm with a pump energy threshold strongly reduced to less than 500 mJ. With the adaptation of the concept, namely double-pulse single-beam grazing incidence pumping (DGRIP), an improved efficiency and stability of table-top high-repetition soft x-ray lasers in the wavelength region below 20 nm was demonstrated. 2 μJ of Ni-like molybdenum soft x-ray laser emission at 18.9 nm with a total pump laser energy below 1 J on the target was obtained at 10 Hz repetition rate without re-alignment, proving the attractiveness for high average power operation. On one hand the low costs and the easy and rapid alignment procedure fulfilled the requirements for a sophisticated installation, and on the other hand the highly stable output satisfied the need for a reliable strong SXRL source. The qualities of the DGRIP scheme were confirmed in an application experiment with over fifty thousand shots and a deposited energy of $\sim$ 50 mJ on user samples.

The generation of double-pulses with high energies of up to 120 J enabled the transfer to shorter wavelength SXRL operation. The application of DGRIP proved also here to be a simple and efficient method for the generation of soft x-ray lasers below 10 nm. Ni-like samarium soft x-ray lasing at 7.3 nm was achieved at a low total pump energy threshold of 36 J, which confirmed the suitability of the applied pumping scheme. A reliable and stable SXRL operation was demonstrated, due to the single-beam pumping geometry.

The generation of the Ni-like Sm x-ray laser was an important milestone for the feasibility of applying the pumping scheme also for higher pumping pulse energies, which are necessary to obtain soft x-ray laser wavelengths in the water window. The reduction of the total pump energy below 40 J for 7.3 nm lasing fulfilled the requirement for the implementation at high-repetition rate operation facilities.

5.2 Outlook

5.2.1 Short-wavelength soft x-ray lasers

A number of applications, including imaging of biological specimen and diagnostics of dense plasmas, require soft x-ray lasers with short wavelength. In medical and biological research, especially attractive is the possibility to reach into the water-window, in which the carbon absorbs well soft x-ray radiation, while the water is quasi transparent. In this configuration high contrast imaging of carbon structures in water is possible.

To achieve such short wavelength SXRLs in the transient collisional scheme requires high Z materials, ionized to Ni-like states and in addition a high electron temperature to sufficiently produce a population inversion. These requirements demand a sophisticated pumping geometry. With the development of DGRIP for short wavelengths a first step towards this aim has been achieved. The generation of the Ni-like Sm SXRL was an important milestone for the feasibility of applying the DGRIP scheme for higher pumping pulse energies, which are necessary to obtain soft x-ray lasing in the above-mentioned water window (Per06),(Per07a),(Per07b). Together with the planned capability of the laser facility PHELIX to bring up to 250 J double-pulse pump laser energy on the target, a Ni-like tungsten x-ray laser at 4.32 nm in the desired water window is conceivable.

However, to establish soft x-ray lasing in such short wavelengths ranges, a frequency doubling of high energy CPA laser pulses could be beneficial. A more efficient laser light absorption and an energy deposition in higher electron densities could be achieved in this way, increasing the gain of short wavelength soft x-ray lasers. Additionally the use of nano-structured targets promises tremendous advantages for the creation of the soft x-ray amplifier medium. If the irradiated target has a volume density, which even in the case of Ni-like ionization provides an electron density lower than the critical one, near volumetric heating and ionization of the target material is possible. Foam targets are promising targets for soft x-ray laser amplification due to the higher efficiency of the laser energy conversion into bulk electron temperature, and smoothing of the laser focal spot inhomogeneities. All these efforts together will probably contribute to an efficient generation of such highly desired soft x-ray lasers in the water window at the laser facility PHELIX.

For the development of high repetition rate short wavelength SXRL another milestone has been achieved. The reduction of the total pump energy below 40 J for lasing around 7 nm in the DGRIP scheme now enables its implementation at the high-repetition rate routine operation at the facility LASERIX. This allows for the further optimization of the Ni-like Sm SXRL pump parameters, as it was done extensively for Ni-like Mo at 18.9 nm. Such a study could enhance the SXRL output energy dramatically and establish sub 10 nm SXRLs in the field of applicable SXRL sources. The possibility to expand the wavelength range for high-repetition-rate SXRL operation, is highly desired for various irradation experiments e.g. (CRK$^+$05).

5.2.2 High-energy soft x-ray lasers

Transient collisionally excited soft x-ray lasers have the potential to generate high-energy, short-pulse beams. Due to their high electron density plasmas, they can store the highest amount of energy among all plasma amplifiers. The available energy is proportional to the small-signal gain coefficient, the saturation fluence and the active volume. Since both the saturation fluence and the gain coefficient are high, the amount of the stored energy is huge. Due to the amplified spontaneous emission mechanism the energy extraction does not reach the highest efficiency. To avoid this limitation, the principle of a soft x-ray master oscillator - power amplifier

concept was developed (DCN$^+$95), as it is common practice in visible lasers.

The idea is to seed the soft x-ray amplifier with a coherent source, e.g. high order harmonics. The first successful attempt was realized by (ZFS$^+$04) with high order harmonics injected into an OFI-SXRL at 32.8 nm. Later the method was adopted by (WGL$^+$06) to a seeded GRIP SXRL by injecting harmonics into the Ni-like Ag amplifier at 13.9 nm. The gain factor in this configuration was very large with over 400 and accompanied by an extreme improvement of the spatial coherence and reduction in divergence. Together with the development of efficient soft x-ray amplifiers like DGRIP, the injected amplifier concept shows a huge potential for upcoming applications (HSA$^+$10).

However, to date, the output energy from solid amplifiers remains as low as $\sim 2\mu$J, in seeded operation even less than 100 nJ (WGP$^+$08). Careful tailoring of the plasma shape is crucial for extracting the energy stored in the plasma amplifier. With larger plasma widths, tens of microjoules of soft x-ray laser energy in picosecond pulses are predicted. With such tailored plasmas, gain and pumping efficiency are expected to increase by nearly a factor of 10 as compared to the narrower plasma amplifiers studied here (OZS$^+$09).

To improve the total output energy of soft x-ray lasers in this way, shaped line foci seem to be promising tools. Sophisticated line focus shapes provide an increased homogeneity of the plasma gain zone at large line widths and thereby the potential of high soft x-ray laser output energy. The idea is to install designed apertures to shape the top-hat pump laser beam, which is then focused to a line focus with the required dimensions. The aperture shapes are calculated with the ray tracing software ZEMAX, and have to be adapted to the beam path specifications of the operating laser system. With this method, rectangular line foci with large widths are produced, which cannot be achieved by defocusing. The losses associated with such apertures in the laser system are of negligible amount since the shaping is performed in the front-end. Designed apertures for the initial beam profile at the laser facility PHELIX can produce a line focus of 6 mm length and 300 μm width, promising a soft x-ray laser output of up to 100 μJ. These high photon numbers are highly desired for diagnostics of warm dense matter, like Thomson scattering for

electron density and temperature determination.

5.2.3 High average power soft x-ray lasers

The enhancement of the average power of soft x-ray lasers has always been desired by various applications. The aim to increase the average power of soft x-ray lasers can be achieved by an upgrade of the pump laser system to higher repetition rates. Diode-pumped solid-state laser systems are capable of delivering repetition rates up to 100 Hz and being at the same time more compact than equivalent flash lamp-pumped systems (TJS$^+$09). Soft x-ray laser operation at such high repetition rates can deliver an average power of up to 200 μW. Such a high repetition rate operation requires a reliable and highly stable pumping geometry.

The DGRIP geometry could provide a sophisticated solution for this kind of SXRL operation. With its concept of collinear pump laser double-pulses under grazing incidence, the SXRL is not as susceptible to pump laser instabilities, and at the same time, provides stable, high-energy output. A first step towards high average power SXRL operation has already been made by (FRL$^+$09), where an all-diode-pumped Yb:YAG laser in a geometry similar to DGRIP was applied to pump a 18.9 nm SXRL at 10 Hz. The results obtained so far are already promising, confirming the observed advantages of the DGRIP scheme. It is planned to upgrade the operation to 100 Hz soon, resulting in the highest average power SXRL operation ever by applying the DGRIP scheme.

Appendix A

An improved double-pulse non-normal incidence pumping geometry for transient collisionally excited soft X-ray lasers

Appendix B

Optimization of a tabletop high-repetition-rate soft x-ray laser pumped in double-pulse single-beam grazing incidence

Appendix C

Short-wavelength soft-x-ray laser pumped in double-pulse single-beam non-normal incidence

Appendix D

Stable and fully controlled long-time operation of a soft x-ray laser for user application experiments

Appendix E

X-ray Parametric Amplification (XPA)

Complementary to the developments of plasma soft x-ray lasers, a new method for parametric amplification of soft x-ray radiation, namely X-ray Parametric Amplification (XPA), was discovered within a collaboration with the Friedrich-Schiller-University of Jena (SSH$^+$10). This new type of soft x-ray laser generation has the potential to be a complementary source next to high-order harmonics and plasma soft x-ray lasers.

Bibliography

[AAA+07] W. Ackermann, G. Asova, V. Ayvazyan, A. Azima, N. Baboi, J. Bahr, V. Balandin, B. Beutner, A. Brandt, A. Bolzmann, R. Brinkmann, O. Brovko, M. Castellano, P. Castro, L. Catani, E. Chiadroni, S. Choroba, A. Cianchi, J. Costello, D. Cubaynes, J. Dardis, W. Decking, H. Delsim-Hashemi, A. Delserieys, G. Pirro, M. Dohlus, S. Dusterer, A. Eckhardt, H. Edwards, B. Faatz, J. Feldhaus, K. Flottmann, J. Frisch, L. Frohlich, T. Garvey, U. Gensch, Ch. Gerth, M. Gorler, N. Golubeva, H.-J. Grabosch, M. Grecki, O. Grimm, K. Hacker, U. Hahn, J. Han, K. Honkavaara, T. Hott, M. Huning, Y. Ivanisenko, E. Jaeschke, W. Jalmuzna, T. Jezynski, R. Kammering, V. Katalev, K. Kavanagh, E. Kennedy, S. Khodyachykh, K. Klose, V. Kocharyan, M. Korfer, M. Kollewe, W. Koprek, S. Korepanov, D. Kostin, M. Krassilnikov, G. Kube, M. Kuhlmann, C. L. Lewis, L. Lilje, T. Limberg, D. Lipka, F. Lohl, H. Luna, M. Luong, M. Martins, M. Meyer, P. Michelato, V. Miltchev, W. Moller, L. Monaco, W. F. Muller, O. Napieralski, O. Napoly, P. Nicolosi, D. Nolle, T. Nunez, A. Oppelt, C. Pagani, R. Paparella, N. Pchalek, J. Pedregosa-Gutierrez, B. Petersen, B. Petrosyan, G. Petrosyan, L. Petrosyan, J. Pfluger, E. Plonjes, L. Poletto, K. Pozniak, E. Prat, D. Proch, P. Pucyk, P. Radcliffe, H. Redlin, K. Rehlich, M. Richter, M. Roehrs, J. Roensch, R. Romaniuk, M. Ross, J. Rossbach, V. Rybnikov, M. Sachwitz, E. Saldin, W. Sandner, H. Schlarb, B. Schmidt, M. Schmitz, P. Schmuser, J. Schneider, E. Schneidmiller, S. Schnepp, S. Schreiber, M. Seidel, D. Sertore, A. Shabunov, C. Simon, S. Simrock, E. Sombrowski, A. Sorokin, P. Spanknebel, R. Spesyvtsev, L. Staykov, B. Steffen, F. Stephan, F. Stulle, H. Thom, K. Tiedtke, M. Tischer,

S. Toleikis, R. Treusch, D. Trines, I. Tsakov, E. Vogel, T. Weiland, H. Weise, M. Wellhofer, M. Wendt, I. Will, A. Winter, K. Wittenburg, W. Wurth, P. Yeates, M. Yurkov, I. Zagorodnov, and K. Zapfe. Operation of a free-electron laser from the extreme ultraviolet to the water window. *Nat Photon*, 1(6):336–342, June 2007.

[AATE+03] Y. Abou-Ali, G.J. Tallents, M. Edwards, R.E. King, G.J. Pert, S.J. Pestehe, F. Strati, R. Keenan, C.L.S. Lewis, S. Topping, O. Guilbaud, A. Klisnick, D. Ros, R. Clarke, D. Neely, M. Notley, and A. Demir. Measurement of the duration of x-ray lasing pumped by an optical laser pulse of picosecond duration. *Optics Communications*, 215:397–406, 2003.

[AMW+10] D. Alessi, D. H. Martz, Y. Wang, M. Berrill, B. M. Luther, and J. J. Rocca. Gain-saturated 10.9 nm tabletop laser operating at 1 hz repetition rate. *Opt. Lett.*, 35(3):414–416, 2010.

[BAB+09] V. Bagnoud, B. Aurand, A. Blazevic, S. Borneis, C. Bruske, B. Ecker, U. Eisenbarth, J. Fils, A. Frank, E. Gaul, S. Goette, C. Haefner, T. Hahn, K. Harres, H.-M. Heuck, D. Hochhaus, D. Hoffmann, D. JavorkovÃ¡, H.-J. Kluge, T. Kuehl, S. Kunzer, M. Kreutz, T. Merz-Mantwill, P. Neumayer, E. Onkels, D. Reemts, O. Rosmej, M. Roth, T. Stoehlker, A. Tauschwitz, B. Zielbauer, D. Zimmer, and K. Witte. Commissioning and early experiments of the phelix facility. *Applied Physics B: Lasers and Optics*, pages –, 2009.

[BBB+09] V Bagnoud, A Blazevic, S Borneis, U Eisenbarth, J Fils, S Goette, Th Kuehl, E Onkels, T Stoehlker, A Tauschwitz, D Zimmer, and K Witte. Phelix: A petawatt-class laser recently commissioned for experiments in plasma and atomic physics. *Journal of Physics: Conference Series*, 194(15):152028, 2009.

[BBW+08] Courtney A. Brewer, Fernando Brizuela, Przemyslaw Wachulak, Dale H. Martz, Weilun Chao, Erik H. Anderson, David T. Attwood, Alexander V. Vinogradov, Igor A. Artyukov, Alexander G. Ponomareko, Valeriy V. Kondratenko, Mario C. Marconi, Jorge J. Rocca, and Carmen S. Menoni. Single-shot extreme ultraviolet laser imaging

of nanostructures with wavelength resolution. *Opt. Lett.*, 33(5):518–520, 2008.

[BGIS07] J.E. Balmer, M. Grünig, C. Imesch, and F. Staub. X-ray lasing using the grip scheme, 2007.

[BMBR97] B. R. Benware, C. H. Moreno, D. J. Burd, and J. J. Rocca. Operation and output pulse characteristics of an extremely compact capillary-discharge tabletop soft-x-ray laser. *Opt. Lett.*, 22(11):796–798, 1997.

[BWB+09] F. Brizuela, Y. Wang, C. A. Brewer, F. Pedaci, W. Chao, E. H. Anderson, Y. Liu, K. A. Goldberg, P. Naulleau, P. Wachulak, M. C. Marconi, D. T. Attwood, J. J. Rocca, and C. S. Menoni. Microscopy of extreme ultraviolet lithography masks with 13.2 nm tabletop laser illumination. *Opt. Lett.*, 34(3):271–273, 2009.

[BZEK09a] V. Bagnoud, D. Zimmer, B. Ecker, and T. Kuehl. A technique for measuring b-integral in chirped-pulse amplifiers. In *Lasers and Electro-Optics, 2009 and 2009 Conference on Quantum electronics and Laser Science Conference. CLEO/QELS 2009.*, 2009.

[BZEK09b] Vincent Bagnoud, Daniel Zimmer, Boris Ecker, and Thomas Kuehl. A technique for measuring b-integral in chirped-pulse amplifiers. In *Conference on Lasers and Electro-Optics/International Quantum Electronics Conference*, page CFG4. Optical Society of America, 2009.

[BZEK10] V. Bagnoud, D. Zimmer, B. Ecker, and T. Kuehl. A technique for measuring b-integral in chirped-pulse amplifiers. *Optics Express*, submitted, 2010.

[CKR+07] K. Cassou, S. Kazamias, D. Ros, F. Plé, G. Jamelot, A. Klisnick, O. Lundh, F. Lindau, A. Persson, C.-G. Wahlström, S. de Rossi, D. Joyeux, B. Zielbauer, D. Ursescu, and T. Kühl. Optimization toward a high-average-brightness soft-x-ray laser pumped at grazing incidence. *Opt. Lett.*, 32(2):139–141, 2007.

[Cor93] P. B. Corkum. Plasma perspective on strong field multiphoton ionization. *Phys. Rev. Lett.*, 71(13):1994–, September 1993.

[CRK+05] K. Cassou, D. Ros, S. Kazamias, A. Klisnick, G. Jamelot, O. Guilbaud, B. Rus, M. Kozlova, J. Polan, A.R. Praeg, M. Stupka, G. Eot-Houllier, E. Sage, M. Begusova, V. Stisova, M.-A.H. du Penhoat, A. Touati, and A. Chetioui. Etude des dommages induits dans l'adn par irradiation laser x-uv a 21.2 nm. *J. Phys. IV France*, 127:177–180, jun 2005.

[CSS+00] Jean-Christophe Chanteloup, Estelle Salmon, Christian Sauteret, Arnold Migus, Philippe Zeitoun, Annie Klisnick, Antoine Carillon, Stéphane Hubert, David Ros, Peter Nickles, and Mikhail Kalachnikov. Pulse-front control of 15-tw pulses with a tilted compressor, and application to the subpicosecond traveling-wave pumping of a soft-x-ray laser. *J. Opt. Soc. Am. B*, 17(1):151–157, 2000.

[DCN+95] T. Ditmire, J. K. Crane, H. Nguyen, L. B. DaSilva, and M. D. Perry. Energy-yield and conversion-efficiency measurements of high-order harmonic radiation. *Phys. Rev. A*, 51(2):R902–, February 1995.

[DKM+95] H. Daido, Y. Kato, K. Murai, S. Ninomiya, R. Kodama, G. Yuan, Y. Oshikane, M. Takagi, H. Takabe, and F. Koike. Efficient soft x-ray lasing at 6 to 8 nm with nickel-like lanthanide ions. *Phys. Rev. Lett.*, 75(6):1074–, August 1995.

[DLO+00] J. Dunn, Y. Li, A. L. Osterheld, J. Nilsen, J. R. Hunter, and V. N. Shlyaptsev. Gain saturation regime for laser-driven tabletop, transient ni-like ion x-ray lasers. *Phys. Rev. Lett.*, 84(21):4834–, May 2000.

[DOS+98] J. Dunn, A. L. Osterheld, R. Shepherd, W. E. White, V. N. Shlyaptsev, and R. E. Stewart. Demonstration of x-ray amplification in transient gain nickel-like palladium scheme. *Phys. Rev. Lett.*, 80(13):2825–, March 1998.

[DSTB+92] LB Da Silva, JE Trebes, R Balhorn, S Mrowka, E Anderson, DT Attwood, Jr Barbee, TW, J Brase, M Corzett, J Gray, and al. et. X-ray laser microscopy of rat sperm nuclei. *Science*, 258(5080):269–271, 1992.

[Eck09] B. Ecker. Aufbau eines kompakten röntgenlasers. Master's thesis, Johannes Gutenberg-University Mainz, 2009.

[Emm09] P. Emma. First lasing of the lcls x-ray fel at 1.5 a. 2009.

[FRL+09] Federico J. Furch, Brendan A. Reagan, Bradley M. Luther, Alden H. Curtis, Shaun P. Meehan, and Jorge J. Rocca. Demonstration of an all-diode-pumped soft x-ray laser. *Opt. Lett.*, 34(21):3352–3354, 2009.

[GISB09] M. Grünig, C. Imesch, F. Staub, and J.E. Balmer. Saturated x-ray lasing in ni-like sn at 11.9 nm using the grip scheme. *Optics Communications*, 282(2):267–271, January 2009.

[GKC+06] O. Guilbaud, A. Klisnick, K. Cassou, S. Kazamias, D. Ros, G. Jamelot, D. Joyeux, and D. Phalippou. Origin of microstructures in picosecond x-ray laser beams. *EPL (Europhysics Letters)*, 74(5):823, 2006.

[Gri05] Griem. *Principles of Plasma Spectroscopy.* Cambridge University Press, 2005.

[GRK+09] O. Guilbaud, D. Ros, S. Kazamias, B. Zielbauer, J. Habib, M. Pittman, M. Farinet, D. Zimmer, T. Yu, A. Klisnick, F. de Dortan, S. Lacombe, E. Porcel, C. Le Sech, M.-A. du Penhoat, A. Touati, M. Marsi, and D. Joyeux. Recent progress on the laserix facility. volume 7451, page 74510T. SPIE, 2009.

[HP96] P B Holden and G J Pert. Long-wavelength, prepulsed driving as a means to greatly increase the gain in low- z ne-like xuv lasers, 1996.

[HSA+10] Daniel. C. Hochhaus, Jozsef Seres, Bastian Aurand, Boris Ecker, Bernhard Zielbauer, Daniel Zimmer, Christian Spielmann, and Thomas Kuehl. Tuning the high-order harmonic lines of a nd:glass laser for soft x-ray laser seeding. *Applied Physics B: Lasers and Optics*, 6650 B, 2010.

[JB07] D. Javorkova and V. Bagnoud. 60-db-dynamic-range short-pulse measurement from an 8-bit cmos camera. *Opt. Express*, 15(9):5439–5444, 2007.

[JCJ+99] G. Jamelot, A. Carillon, P. Jaegle, A. Klisnick, D. Ros, P. Zeitoun, P. Fourcade, S. Hubert, J. C. Lagron, L. Vanbostal, S. Sebban,

F. Albert, P. Agostini, D. Garzella, P. Breger, A. Belsky, I. Kamenskikh, D. Joyeux, D. Phalippou, M. Boussoukaya, A. Zeitoun-Fakiris, G. Lacheze-Murel, and E. Bechir. Usefulness of x-ray lasers for science and technology. *IEEE J. Quantum Electron.*, 5(6):1486, 1999.

[JTS+07] K. A. Janulewicz, J. Tummler, H. Stiel, W. Sandner, P.-V. Nickles, H.T. Kim, I.W. Choi, N. Hafz, J.H. Sung, T.J. Yu, K.-H. Hong, T.M. Jeong, D.-K. Ko, J Lee, I. J. Kim, and C. H. Nam. On the way towards a high repetition rate x-ray laser, 2007.

[KAB+09] Thomas Kuehl, Bastian Aurand, Vincent Bagnoud, Boris Ecker, Udo Eisenbarth, Jerome Fils, Daniel Hochhaus, Dasa Javorkova, Paul Neumayer, Bernhard Zielbauer, Daniel Zimmer, Jamil Habib, Sophie Kazamias, Annie Klisnick, David Ros, Josef Seres, Christian Spielmann, and Daniel Ursescu. X-ray laser developments at phelix. volume 7451, page 74510M. SPIE, 2009.

[KAB+10] T. Kuehl, B. Aurand, V. Bagnoud, B. Ecker, U. Eisenbarth, O. Guilbaud, J. Fils, S. Goette, J. Habib, D. Hochhaus, D. Javorkova, P. Neumayer, S. Kazamias, M. Pittman, D. Ros, J. Seres, Ch. Spielmann, B. Zielbauer, and D. Zimmer. Progress in the applicability of plasma x-ray lasers. *Hyperfine Interactions*, 196(1):233–241, February 2010.

[KBB+09] T. Kuehl, V. Bagnoud, C. Bruske, S. Borneis, B. Ecker, U. Eisenbarth, J. Fils, S. Goette, T. Hahn, D. Hochhaus, D. Javorkova, F. Knobloch, M. Kreutz, S. Kunzer, T. Merz-Mantwill, E. Onkels, D. Reemts, A. Tauschwitz, K. Witte, B. Zielbauer, and D. Zimmer. Versatile high-energy and short-pulse operation of phelix, 2009.

[KBSR97] M. A. Klosner, H. A. Bender, W. T. Silfvast, and J. J. Rocca. Intense plasma discharge source at 13.5 nm for extreme-ultraviolet lithography. *Opt. Lett.*, 22(1):34–36, 1997.

[KCR+06] S. Kazamias, K. Cassou, D. Ros, F. Plé, G. Jamelot, A. Klisnick, O. Lundh, F. Lindau, A. Persson, C.-G. Wahlström, S. de Rossi, D. Joyeux, B. Zielbauer, and D. Ursescu. Laser xuv haute cadence pompé par laser titane : Saphir, vers la station laserix. *J. Phys. IV France*, 138(1):13–19, dec 2006.

[KCR+08] S. Kazamias, K. Cassou, D. Ros, F. Plé, G. Jamelot, A. Klisnick, O. Lundh, F. Lindau, A. Persson, C.-G. Wahlström, S. de Rossi, D. Joyeux, B. Zielbauer, D. Ursescu, and T. Kühl. Characterization of a transient collisional ni-like molybdenum soft-x-ray laser pumped in grazing incidence. *Phys. Rev. A*, 77(3):033812–, March 2008.

[KDP+05] R. Keenan, J. Dunn, P. K. Patel, D. F. Price, R. F. Smith, and V. N. Shlyaptsev. High-repetition-rate grazing-incidence pumped x-ray laser operating at 18.9 nm. *Phys. Rev. Lett.*, 94(10):103901–, March 2005.

[KDS+03] Roisin Keenan, James Dunn, Vyacheslav N. Shlyaptsev, Raymond F. Smith, Pravesh K. Patel, and Dwight F. Price. Efficient pumping schemes for high average brightness collisional x-ray lasers. volume 5197, pages 213–220. SPIE, 2003.

[KGR+06] A. Klisnick, O. Guilbaud, D. Ros, K. Cassou, S. Kazamias, G. Jamelot, J.-C. Lagron, D. Joyeux, D. Phalippou, Y. Lechantre, M. Edwards, P. Mistry, and G.J. Tallents. Experimental study of the temporal coherence and spectral profile of the 13.9 nm transient x-ray laser. *Journal of Quantitative Spectroscopy and Radiative Transfer*, 99(1-3):370–380, May 2006.

[KJR+02] Annie Klisnick, Gerard Jamelot, David Ros, Antoine Carillon, Pierre Jaegle, Mustapha Boussoukaya, Olivier Guilbaud, Jaroslav Kuba, Raymond Smith, Jean-Claude Lagron, Laurent Vanbostal, Denis Joyeux, Daniel Phalippou, Stephane Sebban, Alain Touati, Marie Anne Herve du Penhoat, F. Ballester, E.-J. Petit, Bedrich Rus, Tomas Mocek, Federico Strati, Matthew Edwards, Gregory J. Tallents, Roisin Keenan, Simon Topping, Ciaran L. S. Lewis, Paul Neumeyer, Daniel Ursescu, Thomas Kuhl, Huajing Tang, and Hiroyuki Daido. Development and applications of x-ray lasers at lsai/lixam. volume 641, pages 166–173. AIP, 2002.

[KKC+08] H. T. Kim, C. M. Kim, I. W. Choi, N. Hafz, H. C. Kang, J. H. Sung, T. J. Yu, S. K. Lee, K.-H. Hong, T. M. Jeong, Y.-C. Noh, D.-K. Ko, J. Tümmler, P. V. Nickles, W. Sandner, K. A. Janulewicz, and

J. Lee. Characteristics of a ni-like silver x-ray laser pumped by a single profiled laser pulse. *J. Opt. Soc. Am. B*, 25(7):B76–B84, 2008.

[KKT+03] Tetsuya Kawachi, Masataka Kado, Momoko Tanaka, Noboru Hasegawa, Keisuke Nagashima, Kouta Sukegawa, Peixiang Lu, Kenjiro Takahashi, Sinichi Namba, Masato Koike, Akira Nagashima, and Yoshiaki Kato. Development of a pumping laser system for x-ray laser research. *Appl. Opt.*, 42(12):2198–2205, 2003.

[KLP+08] I Jong Kim, Gae Hwang Lee, Seung Beom Park, Yong Soo Lee, Tae Keun Kim, Chang Hee Nam, Tomas Mocek, and Krzysztof Jakubczak. Generation of submicrojoule high harmonics using a long gas jet in a two-color laser field. *Appl. Phys. Lett.*, 92(2):021125–3, January 2008.

[KPM+01] R. E. King, G. J. Pert, S. P. McCabe, P. A. Simms, A. G. MacPhee, C. L. S. Lewis, R. Keenan, R. M. N. ORourke, G. J. Tallents, S. J. Pestehe, F. Strati, D. Neely, and R. Allott. Saturated x-ray lasers at 196 and 73 a pumped by a picosecond traveling-wave excitation. *Phys. Rev. A*, 64(5):053810–, October 2001.

[KST+04] Tetsuya Kawachi, Akira Sasaki, Momoko Tanaka, Maki Kishimoto, Noboru Hasegawa, Keisuke Nagashima, Masato Koike, Hiroyuki Daido, and Yoshiaki Kato. Observation of strong soft-x-ray amplification at 8.8 nm in the transient collisional-excitation scheme. *Phys. Rev. A*, 69(3):033805–, March 2004.

[KUB+07a] T. Kuehl, D. Ursescu, V. Bagnoud, D. Javorkova, O. Rosmej, D. Zimmer, K. Cassou, S. Kazamias, A. Klisnick, D. Ros, B. Zielbauer, K. Janulewicz, P. Nickles, G. Pert, P. Neumayer, and J. Dunn. A non-normal incidence pumped ni-like zr xrl for spectroscopy of li-like heavy ions at gsi/fair, 2007.

[KUB+07b] Th. Kuehl, D. Ursescu, V. Bagnoud, D. Javorkova, O. Rosmej, K. Cassou, S. Kazamias, A. Klisnick, D. Ros, P. Nickles, B. Zielbauer, J. Dunn, P. Neumayer, G. Pert, and the PHELIX team null. Optimization of the non-normal incidence, transient pumped plasma x-

ray laser for laser spectroscopy and plasma diagnostics at the facility for antiproton and ion research (fair). *Laser and Particle Beams*, 25(01):93–97, 2007.

[LCJ95] L. Lepetit, G. Chériaux, and M. Joffre. Linear techniques of phase measurement by femtosecond spectral interferometry for applications in spectroscopy. *J. Opt. Soc. Am. B*, 12(12):2467–2474, 1995.

[LLP+07] F. Lindau, O. Lundh, A. Persson, K. Cassou, S. Kazamias, D. Ros, F. Plé, G. Jamelot, A. Klisnick, S. de Rossi, D. Joyeux, B. Zielbauer, D. Ursescu, T. Kühl, and C.-G. Wahlström. Quantitative study of 10 hz operation of a soft x-ray laser—energy stability and target considerations. *Opt. Express*, 15(15):9486–9493, 2007.

[LPSS74] Gary J. Linford, Eugene R. Peressini, Walter R. Sooy, and Mary L. Spaeth. Very long lasers. *Appl. Opt.*, 13(2):379–390, February 1974.

[LTM+99] J. Y. Lin, G. J. Tallents, A. G. MacPhee, A. Demir, C. L. S. Lewis, R. M. N. O'Rourke, G. J. Pert, D. Ros, and P. Zeitoun. Travelling wave chirped pulse amplified transient pumping for collisional excitation lasers. *Optics Communications*, 166(1-6):211–218, August 1999.

[LWL+05] B. M. Luther, Y. Wang, M. A. Larotonda, D. Alessi, M. Berrill, M. C. Marconi, J. J. Rocca, and V. N. Shlyaptsev. Saturated high-repetition-rate 18.9-nm tabletop laser in nickellikemolybdenum. *Opt. Lett.*, 30(2):165–167, January 2005.

[LWM+95] X. Liu, R. Wagner, A. Maksimchuk, E. Goodman, J. Workman, D. Umstadter, and A. Migus. Nonlinear temporal diffraction and frequency shifts resulting from pulse shaping in chirped-pulse amplification systems. *Opt. Lett.*, 20(10):1163–1165, 1995.

[MAHM+07] Majed Chergui Winfried Decking Barry Dobson Stefan Düsterer Gerhard Grübel Walter Graeff Heinz Graafsma Massimo Altarelli, Reinhard Brinkmann, Janos Hajdu, Jonathan Marangos, Joachim Pflüger, Harald Redlin, David Riley, Ian Robinson, Jörg Rossbach, Andreas Schwarz, Kai Tiedtke, Thomas Tschentscher, Ivan Vartaniants, Hubertus Wabnitz, Hans Weise, Riko Wichmann, Karl Witte, Andreas

Wolf, Michael Wulff, and Mikhail Yurkov. The european x-ray free-electron laser technical design report. Technical report, DESY, 2007.

[Mai60] T. H. Maiman. Stimulated optical radiation in ruby. *Nature*, 187(4736):493–494, August 1960.

[MAL+10] D. H. Martz, D. Alessi, B. M. Luther, Y. Wang, D. Kemp, M. Berrill, and J. J. Rocca. High-energy 13.9nm table-top soft-x-ray laser at 2.5hz repetition rate excited by a slab-pumped ti:sapphire laser. *Opt. Lett.*, 35(10):1632–1634, May 2010.

[Mar87] O. Martinez. Design of high-power ultrashort pulse amplifiers by expansion and recompression. *IEEE J. Quantum Electron.*, 23:1385, 1987.

[MBR99] C. D. Macchietto, B. R. Benware, and J. J. Rocca. Generation of millijoule-level soft-x-ray laser pulses at a 4-hz repetition rate in a highly saturated tabletop capillary discharge amplifier. *Opt. Lett.*, 24(16):1115–1117, 1999.

[MEP+93] S. Maxon, K. G. Estabrook, M. K. Prasad, A. L. Osterheld, R. A. London, and D. C. Eder. High gain x-ray lasers at the water window. *Phys. Rev. Lett.*, 70(15):2285–, April 1993.

[MHR+85] D. L. Matthews, P. L. Hagelstein, M. D. Rosen, M. J. Eckart, N. M. Ceglio, A. U. Hazi, H. Medecki, B. J. MacGowan, J. E. Trebes, B. L. Whitten, E. M. Campbell, C. W. Hatcher, A. M. Hawryluk, R. L. Kauffman, L. D. Pleasance, G. Rambach, J. H. Scofield, G. Stone, and T. A. Weaver. Demonstration of a soft x-ray amplifier. *Phys. Rev. Lett.*, 54(2):110–, January 1985.

[MMDS+90] B. J. MacGowan, S. Maxon, L. B. Da Silva, D. J. Fields, C. J. Keane, D. L. Matthews, A. L. Osterheld, J. H. Scofield, G. Shimkaveg, and G. F. Stone. Demonstration of x-ray amplifiers near the carbon k edge. *Phys. Rev. Lett.*, 65(4):420–, July 1990.

[MMH+87] B. J. MacGowan, S. Maxon, P. L. Hagelstein, C. J. Keane, R. A. London, D. L. Matthews, M. D. Rosen, J. H. Scofield, and D. A.

Whelan. Demonstration of soft x-ray amplification in nickel-like ions. *Phys. Rev. Lett.*, 59(19):2157–, November 1987.

[NAdM+01] Paul Neumayer, J. Alvarez, Bruno Becker de Mos, Stefan Borneis, K. Brueck, Erhard W. Gaul, C. Haefner, Karol A. Janulewicz, Thomas Kuehl, Dieter Marx, Irene Reinhard, Marco Tomaselli, Peter V. Nickles, Wolfgang Sandner, and Wolfgang Seelig. X-ray laser spectroscopy on lithium-like ions. volume 4505, pages 236–242. SPIE, 2001.

[NJS08] P. V. Nickles, K. A. Janulewicz, and W. Sandner. *Advanced Materials and Technologies, Laser Physics and Applications, Laser Systems Part 2 - X-ray lasers*. Springer-Verlag, 2008.

[NM95] Joseph Nilsen and Juan C. Moreno. Nearly monochromatic lasing at 182 å in neonlike selenium. *Phys. Rev. Lett.*, 74(17):3376–, April 1995.

[NMK+93] Yutaka Nagata, Katsumi Midorikawa, Shoich Kubodera, Minoru Obara, Hideo Tashiro, and Koichi Toyoda. Soft-x-ray amplification of the lyman- alpha transition by optical-field-induced ionization. *Phys. Rev. Lett.*, 71(23):3774–, December 1993.

[NSC+04] P. Neumayer, W. Seelig, K. Cassou, A. Klisnick, D. Ros, D. Ursescu, T. Kuehl, S. Borneis, E. Gaul, W. Geithner, C. Haefner, and P. Wiewior. Transient collisionally excited x-ray laser in nickel-like zirconium pumped with the phelix laser facility. *Applied Physics B: Lasers and Optics*, 78(7):957–959, May 2004.

[NSK+97] P. V. Nickles, V. N. Shlyaptsev, M. Kalachnikov, M. Schnürer, I. Will, and W. Sandner. Short pulse x-ray laser at 32.6 nm based on transient gain in ne-like titanium. *Phys. Rev. Lett.*, 78(14):2748–, April 1997.

[OZS+09] E. Oliva, Ph. Zeitoun, S. Sebban, M. Fajardo, P. Velarde, K. Cassou, and D. Ros. Optimization of soft x-ray amplifier by tailoring plasma hydrodynamics. *Opt. Lett.*, 34(17):2640–2642, 2009.

[PDS94] M. D. Perry, T. Ditmire, and B. C. Stuart. Self-phase modulation in chirped-pulse amplification. *Opt. Lett.*, 19(24):2149–2151, December 1994.

[Per95] Michael Perry. Multilayer dielectric gratings: Increasiing the power of light. *Science & Technology Review*, 1995.

[Per06] G. J. Pert. Optimizing the performance of nickel-like collisionally pumped x-ray lasers. *Phys. Rev. A*, 73(3):033809–, March 2006.

[Per07a] G. J. Pert. Optimizing the performance of nickel-like collisionally pumped x-ray lasers. ii. lasers for the wavelength range 50-100 a;. *Phys. Rev. A*, 75(2):023808–, February 2007.

[Per07b] G. J. Pert. Optimizing the performance of nickel-like collisionally pumped x-ray lasers. iii. exploding foil lasers for the wavelength range below 50a;. *Phys. Rev. A*, 75(6):063814–, June 2007.

[PPJC07] Fabien Ple, Moana Pittman, Gerard Jamelot, and Jean-Paul Chambaret. Design and demonstration of a high-energy booster amplifier for a high-repetition rate petawatt class laser system. *Opt. Lett.*, 32(3):238–240, 2007.

[PPS+99] M. D. Perry, D. Pennington, B. C. Stuart, G. Tietbohl, J. A. Britten, C. Brown, S. Herman, B. Golick, M. Kartz, J. Miller, H. T. Powell, M. Vergino, and V. Yanovsky. Petawatt laser pulses. *Opt. Lett.*, 24(3):160–162, 1999.

[PWB+08] F. Pedaci, Y. Wang, M. Berrill, B. Luther, E. Granados, and J. J. Rocca. Highly coherent injection-seeded 13.2 nm tabletop soft x-ray laser. *Opt. Lett.*, 33(5):491–493, 2008.

[RDM+07] B. Rus, J. Dunn, T. Mocek, A. J. Nelson, M. E. Foord, R. Shepherd, W. Rozmus, H. A. Baldis, M. KozlovÃ¡, J. Polan, P. Homer, and M. Stupka. X-ray laser thomson scattering at 21 nm of laser-heated high-density foil plasmas, 2007.

[RGK+09] D. Ros, O. Guilbaud, S. Kazamias, M. Pittman, J.-C. Lagron, B. Zielbauer, J. Habib, J.-P. Chambaret, G. Mourou, K. Cassou, B. Cros, G. Maynard, Ph. Zeitoun, S. Sebban, J. Gautier, A. Klisnick, S. de Rossi, S. Jacquemot, P. Audebert, B. Rus, D. Zimmer, and T. Kuhl. Perspectives of xuv sources development on laserix facility, ile, and eli. volume 7451, page 74510A. SPIE, 2009.

[RKJ+02] D. Ros, A. Klisnick, D. Joyeux, D. Phalippou, O. Guilbaud, J. Kuba, A. Carillon, G. Jamelot, R. Smith, and M. Edwards. Recent progress on the understanding of the transient ni-like ag x-ray laser at 13.9 nm at luli facilities. In J. J. Rocca, J. Dunn, & S. Suckewer, editor, *X-ray Lasers 2002*, volume 641 of *American Institute of Physics Conference Series*, pages 69–76, November 2002.

[RMMK99] J. J. Rocca, C. H. Moreno, M. C. Marconi, and K. Kanizay. Soft-x-ray laser interferometry of a plasma with a tabletop laser and a lloyd's mirror. *Opt. Lett.*, 24(6):420–422, March 1999.

[RMP+02] B. Rus, T. Mocek, A. R. Präg, M. Kozlová, G. Jamelot, A. Carillon, D. Ros, D. Joyeux, and D. Phalippou. Multimillijoule, highly coherent x-ray laser at 21 nm operating in deep saturation through double-pass amplification. *Phys. Rev. A*, 66(6):063806–, December 2002.

[RWL+05] J. J. Rocca, Y. Wang, M. A. Larotonda, B. M. Luther, M. Berrill, and D. Alessi. Saturated 13.2 nm high-repetition-rate laser in nickellike cadmium. *Opt. Lett.*, 30(19):2581–2583, October 2005.

[RZM+97] B. Rus, P. Zeitoun, T. Mocek, S. Sebban, M. Kálal, A. Demir, G. Jamelot, A. Klisnick, B. Králiková, J. Skála, and G. J. Tallents. Investigation of zn and cu prepulse plasmas relevant to collisional excitation x-ray lasers. *Phys. Rev. A*, 56(5):4229–, November 1997.

[SCF+94] Luiz B. Da Silva, Robert C. Cauble, Gene Frieders, Jeffrey A. Koch, Brian J. MacGowan, Dennis L. Matthews, Stanley Mrowka, David B. Ress, James E. Trebes, and Timothy L. Weiland. Imaging with x-ray lasers. volume 2012, pages 158–164. SPIE, 1994.

[SDH+03a] Raymond F. Smith, James Dunn, James R. Hunter, Joseph Nilsen, Sebastien Hubert, Sylvie Jacquemot, Christian Remond, Remy Marmoret, Marta Fajardo, Philippe Zeitoun, Laurent Vanbostal, Ciaran L.S. Lewis, Marie Francoise Ravet, and Franck Delmotte. Longitudinal coherence measurements of a transient collisional x-ray laser. *Opt. Lett.*, 28(22):2261–2263, November 2003.

[SDH+03b] Raymond F. Smith, James Dunn, James R. Hunter, Joseph Nilsen, Sebastien Hubert, Sylvie Jacquemot, Christian Remond, Remy Marmoret, Marta Fajardo, Philippe Zeitoun, Laurent Vanbostal, Ciaran L.S. Lewis, Marie Francoise Ravet, and Franck Delmotte. Longitudinal coherence measurements of a transient collisional x-ray laser. *Opt. Lett.*, 28(22):2261–2263, 2003.

[SDM+03] V. N. Shlyaptsev, James Dunn, S. Moon, R. Smith, Roisin Keenan, Joseph Nilsen, Kevin B. Fournier, Jaroslav Kuba, A. L. Osterheld, J. J. G. Rocca, Bradley M. Luther, Yong Wang, and Mario C. Marconi. Numerical studies of transient and capillary x-ray lasers and their applications. volume 5197, pages 221–228. SPIE, 2003.

[SHB+01] S. Sebban, R. Haroutunian, Ph. Balcou, G. Grillon, A. Rousse, S. Kazamias, T. Marin, J. P. Rousseau, L. Notebaert, M. Pittman, J. P. Chambaret, A. Antonetti, D. Hulin, D. Ros, A. Klisnick, A. Carillon, P. Jaeglé, G. Jamelot, and J. F. Wyart. Saturated amplification of a collisionally pumped optical-field-ionization soft x-ray laser at 41.8 nm. *Phys. Rev. Lett.*, 86(14):3004–, April 2001.

[SHE+09a] J. Seres, D. Hochhaus, B. Ecker, D. Zimmer, T. Kuehl, and C. Spielmann. High-order harmonic source for x-ray laser seeding driven by two-color laser field. In *CLEO/Europe and EQEC 2009 Conference Digest*, page CG25. Optical Society of America, 2009.

[SHE+09b] Josef Seres, Daniel Hochhaus, Boris Ecker, Daniel Zimmer, Christian Spielmann, and Thomas Kuehl. Two-color driven high-order harmonic source for x-ray laser seeding. In *Conference on Lasers and Electro-Optics/International Quantum Electronics Conference*, page JThH4. Optical Society of America, 2009.

[SM85] Donna Strickland and Gerard Mourou. Compression of amplified chirped optical pulses. *Optics Communications*, 55(6):447–449, October 1985.

[SME+06] I. J. Sola, E. Mevel, L. Elouga, E. Constant, V. Strelkov, L. Poletto, P. Villoresi, E. Benedetti, J.-P. Caumes, S. Stagira, C. Vozzi,

G. Sansone, and M. Nisoli. Controlling attosecond electron dynamics by phase-stabilized polarization gating. *Nat Phys*, 2(5):319–322, May 2006.

[SMR+02] S. Sebban, T. Mocek, D. Ros, L. Upcraft, Ph. Balcou, R. Haroutunian, G. Grillon, B. Rus, A. Klisnick, A. Carillon, G. Jamelot, C. Valentin, A. Rousse, J. P. Rousseau, L. Notebaert, M. Pittman, and D. Hulin. Demonstration of a ni-like kr optical-field-ionization collisional soft x-ray laser at 32.8 nm. *Phys. Rev. Lett.*, 89(25):253901–, November 2002.

[SMYH87] M. H. Sher, J. J. Macklin, J. F. Young, and S. E. Harris. Saturation of the xe iii 109-nm laser using traveling-wave laser-produced-plasma excitation. *Opt. Lett.*, 12(11):891–893, 1987.

[SNS+94] V. N. Shlyaptsev, P. V. Nickles, T. Schlegel, M. P. Kalashnikov, and A. L. Osterheld. Tabletop x-ray laser pumped with subnanosecond and picosecond pulses. In S. Suckewer, editor, *Society of Photo-Optical Instrumentation Engineers (SPIE) Conference Series*, volume 2012 of *Presented at the Society of Photo-Optical Instrumentation Engineers (SPIE) Conference*, pages 111–118, February 1994.

[SSH+10] J. Seres, E. Seres, D. Hochhaus, B. Ecker, D. Zimmer, V. Bagnoud, T. Kuehl, and C. Spielmann. Laser-driven amplification of soft x-rays by parametric stimulated emission in neutral gases. *Nat Phys*, advance online publication:–, April 2010.

[SSM+85] S. Suckewer, C. H. Skinner, H. Milchberg, C. Keane, and D. Voorhees. Amplification of stimulated soft x-ray emission in a confined plasma column. *Phys. Rev. Lett.*, 55(17):1753–, October 1985.

[SSV+05] J. Seres, E. Seres, A. J. Verhoef, G. Tempea, C. Streli, P. Wobrauschek, V. Yakovlev, A. Scrinzi, C. Spielmann, and F. Krausz. Laser technology: Source of coherent kiloelectronvolt x-rays. *Nature*, 433(7026):596–596, February 2005.

[STZ+99] R. Smith, G. J. Tallents, J. Zhang, G. Eker, S. McCabe, G. J. Pert,

and E. Wolfrum. Saturation behavior of two x-ray lasing transitions in ni-like dy. *Phys. Rev. A*, 59(1):R47–, January 1999.

[TF00] Riccardo Tommasini and Ernst E. Fill. Generalized linford formula. *J. Opt. Soc. Am. B*, 17(10):1665–1670, October 2000.

[TJPN05] J. Tümmler, K. A. Janulewicz, G. Priebe, and P. V. Nickles. 10-hz grazing-incidence pumped ni-like mo x-ray laser. *Phys. Rev. E*, 72(3):037401–, September 2005.

[TJS+09] J. Tümmler, R. Jung, H. Stiel, P. V. Nickles, and W. Sandner. High-repetition-rate chirped-pulse-amplification thin-disk laser system with joule-level pulse energy. *Opt. Lett.*, 34(9):1378–1380, 2009.

[TNF01] Riccardo Tommasini, Joseph Nilsen, and Ernst E. Fill. Investigations on 10-hz sub-joule fs-laser pumped neon- and nickel-like x-ray lasers. volume 4505, pages 85–92. SPIE, 2001.

[Tre69] E. B. Treacy. Optical pulse compression with diffraction gratings. *IEEE J. Quantum Electron.*, 5:454, 1969.

[TSJ+09] J. Tümmler, H. Stiel, R. Jung, K. A. Janulewicz, P. V. Nickles, and W. Sandner. Towards an 100 hz x-ray laser station, 2009.

[UZK+07] D. Ursescu, D. Zimmer, T. Kuehl, B. Zielbauer, and G.J. Pert. Gain generation in the critical density region of a tce xrl, 2007.

[VBB+06] G. Vaschenko, C. Brewer, F. Brizuela, Y. Wang, M. A. Larotonda, B. M. Luther, M. C. Marconi, J. J. Rocca, C. S. Menoni, E. H. Anderson, W. Chao, B. D. Harteneck, J. A. Liddle, Y. Liu, and D. T. Attwood. Sub-38 nm resolution tabletop microscopy with 13 nm wavelength laser light. *Opt. Lett.*, 31(9):1214–1216, 2006.

[VBR07] Denis Villate, Nathalie Blanchot, and Claude Rouyer. Beam breakup integral measurement on high-power laser chains. *Opt. Lett.*, 32(5):524–526, 2007.

[VEM+06] G. Vaschenko, A. Garcia Etxarri, C. S. Menoni, J. J. Rocca, O. Hemberg, S. Bloom, W. Chao, E. H. Anderson, D. T. Attwood, Y. Lu, and

B. Parkinson. Nanometer-scale ablation with a table-top soft x-ray laser. *Opt. Lett.*, 31(24):3615–3617, 2006.

[WGL+06] Y. Wang, E. Granados, M. A. Larotonda, M. Berrill, B. M. Luther, D. Patel, C. S. Menoni, and J. J. Rocca. High-brightness injection-seeded soft-x-ray-laser amplifier using a solid target. *Phys. Rev. Lett.*, 97(12):123901–, September 2006.

[WGP+08] Y. Wang, E. Granados, F. Pedaci, D. Alessi, B. Luther, M. Berrill, and J. J. Rocca. Phase-coherent, injection-seeded, table-top soft-x-ray lasers at 18.9 nm and 13.9 nm. *Nat Photon*, 2(2):94–98, February 2008.

[WLL+05] Y. Wang, M. A. Larotonda, B. M. Luther, D. Alessi, M. Berrill, V. N. Shlyaptsev, and J. J. Rocca. Demonstration of high-repetition-rate tabletop soft-x-ray lasers with saturated output at wavelengths down to 13.9 nm and gain down to 10.9 nm. *Phys. Rev. A*, 72(5):053807–, November 2005.

[WLW+06] A. Weith, M. A. Larotonda, Y. Wang, B. M. Luther, D. Alessi, M. C. Marconi, J. J. Rocca, and J. Dunn. Continuous high-repetition-rate operation of collisional soft-x-ray lasers with solid targets. *Opt. Lett.*, 31(13):1994–1996, 2006.

[ZAJ+98] Ph. Zeitoun, F. Albert, P. Jaeglé, D. Joyeux, M. Boussoukaya, A. Carillon, S. Hubert, G. Jamelot, A. Klisnick, D. Phalippou, J. C Lagron, D. Ros, S. Sebban, and A. Zeitoun-Fakiris. Investigation of strong electric-field induced surface phenomena by soft x-uv laser interferometry. *Nuclear Instruments and Methods in Physics Research Section A: Accelerators, Spectrometers, Detectors and Associated Equipment*, 416(1):189–191, October 1998.

[ZBE+09a] D. Zimmer, V. Bagnoud, B. Ecker, D. Hochhaus, B. Aurand, B. Zielbauer, D. Ros, and T. Kuehl. Low pumping energy threshold for a ni-like sm x-ray laser pumped in the double-pulse non-normal incidence pumping geometry. In *Proceedings of the Ultrafast Optics Conference*, 2009.

[ZBE+09b] Daniel Zimmer, Vincent Bagnoud, Boris Ecker, Udo Eisenbarth, Jamil Habib, Daniel Hochhaus, Dasa Javorkova, Sophie Kazamias, Thomas Kuehl, David Ros, Daniel Ursescu, and Bernhard Zielbauer. An improved double-pulse non-normal incidence pumping geometry for transient collisionally excited soft x-ray lasers, 2009.

[ZFS+04] Ph. Zeitoun, G. Faivre, S. Sebban, T. Mocek, A. Hallou, M. Fajardo, D. Aubert, Ph. Balcou, F. Burgy, D. Douillet, S. Kazamias, G. de Lacheze-Murel, T. Lefrou, S. le Pape, P. Mercere, H. Merdji, A. S. Morlens, J. P. Rousseau, and C. Valentin. A high-intensity highly coherent soft x-ray femtosecond laser seeded by a high harmonic beam. *Nature*, 431(7007):426–429, September 2004.

[Zie07] B. Zielbauer. *Characterization and Optimization of an x-ray laser for the spectroscopy of Li-like heavy ions.* PhD thesis, Johannes Gutenberg-University Mainz, 2007.

[ZML+97] J. Zhang, A. G. MacPhee, J. Lin, E. Wolfrum, R. Smith, C. Danson, M. H. Key, C. L. S. Lewis, D. Neely, J. Nilsen, G. J. Pert, G. J. Tallents, and J. S. Wark. A saturated x-ray laser beam at 7 nanometers. *Science*, 276(5315):1097–1100, 1997.

[ZRG+10] D. Zimmer, D. Ros, O. Guilbaud, J. Habib, S. Kazamias, B. Zielbauer, V. Bagnoud, B. Ecker, D. C. Hochhaus, B. Aurand, P. Neumayer, and T. Kuehl. Short-wavelength soft-x-ray laser pumped in double-pulse single-beam non-normal incidence. *Phys. Rev. A*, 82(1):013803–, July 2010.

[ZZB+08] Daniel Zimmer, Bernhard Zielbauer, Vincent Bagnoud, Udo Eisenbarth, Dasa Javorkova, and Thomas Kuehl. An improved double-pulse non-normal incidence pumping geometry for transient collisionally excited soft x-ray lasers. *Opt. Express*, 16(14):10398–10404, 2008.

[ZZG+09] Daniel Zimmer, Bernhard Zielbauer, Olivier Guilbaud, Jamil Habib, Sophie Kazamias, Moana Pittman, David Ros, Vincent Bagnoud, Boris Ecker, Daniel Hochhaus, and Thomas Kuehl. Characterization

of a 10hz double-pulse non-normal incidence pumped transient collisional ni-like molybdenum soft x-ray laser for applications. volume 7451, page 745108. SPIE, 2009.

[ZZH+10] B. Zielbauer, D. Zimmer, J. Habib, O. Guilbaud, S. Kazamias, M. Pittman, and D. Ros. Stable and fully controlled long-time operation of a soft x-ray laser for user application experiments. *Applied Physics B: Lasers and Optics*, pages –, 2010.

[ZZP+10] Daniel Zimmer, Bernhard Zielbauer, Moana Pittman, Olivier Guilbaud, Jamil Habib, Sophie Kazamias, David Ros, Vincent Bagnoud, and Thomas Kuehl. Optimization of a tabletop high-repetition-rate soft x-ray laser pumped in double-pulse single-beam grazing incidence. *Opt. Lett.*, 35(4):450–452, 2010.